Design, Modeling, Characterization and Control of Novel Rotary Pumps

By

MENGTANG LI

Dissertation

Submitted to the Faculty of the

Graduate School of Vanderbilt University

in partial fulfillment of the requirements

for the degree of

DOCTOR OF PHILOSOPHY

in

Mechanical Engineering

August 7th, 2020

Nashville, Tennessee

Approved:

Eric Barth, Ph.D.

Michael Goldfarb, Ph.D.

Nilanjan Sarkar, Ph.D.

Kim Stelson, Sc.D.

Andrea Vacca, Ph.D.

To my wife Jia, for her unconditional love and support.

TABLE OF CONTENTS

LIST OF TABLES

LIST OF FIGURES

Chapter 1

Overview

1.1 Introduction

This dissertation presents mathematical modeling, model informed design, experimental verification and validation of prototypes, and control of three hydraulic pumping systems adopting rotary fashion for distinguishable different applications. The first work (AF pump) is a novel hydraulic pump/motor inspired by the hydraulic alternating flow concept to power industrial actuator units compactly on a common shaft and efficiently across a wide range of operating conditions. The second work (MCS pump) presents two novel mechanical circulatory support pump systems, a spherical gerotor architecture and a non-vacuum sliding vane mechanism, to power human body with less shear stress mediated blood damage thus reducing related complications such as platelet activation and hemolysis. And the third work (mHPU) presents a high bandwidth miniature hydraulic power unit to power soft robots within a closed compact system, free from traditionally utilized compressed pneumatic tank.

For AF pump, a dynamic model, describing the cylinder pressure, flows between pairs of cylinders, and net inlet and outlet flows as a function of the pump phase-shift angle was established. The model also captures check valve dynamics, effective bulk modulus, leakage flow, and piston dynamics, which allow energy efficiency calculation and analysis. A prototype was constructed from two inline triplex pumps and experiment tests were conducted and used to validate the model. After model validation, simulation results were utilized to optimize the design for future development of AF pump. For MCS, a bond graph model describing the interaction between cardiovascular system and MCS devices was established first to specify pump performance requirement and to allow study and design of control strategies. Bond graph model guided geometry governing equations were

derived and used for designing a spherical MCS pump and a sliding vane MCS pump. Pump characterization experiments were performed and used to control the prototype to show its ability to generate pulsatile flow. For mHPU, analytical models for pump geometry and flow rate were described firstly. Model guided design was utilized and a workable prototype was manufactured. Pump performance characterization and band width experiments were performed and assessed. Finally, this mHPU prototype was used to control the position of a fluidic muscle manipulator, illustrating its feasibility and competence.

Pronounced impacts of the above mentioned three researches are noted. The AF pump 1) offers a more energy efficient way to directly power every actuator, eliminating metering losses; 2) achieves high efficiency across a wide range of operating conditions and displacements; and 3) allows multiple units to be easily common-shaft mounted for a compact multi-actuator displacement control system from a single prime mover. The spherical gerotor MCS pump 1) presents a novel rotary positive displacement pumping architecture; 2) is capable for both circulation sides (systemic and pulmonary) with only 1 DoF; 3) theoretically reduces shear stress mediated blood damage by its low operating speed. The vane MCS pump 1) shows itself as a novel alternative architecture capable of generating blood flow within clinic range; 2) reduces shear stresses imparted to blood by dramatic reduced rotary speed, particularly in comparison to present VADs (5000 rpm+); and 3) demonstrates the ability of generating pulsatile flow to address related issue of current MCS devices. And the mHPU 1) is scalable for various applications; 2) is compact enough to be integrated into many soft robot structure within a closed loop; 3) has high bandwidth to allow fast response; and 4) demonstrates its suitability and feasibility for soft robotic actuation.

In light of various challenging requirements from different systems and inherent advantages nature of rotary hydraulic pumps, the main contribution of this dissertation involves 1) detailed model guided design method to design and optimize an AF pump, a spherical gerotor MCS pump, a sliding vane MCS pump and a miniature soft robot power supply

pump; 2) building the first variable displacement hydraulic pump utilizing the alternating flow concept; 3) building the first non-vacuum sliding vane pump as an MCS device; and 4) provides the research community with a new method of "servor" motor for soft actuators.

1.2 Background and Significance

1.2.1 Efficiency Improvement in Hydraulic System

Hydraulic fluid power is an excellent type of actuation source. Compared with other primary sources of actuation in industry (electric and pneumatic motors and pistons), the power density of hydraulics is typically more than one order of magnitude better [8] (Tab.1.1) due to the fact that electric motors consist of high density materials such as rare earth magnetic, iron and copper while primary motive force for hydraulic system is incompressible (or relatively incompressible) low density fluids such as oil or water [9-11]. In contrast to hydraulics, pneumatics suffers from low efficiency (15% or lower [8]), low power density and noise. Additionally, the inevitable large compressed air tank would cause problems such as bulky size. Conclusively, the inherently high power density of hydraulic pump can allow for compactly designed devices to help deliver power or fluid to any target systems efficiently.

Table 1.1: Actuation Source Comparison

Actuation Source	Electromagnetic	Pneumatic	Hydraulic
$\frac{Actuator\ Displacement}{Overall\ Actuator\ Length}[\%]$	50	50	70
$\frac{Maximum\ Actuator\ Force}{Actuator\ Cross\ Section}[MPa]$	0.035	0.69	20.8
$\frac{Peak\ Power}{Actuator\ Weight}[W/kg]$	200	200	2000
$Load\ Holding\ Capability[MPa]$	0.1	0.1	1380

Though hydraulic power system is power dense, economically superior, and safe for environment and personnel, low system efficiency (averagely, 50% for industrial and 21% for mobile) is urgently needed to be improved. As a result, the inefficiencies lead to en-

ergy consumption between 2.0 and 2.9 Quadrillion Btus and CO2 release between 310 and 380 million metric tons annually. A typical hydraulic system, as illustrated in Fig.1.1 [8], consists various sources of inefficiency from different primary components. The parasitic loss associated with the engine during power transmitting procedure exists in every system and can be improved as technology advances, thus out of discussion here. Pump efficiency could approach 90% or higher under ideal operating condition. Although much work has been done on improving the maximum efficiency of hydraulic pumps [12-15], such pumps characteristically have low efficiency at low volumetric displacement since the largest energy losses do not scale with output power [16]. Therefore, the pump efficiency drops when it is dealing with time varying load or working under not ideal conditions. Traditional hydraulic circuits use metering valves for precise independent control of individual actuators, using a variable orifice to throttle the flow off unnecessary pressure and energy [17,18]. Valve associated energy losses are also induced by control valves to regulate flows. Valve usage is largely the reason that the overall hydraulic system efficiency is unsatisfactory, as seen in Fig.1.2 [8]. Line loss is another source of inefficiency, typically due to pressure drop associated with line, hose, connectors and couplings.

A clear and urgent need for a more efficient pressure/flow control method for hydraulic system is required, economically and environmentally. Instead of throttling the fluid and transforming the unnecessary power into heat by metering valves, load sensing (LS) circuits [19] are widely used now in industry to control the pressure source to match with the highest pressure load to minimize the throttling loss. An LS system does improve the system efficiency but when the required pressure levels from different loads are not close each other LS still sufferers from throttling loss and poor efficiency [20].

Another method to control hydraulic flow is to vary the flowrate of a fixed displacement pump through the speed control of an electric drive motor, known as electro-hydraulic actuator (EHA). While straightforward and more efficient, the higher cost, lower power density of electronics and reduced motor life restrict the usage of EHA to many industrial

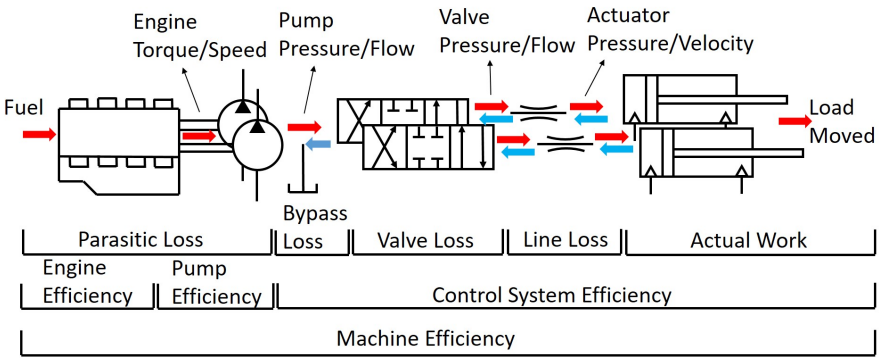

Figure 1.1: Energy losses in a hydraulic system.

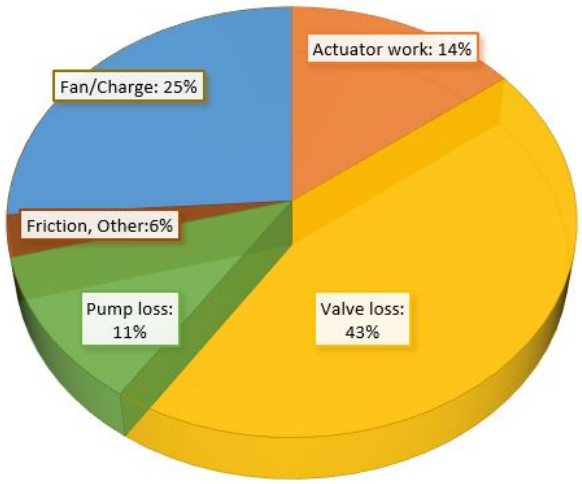

Figure 1.2: Energy losses in mobile load sensing hydraulic application.

applications [21].

The flow could also be controlled with high speed switching of digital valves, termed digital displacement. The most common approach to digital displacement is flow diverting, where the actively controlled tank valve is held open for a portion of the upstroke of the piston, returning the fluid to tank. At a specified displacement fraction of the piston stroke, the tank valve is rapidly closed and the pressure valve is opened, sending flow to the load. While this approach eliminates the leakage and friction of the port plates of an axial piston or bent axis pump, it has several drawbacks. The valve transitions occur at high piston velocity, resulting in throttling energy loss across the partially open tank and pressure valves for a fraction of the piston stroke and generating water hammer creating noise and large

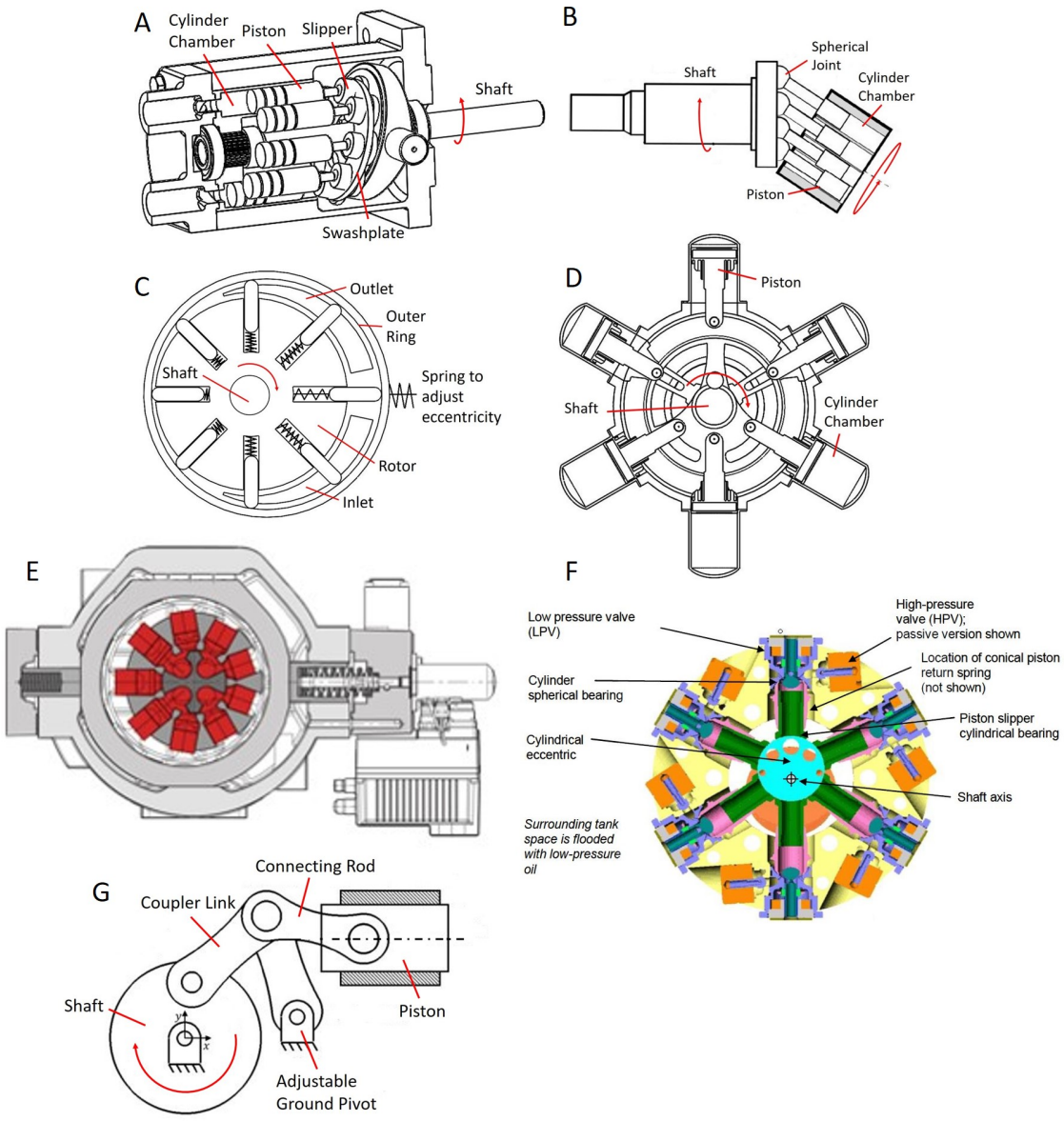

Figure 1.3: Family of variable positive displacement pumps. (A) axial piston pump (swash-plate pump), (B) bent axis pump, (C) vane pump, (D) radial piston pump, (E) Moog RKP pump, (F) Artemis Digital Displacement®pump, (G) variable linkage pump

flow pulsations [22,23]. Viscous flow losses are incurred by pumping the unused flow back to tank, and there is a lack of digital valves with reasonable energy consumption that can switch fast enough for high-speed pumps.

A more efficient alternative is to power each actuator with an individual variable displacement pump and control the actuator with the pump displacement, term displacement

control [24]. An excavator employing displacement control with currently available variable pump/motors has experimentally demonstrated 39% energy savings over throttling valve control in a load sensing circuit [25]. The modularity of displacement control brings another benefit which makes the whole system more reliable than a single pump circuit with metering valves. If one pump fails, the other axes are decoupled and still fully functional. Critical to displacement control is the performance and efficiency of the variable displacement pump across a wide range of displacement and pressures. For multi-actuator circuits, where multiple pumps are driven, ideally on a common shaft, the package size and weight of a single pump are also important. The family of variable positive displacement pumps includes: axial piston pump (swash plate pump), bent axis pump, vane pump, along with some new architectures (Fig.1.3).

Axial piston pump (Fig.1.3A) realizes variable displacement by changing the angle of a non-rotating swash plate [26], which determines the maximum displacement of each piston and adjusts the pump output. A valve plate is needed to guide flow from low pressure port into piston chambers and out to high pressure port. Friction force between cylinder block and the valve plate is relatively constant regardless of the pump displacement, contributing to the majority of energy dissipation [27]. Additional leakage path exists from cylinder chamber to the swash plate to create hydrostatic bearings at the slippers [28]. Furthermore, though compact and robust [12], it is axially long, making it challenging to common-shaft mount multiple pumps.

Bent axis pump [29] (Fig.1.3B) is a variation of axial piston machine. Similar to axial piston pump, bent axis pump varies its displacement by changing the angle between the cylinder block and the shaft. And inevitably, it also suffers from the port plate friction and additional leakage pathway issues. Though high efficient [30], this pump is typically more expensive, more complex, less reliable and do not offer though shaft configuration [12].

Vane pump [31] (Fig.1.3C) sweeps fluid with vanes mounted on a rotor that rotates inside a cavity chamber. Vanes slide into and out of the rotor and seal against the wall

of outer ring, creating chambers that trap fluid and moving fluid from low pressure side to high side. Vane pump varies its displacement by adjusting the eccentricity between the rotor and the outer ring. Complex cavity curve and sealing mechanism, plus high side load on pump shaft, determines low pressure application of vane pump.

Radial piston pump (Fig.1.3D) arranges piston-cylinder pairs in a radial configuration, making it axially short and allowing a through shaft. Usage of check valves instead of valve plate circumvents the energy loss associated with high friction. However, currently, only few variable radial piston configurations are available beyond Moog®RKP [32] (Fig.1.3E), which also suffers from high shaft side load issue. The Artemis Digital Displacement®pump [33] (Fig.1.3F) offers very high efficiencies and packages well due to its radial piston arrangement. This pump however relies on the precise timing of inlet and outlet valves for fluid management [22].

Variable displacement linkage pump [34] (Fig.1.3G) advantages the mechanism of six-bar linkage and uses a changing ground pivot to adjust piston swept volume inside a cylinder chamber while maintaining a constant dead/unswept volume. This pump offers very high efficiency across a wide operating range since its energy losses scale down as the displacement is low [16]. The Achilles' heel of this variable linkage pump is bulky size in the inline configuration and complex in the radial configuration [35].

1.2.2 Mechanical Circulatory Support Device

Heart failure (HF) is the final common pathway of all forms of heart disease with prevalence of 1.7 per 100 persons globally [36]. Presently, more than 6,000,000 patients are afflicted with HF, with this number projected to double over the next two decades [37,38]. HF is the leading cause of hospital admission and number one DRG of Medicare- the largest burden on the health care budget [39,40]. While pharmacologic and electrical therapies have reduced morbidity and mortality for milder classes of HF, severe and end-stage HF (NYHA Class IV/AHA Stage D) requires augmentation or replacement of pump function

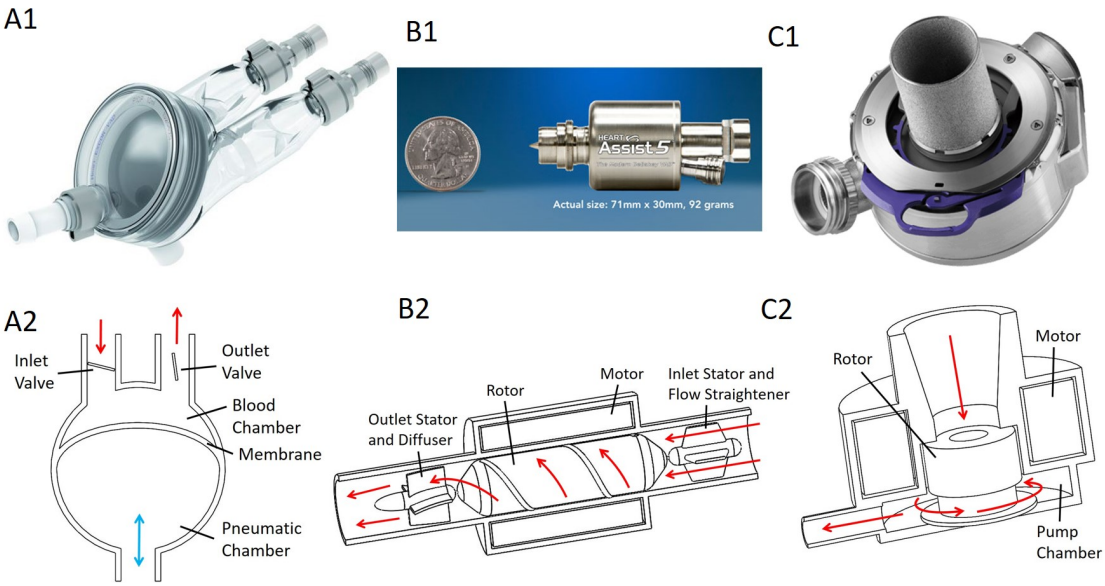

Figure 1.4: A selection of VADs. (A1) Berlin Heart"EXCOR"®[1](represents the first generation VAD), (A2) Working principle, (B1) HeartAssist 5®[2](represents the second generation VAD), (B2) Working principle, (C1) HeartMate 3®[3](represents the third generation VAD), (C2) Working principle.

[41,42]. Notably more than 50% of HF patients progressively develop biventricular (BiV) HF, which is particularly devastating, and is often worsened by treatment of left side only, via unmasking of right heart failure [43-47]. Human allograft heart transplantation, the definitive therapy for these patients, is hampered by a severe lack of donor hearts [48], with more than 200,000 patients in need in the U.S., with only 2500 transplants performed annually on average [49].

In response to this, the field of mechanical circulatory support device (MCS) has emerged to provide for immediate hemodynamic restoration in patients with progressive, often rapid, cardiovascular collapse; as well as to address the limited availability of donor hearts for transplantation for patients with advanced and end-stage heart failure [41]. To date a range of ventricular assist devices (VAD) and total artificial hearts (TAH) have emerged, with several achieving FDA approval [50-53]. The bulk of MCS development has focused on single ventricle augmentation systems, i.e. VADs. Photographs of several noteworthy VADs are presented in Fig.1.4.

Analogy to a real human heart to produce pulsatile physiologic flow to the circulatory system, the first generation of VADs adopts fixed volume displacement fashion that incorporates sacs, diaphragms or pusher plates actuated pneumatically, electrically or mechanically (Fig. 1.4A1). Some good examples of this type are Berlin Heart EXCOR [54-56], Thoratec HeartMate 1 [57-59], Thoratec IVAD/PVAD [60] and Abiomed AB5000 [61,62]. Working principles (Fig.1.4A2) of different designs are generally the same. Blood is pulled into a flexible chamber from left or right ventricle and pushed out into ascending aorta or pulmonary artery while uni-directional blood flow is guaranteed by prosthetic valves. Although they could generate pulsatile physiologic blood flow, these pumps inherently are bulky, which make them difficult to fit into many patients [63], and have large blood contacting surfaces which require frequent coagulation of warfarin, aspirin and dipyridamole to maintain high international standard ratio (INR) [54]. Also, mechanical failure caused by flexible membranes or diaphragms limits device durability [63].

To circumvent disadvantages mentioned above, hydrodynamic blood pumps generating continuous flow instead of pulsatile flow, despite that concerns exist about the effects of non-pulsatile flow, are favored more and more by researchers and manufactures thanks to its distinct advantages of compactness and durability. These second generation VADs (Fig.1.4B1) normally consist a fast spinning impeller (5000-10000 rpm), flow straightener and diffuser. Distinguished VADs are Thoratec HeartMate 2 [64-66], Reliant Heart HeartAssist 5 [67,68], Jarvik Heart Jarvik 2000 FlowMaker [69,70] and Berlin Heart INCOR [71,72]. Due to its working principle (Fig.1.4B2), the flow rate depends on the pressure difference across the VAD, which requires precise sensors and cardiovascular model and control algorithm to generate desired blood flow. The dramatically high velocity at the impeller edge contributes high shear stress to blood, inducing hemolysis and platelet activation. Also, thrombus may format in regions of recirculation or stagnation such as the stationary flow straightener [73]. Lastly, the lifespan of these axial flow VADs is limited below five years due to the mechanical contact bearing and impeller's fast rotary speed

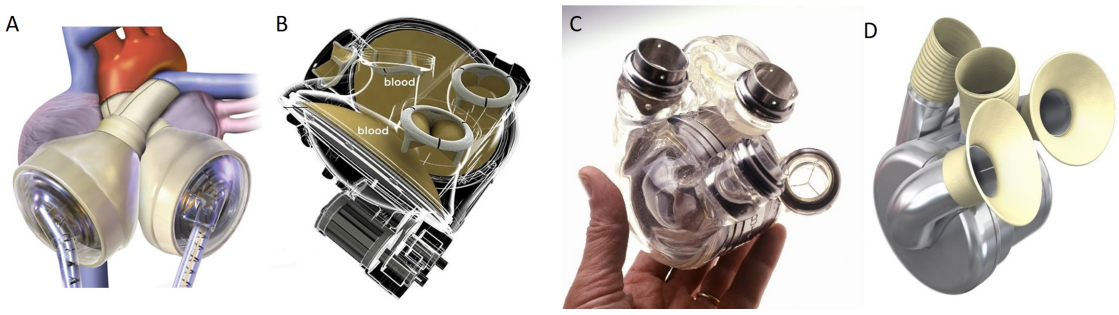

Figure 1.5: A selection of TAHs. (A) SynCardia®TAH [4], (B) Carmat®TAH [5], (C) Abiocor®TAH [6], (D) BiVACOR®TAH [7]

[74].

The third generation of VADs (Fig.1.4C1), utilizing centrifugal pumping architecture, has showed superiority to its ancestor. As shown in Fig.1.4C2, blood enters into the rotor and is driven outward centrifugally to aorta or pulmonary artery without need of flow straightener at inlet or diffuser at outlet, thus lower probability to induce hemolysis and platelet activation. Compared to axial flow VAD, the rotary speed of these centrifugal VADs could be lower due to higher hydraulic efficiency of centrifugal pumping mechanism. Furthermore, the impeller wear issue could be completely eliminated using magnetic levitation, ensuring longer lifespan than axial flow VADs. Some noteworthy VADs are Thoratec HeartMate 3 [75,76] and HeartWare HVAD [77-79].

Despite VADs have successfully illustrated effectiveness to restore hemodynamics, patients with a particular unmet need are those with dual or biventricular HF - being more than 50% of the end-stage HF population, poorly treated with LVADs alone [43-47]. Surgical groups have attempted makeshift placement of two durable CFVADs into these patients, which has only resulted in amplified adverse events from two imposed systems [80,81]. For these patients the only effective MCS solution has been the TAH treatment. Some representative TAHs are listed in Fig.1.5.

SynCardia TAH (Fig.1.5A) [53], as the first FDA approved TAH as a bridge to transplantation in 2004 and for voluntary implantation as destination therapy [82], consists of

two ventricles with four tilting disc valves to direct flows. Each ventricle is separated by four layers of flexible and durable membranes into two compartments for blood and air respectively. Pulses of air and vacuum is generated by external terminal/driver and travels through percutaneous drivelines to inflate and deflate the diaphragms within each ventricle, creating pulsatile blood flow. Though effective, SynCardia TAH is bulky, noisy, potential of infections due to percutaneous air hoses and it demonstrated membrane failure [52,83].

Carmat TAH (Fig.1.5B) [84] shares a similar working principle as SynCardia TAH. But instead of driving the membrane with pneumatics, Carmat has two electro-hydraulic pumps controlled to move viscous fluid back and forth to pull and push against membranes to generate pulsatile flow. Although free from transcutaneous air hoses, Carmat TAH is too bulky and heavy (1kg) to fit into most patients [85].

Abiocor TAH (Fig.1.5C) [86], similar to the previous two TAHs, consists of two pumping compartments with flexible membranes and four trileaflet valves. Uniquely, a centrifugal pump (rotates at 4000-8000 rpm) is placed in the middle of the TAH, between those two membranes. Hydraulic oil is shuttled back and forth to alternately compress the flexible diagraphms, resulting in pulsatile flow generation. A rotary port cylinder is specially designed. It rotates continuously around the hydraulic pump and changes its direction, eliminating the need to change the rotary direction of the hydraulic pump.

BiCACOR TAH (Fig.1.5D) [87], unlike the previous three TAHs, features a single rotary component with systemic and pulmonary impellers on opposing faces. While rotating at the same speed, different impeller size and geometry allows different flow characteristics for the systemic and pulmonary circulation sides. The impeller is magnetic levitated, without the need of any mechanical bearings. Also, as it takes advantages of centrifugal pump, no valve is needed, thus further reducing hemolysis and platelet activation potential. A similar design is Cleveland SmartHeart TAH [88,89].

1.2.3 Actuation Methods for Soft Robot

Soft robotics utilizes the compliance and adaptability of soft materials to interact with human and environment more safely than conventional rigid-body robots made with high stiffness materials [90]. Compared to rigid robots, soft robots have shown superiority in performing tasks in unstructured and un-defined environments. The elastic and soft material properties, on one hand, grant a soft robot the ability to bend, stretch and contract, on the other hand require special actuation methods other than rigid electric motors which are the common actuation method for conventional robots. Also, it is critical that soft robots, especially in mobile applications, have a power supply and actuation system with high power density, high control bandwidth, and high efficiency. The goal herein is to fill the gap of having no viable compact, convenient, high bandwidth and high power density direct power unit for soft robotics.

Some common actuation methods studied in soft robotics include cable (tendon) drive, fluidic actuation (pneumatics and hydraulics) and shape memory alloy (SMA) [90].

Cable drives allow for the transfer of very high tensile strength and forces to a manipulator from a distant power source along its longitudinal axis while also permitting bending in other directions without noticeable strength loss. With cable's unique features, the system moment of inertia is low and movements of joints and manipulators are not affected. Although cables can be guided through complex routes and mounted to the system easily and tightly (e.g. a spine [91]), adequate space to include a power source such as a spooler motor might make the whole soft robotic system bulky. Nonetheless, due to is simplicity, the cable driven method is a very common actuation method for soft continuum robots [92-96], soft robotic manipulators (for instance an octopus inspired arm uses embedded cables for reaching [97,98]) and soft robot locomotions (for example a cable driven fish robot [99]).

Pneumatic actuation datas back to the 1950s when McKibben invented an unbraided chord tube, which replicated the functionality of contracting muscle when pressurized. In-

spired by the McKibben actuator, more-recently developed unbraided channeled silicon molds, often called PneuFlex Actuator [100], Pneumatic Neworks (Pneu-Nets) [101], or PneuFlex Actuator [102], have been shown not only to have the ability to contract and expand but also to bend. Because pneumatic networks are lightweight and can operate using ambient air, this actuation method has been adopted by many bio-inspired soft robots such as a resilient quadrupedal robot [103]. A fish-like robot [104], a snake-like robot [105], and a manta ray-like robot [106]. However, using pressurized air inevitably limits the mobility of any pneumatic powered soft robots since the source is normally connected to a building or at least a big air tank. Even though some study showed on-board chemical decomposition of gas generation in a closed container could also be used to regulate the pressure [107], this method will not be able to replace the traditional pressure source. Another noticeable disadvantage of pneumatics comes from its poor dynamic behavior because the working fluid, air or other gas, is compressible.

Hydraulic actuation shares many similarities with pneumatic actuation as both approaches regulate internal pressure to deform a structure in a controlled manner and some soft robots can be powered by either method [108]. In contrast to most pneumatic systems, hydraulic systems normally contain a closed loop of working fluid, enabling them to function in untethered environment such as an under-water robotic fish [109] or in mobile application such as a rehab device [110] and an exoskeleton [111-113]. Although hydraulics provides larger forces and faster system dynamics than pneumatics, classic system circuits contain pressure regulators, directional valves, and accumulators, making traditional hydraulics not suitable for small-package designs. Electro-hydraulic actuators (EHAs) offer an alternative approach to directly supply power to actuators by varying the speed of an electric drive motor connected to a fixed displacement hydraulic pump, eliminating the need for conventional control valves [114-116].

Shape memory alloy is a novel, light, simple, and deformable material of interest to soft robot developers thanks to its ability to revert to its original position and orientation

when heated. This unique effect has been utilized by researchers to actuate various soft robots, such as a meshworm robot inspired by the peristaltic of Oligochaetes [117], the GoQBot, a soft body rolling robot inspired by a caterpillar [118], and octopus like robots [119,120]. The most significant drawback to adopting SMAs more broadly in soft robotic systems is material hysteresis, as cooling the material takes more time than heating [121], which makes SMAs not suitable for many bi-directional applications.

1.3 Document Organization

This dissertation consists of 8 chapters and is organized as follows. Chapter 2 presents dynamical modeling, prototype fabrication, and experimental validation of a novel variable displacement hydraulic pump. Chapter 3 develops a bond graph model of mechanical circulatory support device and cardiovascular system interaction. Chapter 4 derives a mathematical synthesis of a spherical total artificial heart. Chapter 5 presents design, modeling, prototype fabrication, and performance characterization of a novel valveless MCS pump based on sliding vane mechanism. Chapter 6 demonstrates design, prototype fabrication, performance characterization, and soft robotic actuator control application of a miniature hydraulic power unit. Chapter 7 summarizes this dissertation, along with contributions. Summaries of the manuscripts included in this dissertation are as follows:

Manuscript 1 (Chapter 2): *Design, Dynamic Modelling and Experiment Validation of A Novel Alternating Flow Variable Displacement Hydraulic Pump*, M. Li, R. Foss, K. A. Stelson, J. D. Van de Ven, E. J. Barth

From: *IEEE/ASME Transactions on Mechatronics*

Abstract: High power density, good controllability and low cost are the most appealing characteristics that make hydraulic systems the best choice for many applications. Current state of the art hydraulic variable displacement pumps show high efficiency at high displacement while they have poor efficiencies at low displacement. This paper proposes a

novel alternating flow (AF) variable displacement hydraulic pump to 1) eliminate metering losses by acting as a high-bandwidth pump for displacement control, 2) achieve high efficiency across a wide range of operating conditions and displacements, and 3) allow multiple units to be easily common-shaft mounted for a compact multi-actuator displacement control system from a single prime-mover. A dynamic model using first principles describes the cylinder pressure, flows between pairs of cylinders, and net inlet and outlet flows as a function of the pump's phase shift angle. The model captures hydraulic check valve dynamics, the effective bulk modulus, leakage flows, and viscous friction. Piston kinematics and dynamics are discussed and energy loss models are presented. A first prototype of the AF pump was constructed from two inline triplex pumps that were modified so that three piston pairs were created. Experiment tests were conducted and used to validate the model. After model validation, simulation results from the model can offer an initial evaluation of this novel pump concept and potential applications and can be used to guide the design for future prototype of the AF hydraulic pump.

Manuscript 2 (Chapter 3): *Bond Graph Modeling of Mechanical Circulatory Support (MCS) Device - Cardiovascular System Interactions*, M. Li, M. J. Slepian, E. J. Barth

From: *ASME Journal of Biomechanical Engineering*

Abstract: Though mechanical circulatory support (MCS) devices, such as ventricular assist devices (VAD) and total artificial hearts (TAH), provide heart failure patients with bridges to heart transplantation or are alternatives to transplantation, device performance and corresponding control strategies are often difficult to evaluate. Difficulties arise due to the complex interaction of multiple domains – i.e. biological, hydraulic, hemodynamics, electromechanical, system dynamics, and controls. In an attempt to organize, integrate and clarify these interactions, a technique often used in hydraulic pump design and robotics, called "bond graph modeling," is applied to describe the performance and functionality of MCS devices and the interaction between the cardiovascular system and the MCS device.

This technical brief demonstrates the advantages of this tool in formulating a model for the systemic circulation interacting with the left side of a TAH, adopting the fundamental structure of either a hydraulic mechanism (i.e. AbioCor/Carmat) or a pneumatic mechanism (i.e. SynCardia), combined with a systemic circulation loop. The model captures the dynamics of the membrane, the hydraulic source or pneumatic source, and the systemic circulation. This multi-disciplinary cross-pollination of an analytical tool from the field of dynamic systems may provide important insight to further aid and improve the design and control of future MCS systems.

Manuscript 3 (Chapter 4): *Spherical Gerotor: Synthesis of a Novel Valveless Pulsatile Flow Spherical Total Artificial Heart*, M. Li, E. J. Barth

From: *Journal of Mechanics Engineering and Automation*

Abstract: Though mechanical circulatory support (MCS) devices, such as ventricular assist device (VAD) and total artificial heart (TAH), indeed provide heart failure patients with an alternative to transplantation, many complications are provided at the same time due to the non-pulsatile blood flow or high blood shear induced by those MCS. A novel spherical total artificial heart (TAH) based on the concept of hydraulic gerotor pump is proposed. This spherical TAH features volumetric pumping mechanism, pulsatile flow generating and low blood shear. It consists of four time-varying chambers partitioned by two orange shape wedges and one complex curve cut disk. The disk rotates as twice fast as the wedges, while all in the same direction. The TAH sucks in and pumps out blood through four ports located at the pump peripheral. This paper presents the fundamental equations which establish the geometric shape of the TAH, develop the range of the size specs, and show the analytical model for the time-varying chamber volume.

Manuscript 4 (Chapter 5): *Design, Modeling, and Experimental Characterization of A Valveless Pulsatile Flow Mechanical Circulatory Support (MCS) Device*, M. Li, Y. Chen,

M. J. Slepian, J. T. Howard, B. S. Thomas, E. J. Barth

From: *ASME Journal of Biomechanical Engineering*, Under Review

Abstract: Mechanical circulatory support (MCS) devices, i.e. ventricular assist devices (VADs) and total artificial hearts (TAHs), while effective and vital in restoring hemodynamics in patients with circulatory compromise in advanced heart failure, remain limited by significant adverse thrombotic, embolic and bleeding events. Many of these complications relate to chronic exposure, via these devices, to non-pulsatile flow and the high shear stress created by current methods of blood propulsion or use of prosthetic valves. Here we proposes a novel valveless pulsatile flow MCS device to: 1) lower the shear stress imparted to blood by dramatically reduced pump operating speed; 2) eliminate utilization of prosthetic valves thus diminishing potential shear stress generations; 3) allow direct flowrate control to generate physically desired blood flowrate include pulsatile flow; and 4) achieve compactness to fit into the majority of patients. The fundamental working principle and governing design equations are introduced first with multiple design and performance objectives presented. A first prototype was fabricated and experimental tests were conducted to validate the model. After model validation, the proposed MCS was controlled to illustrate the ability of pulsatile flow generation. The presented work offers a novel MCS design and paves the way for next steps in device hemocompatibility testing.

Manuscript 5 (Chapter 6): *A "Servopump" for Soft Robotics*, M. Li, B. S. Thomas, J. T. Howard, E. J. Barth

From: *Soft Robotics*, Under Review

Abstract: A hydraulic "servopump" for soft robotics that directly powers soft actuators is proposed and presented here. This is akin to a servomotor for traditional robotics that is suitable for closed-loop feedback control. This miniature hydraulic power unit (mHPU), based on a gerotor architecture and driven by a DC motor, features compactness, convenience, high bandwidth and high power density. It offers a highly controllable actuation

package that current soft robotic systems lack. A design methodology is presented for sizing the mHPU for a given flowrate. A prototype is demonstrated for a target application with a flowrate of ±3 L/min and maximum output pressure of 500kPa (77 psig). Our first-generation prototype was designed and fabricated with a positive-displacement gerotor architecture of 0.5 mL/rev directly driven by a 60W brushless DC motor. The mHPU prototype was characterized in terms of flowrate (as a function of speed and pressure load), efficiency (volumetric, mechanical, electrical and total efficiency), and control bandwidth. Energy efficiency of the proposed mHPU offers a peak efficiency near 45%, offering comparable efficiencies of non-soft servomotor actuated systems. Bandwidth characterization demonstrated the mHPU has a bandwidth of approximately 35 Hz, which is well above the mechanical frequency of many soft robots and results in high control authority. As a demonstration of the control capabilities of the mHPU, the position of a basic fluidic muscle was controlled with a simple PID controller and exhibited a fast and accurate step response (1.6 cm step in 250ms with a steady-state accuracy of 0.2 mm).

1.4 References

[1] Berlin heart inc. https://www.berlinheart.com/.

[2] Reliant heart inc. http://reliantheart.com/.

[3] Thoratec corporation. https://www.heartmate.com/.

[4] Syncardia systems llc. https://www.syncardia.com/.

[5] Carmat. https://www.carmatsa.com/en/.

[6] Abiomed. https://www.abiomed.com/en/.

[7] Bivacor inc. https://bivacor.com/.

[8] Lonnie J Love. Estimating the impact (energy, emissions and economics) of the us fluid power industry. Technical report, Oak Ridge National Laboratory (ORNL), 2012.

[9] Ilene J Busch-Vishniac. Electromechanical sensors and actuators. Springer Science & Business Media, 1998.

[10] AP Dorey and JH Moore. Advances in actuators; Ed. by AP Dorey, JH Moore. Inst. of physics Bristol, 1995.

[11] MV Gandhi and BS Thompson. Electro-rheological fluids. Smart Materials and Structures, Chapman and Hall, London, UK, 1992´a Search´aPubMed ´a, 1992.

[12] Monika Ivantysynova. Innovations in pump design-what are future directions? In Proceedings of the JFPS International Symposium on Fluid Power, volume 2008, pages 59–64. The Japan Fluid Power System Society, 2008.

[13] Chao Zhang, Shaokang Huang, Jun Du, Xingjian Wang, Shaoping Wang, and Haiyan Zhang. A new dynamic seven-stage model for thickness prediction of the film between valve plate and cylinder block in axial piston pumps. Advances in Mechanical Engineering, 8(9):1687814016671446, 2016.

[14] Lizhi Shang and Monika Ivantysynova. A temperature adaptive piston design for swash plate type axial piston machines. International Journal of Fluid Power, 18(1):38–48, 2017.

[15] G Rizzo, GP Massarotti, A Bonanno, R Paoluzzi, M Raimondo, M Blosi, F Veronesi, A Caldarelli, and G Guarini. Axial piston pumps slippers with nanocoated surfaces to reduce friction. International Journal of Fluid Power, 16(1):1–10, 2015.

[16] Shawn R Wilhelm and James D Van de Ven. Synthesis of a variable displacement linkage for a hydraulic transformer. In ASME 2011 International Design Engineering Technical Conferences and Computers and Information in Engineering Conference, pages 309–316. American Society of Mechanical Engineers, 2011.

[17] Mengtang M Li, Ryan Foss, Kim A Stelson, James D Van de Ven, and Eric J Barth. Dynamic model of a novel alternating flow (af) hydraulic pump. In ASME/BATH 2017 Symposium on Fluid Power and Motion Control. American Society of Mechanical Engineers Digital Collection, 2017.

[18] Ryan J Foss, Mengtang Li, Eric J Barth, Kim A Stelson, and James D Van de Ven. Experimental studies of a novel alternating flow (af) hydraulic pump. In ASME/-BATH 2017 Symposium on Fluid Power and Motion Control. American Society of Mechanical Engineers Digital Collection, 2017.

[19] R Book and CE Goering. Load sensing hydraulic system simulation. Applied Engineering in Agriculture, 13(1):17–25, 1997.

[20] Mengtang Li, Ryan Foss, Kim Stelson, James Van de Ven, and Eric John Barth. Design, dynamic modelling and experiment validation of a novel alternating flow variable displacement hydraulic pump. IEEE/ASME Transactions on Mechatronics, 2019.

[21] Christopher Williamson and Monika Ivantysynova. Pump mode prediction for four-quadrant velocity control of valueless hydraulic actuators. In Proceedings of the JFPS International Symposium on Fluid Power, volume 2008, pages 323–328. The Japan Fluid Power System Society, 2008.

[22] Md Ehsan, WHS Rampen, and SH Salter. Modeling of digital-displacement pump-motors and their application as hydraulic drives for nonuniform loads. Journal of dynamic systems, measurement, and control, 122(1):210–215, 2000.

[23] Matti Linjama. Digital fluid power: State of the art. In 12th Scandinavian International Conference on Fluid Power, Tampere, Finland, May, pages 18–20, 2011.

[24] Kim Heybroek. Saving energy in construction machinery using displacement control hydraulics: Concept realization and validation. PhD thesis, Link¨oping University Electronic Press, 2008.

[25] Christopher Williamson. Efficiency study of an excavator hydraulic system based on displacement-controlled actuators. In Proceedings of the Bath/ASME Symposium on Fluid Power and Motion Control (FPMC), 2008, pages 291–307, 2008.

[26] John A Anning. The "michell" crankless engine–why was it not a commercial success?

[27] Rene Chacon. Cylinder block/valve plate interface performance investigation through the introduction of micro-surface shaping. PhD thesis, Purdue University, 2014.

[28] Terry L Henshaw. Reciprocating pumps. 1987.

[29] Hermann Eris Busse and Hans Thoma. Hans Thoma: Leben und Werk. Dt. Buch-Gemeinschaft, 1935.

[30] Jong-Ki Kim and Jae-Youn Jung. Driving mechanism of tapered pistons in bent-axis design axial piston pumps. KSME international journal, 17(2):181–186, 2003.

[31] Mario Theriault. Great Maritime Inventions, 1833-1950. Goose Lane Editions Fredericton, 2001.

[32] Moog. Radial Piston RKP. Moog, rev g. edition, 2015.

[33] Niall James Caldwell. Digital displacement hydrostatic transmission systems. 2007.

[34] Shawn Wilhelm. Modeling, analysis, and experimental investigation of a variable displacement linkage pump. 2015.

[35] Shawn Wilhelm and James Van de Ven. Adjustable linkage pump: efficiency modeling and experimental validation. Journal of Mechanisms and Robotics, 7(3):031013, 2015.

[36] Dariush Mozaffarian, Emelia J Benjamin, Alan S Go, Donna K Arnett, Michael J Blaha, Mary Cushman, Sandeep R Das, Sarah De Ferranti, Jean Pierre Despr´es, Heather J Fullerton, et al. Heart disease and stroke statistics-2016 update a report from the american heart association. Circulation, 133(4):e38–e48, 2016.

[37] Writing group Members, Donald Lloyd-Jones, Robert Adams, Mercedes Carnethon, Giovanni De Simone, T Bruce Ferguson, Katherine Flegal, Earl Ford, Karen Furie, Alan Go, et al. Heart disease and stroke statistics—2009 update: a report from the american heart association statistics committee and stroke statistics subcommittee. Circulation, 119(3):480–486, 2009.

[38] Emelia J Benjamin, Paul Muntner, and M´arcio Sommer Bittencourt. Heart disease and stroke statistics-2019 update: A report from the american heart association. Circulation, 139(10):e56–e528, 2019.

[39] Akshay S Desai and LynneWStevenson. Rehospitalization for heart failure: predict or prevent? Circulation, 126(4):501–506, 2012.

[40] David H Smith, Eric S Johnson, David K Blough, Micah L Thorp, Xiuhai Yang, Amanda F Petrik, and Kathy A Crispell. Predicting costs of care in heart failure patients. BMC health services research, 12(1):434, 2012.

[41] Jennifer L Cook, Monica Colvin, Gary S Francis, Kathleen L Grady, Timothy M Hoffman, Mariell Jessup, Ranjit John, Michael S Kiernan, Judith E Mitchell, Francis D Pagani, et al. Recommendations for the use of mechanical circulatory support: ambulatory and community patient care: a scientific statement from the american heart association. Circulation, 135(25):e1145–e1158, 2017.

[42] Clyde W Yancy, Mariell Jessup, Biykem Bozkurt, Javed Butler, Donald E Casey, Mark H Drazner, Gregg C Fonarow, Stephen A Geraci, Tamara Horwich, James L Januzzi, et al. 2013 accf/aha guideline for the management of heart failure: a report of the american college of cardiology foundation/american heart association task force on practice guidelines. Journal of the American College of Cardiology, 62(16):e147–e239, 2013.

[43] Francisco A Arab´ıa, Ryan S Cantor, Devin A Koehl, Vigneshwar Kasirajan, Igor Gregoric, Jaime D Moriguchi, Fardad Esmailian, Danny Ramzy, Joshua S Chung, Lawrence S Czer, et al. Interagency registry for mechanically assisted circulatory support report on the total artificial heart. The Journal of Heart and Lung Transplantation, 37(11):1304–1312, 2018.

[44] Francisco A Arab´ıa, Carmelo A Milano, Claudius Mahr, Edwin C McGee Jr, Nahush A Mokadam, J Eduardo Rame, Jaime D Moriguchi, Danny Ramzy, David C Naftel, Susan L Myers, et al. Biventricular support with intracorporeal, continuous flow, centrifugal ventricular assist devices. The Annals of thoracic surgery, 105(2):548–555, 2018.

[45] Nicholas C Dang, Veli K Topkara, Michelle Mercando, Joy Kay, Kurt H Kruger, Michael S Aboodi, Mehmet C Oz, and Yoshifumi Naka. Right heart failure after left ventricular assist device implantation in patients with chronic congestive heart failure. The Journal of heart and lung transplantation, 25(1):1–6, 2006.

[46] Brent C Lampert and Jeffrey J Teuteberg. Right ventricular failure after left ventricular assist devices. The Journal of Heart and Lung Transplantation, 34(9):1123–1130, 2015.

[47] Diyar Saeed. Right ventricular failure and biventricular support strategies. Cardiology clinics, 36(4):599–607, 2018.

[48] Kiran K Khush,Wida S Cherikh, Daniel C Chambers, Samuel Goldfarb, Don Hayes, Anna Y Kucheryavaya, Bronwyn J Levvey, Bruno Meiser, Joseph W Rossano, and Josef Stehlik. The international thoracic organ transplant registry of the international society for heart and lung transplantation: thirty-fifth adult heart transplantation report— 2018; focus theme: multiorgan transplantation. The Journal of Heart and Lung Transplantation, 37(10):1155–1168, 2018.

[49] Lars H Lund, Kiran K Khush, Wida S Cherikh, Samuel Goldfarb, Anna Y Kucheryavaya, Bronwyn J Levvey, Bruno Meiser, Joseph W Rossano, Daniel C Chambers, Roger D Yusen, et al. The registry of the international society for heart and lung transplantation: thirty-fourth adult heart transplantation report—2017; focus theme: allograft ischemic time. The Journal of Heart and Lung Transplantation, 36(10):1037–1046, 2017.

[50] Mark S Slaughter, Joseph G Rogers, Carmelo A Milano, Stuart D Russell, John V Conte, David Feldman, Benjamin Sun, Antone J Tatooles, Reynolds M Delgado III, James W Long, et al. Advanced heart failure treated with continuous-flow left ventricular assist device. New England Journal of Medicine, 361(23):2241–2251, 2009.

[51] Martin Strueber, Gerry O'Driscoll, Paul Jansz, Asghar Khaghani, Wayne C Levy, George M Wieselthaler, HeartWare Investigators, et al. Multicenter evaluation of an intrapericardial left ventricular assist system. Journal of the American College of Cardiology, 57(12):1375–1382, 2011.

[52] Jack G Copeland, Richard G Smith, Francisco A Arabia, Paul E Nolan, Gulshan K Sethi, Pei H Tsau, Douglas McClellan, and Marvin J Slepian. Cardiac replacement with a total artificial heart as a bridge to transplantation. New England Journal of Medicine, 351(9):859–867, 2004.

[53] Marvin J Slepian, Yared Alemu, Jo˜ao Silva Soares, Richard G Smith, Shmuel Einav, and Danny Bluestein. The syncardia™ total artificial heart: in vivo, in vitro, and computational modeling studies. Journal of biomechanics, 46(2):266–275, 2013.

[54] Thorsen Drews, Matthias Loebe, Ewald Hennig, Friedrich Kaufmann, Johannes M¨uller, and Roland Hetzer. The 'berlin heart'assist device. Perfusion, 15(4):387–396, 2000.

[55] David LS Morales, Christopher SD Almond, Robert DB Jaquiss, David N Rosenthal, David C Naftel, M Patricia Massicotte, Tilman Humpl, MarkWTurrentine, James S Tweddell, Gordon A Cohen, et al. Bridging children of all sizes to cardiac transplantation: the initial multicenter north american experience with the berlin heart excor ventricular assist device. The Journal of Heart and Lung Transplantation, 30(1):1–8, 2011.

[56] William J Weiss. Pulsatile pediatric ventricular assist devices. Asaio Journal, 51(5):540–545, 2005.

[57] Timothy R Maher, Kenneth C Butler, Victor L Poirier, and David B Gernes. Heartmate left ventricular assist devices: a multigeneration of implanted blood pumps. Artificial organs, 25(5):422–426, 2001.

[58] Patrick M McCarthy. Heartmate implantable left ventricular assist device: bridge to transplantation and future applications. The Annals of thoracic surgery, 59:S46–S51, 1995.

[59] James W Long. Advanced mechanical circulatory support with the heartmate left ventricular assist device in the year 2000. The Annals of thoracic surgery, 71(3):S176–S182, 2001.

[60] S Whittaker and C Glanville. The thoratec® ventricular assist device system. Perfusion, 15(4):363–368, 2000.

[61] Li Zhang, Emmanouil I Kapetanakis, Richard H Cooke, Leslie C Sweet, and Steven W Boyce. Bi-ventricular circulatory support with the abiomed ab5000 system in a patient with idiopathic refractory ventricular fibrillation. The Annals of thoracic surgery, 83(1):298–300, 2007.

[62] Marc E Stone. Current status of mechanical circulatory assistance. In Seminars in cardiothoracic and vascular anesthesia, volume 11, pages 185–204. Sage Publications Sage CA: Los Angeles, CA, 2007.

[63] Eric H Maslen, Gill B Bearnson, Paul E Allaire, Ronald D Flack, Michael Baloh, Edgar Hilton, Myounggyu D Noh, Don B Olson, Pratap S Khanwilkar, and James D Long. Artificial hearts. In Proceedings of the 1997 IEEE international conference on control applications, pages 204–209. IEEE, 1997.

[64] David J Burke, Edward Burke, Farzad Parsaie, Victor Poirier, Kenneth Butler, Douglas Thomas, Lynn Taylor, and Timothy Maher. The heartmate ii: design and development of a fully sealed axial flow left ventricular assist system. Artificial organs, 25(5):380–385, 2001.

[65] OH Frazier and Leon P Jacob. Small pumps for ventricular assistance: progress in mechanical circulatory support. Cardiology clinics, 25(4):553–564, 2007.

[66] Ranjit John. Current axial-flow devices—the heartmate ii and jarvik 2000 left ventricular assist devices. In Seminars in thoracic and cardiovascular surgery, volume 20, pages 264–272. Elsevier, 2008.

[67] Eiki Tayama, Don B Olsen, Yukio Ohashi, Robert Benkowski, Deborah Morley, George P Noon, Yukihiko Nos´e, and Michael E DeBakey. The debakey ventricular assist device: current status in 1997. Artificial organs, 23(12):1113–1116, 1999.

[68] Georg M Wieselthaler, Heinrich Schima, Michael Hiesmayr, Richard Pacher, Gunther Laufer, George P Noon, Michael DeBakey, and Ernst Wolner. First clinical experience with the debakey vad continuous-axial-flow pump for bridge to transplantation. Circulation, 101(4):356–359, 2000.

[69] Robert K Jarvik. System considerations favoring rotary artificial hearts with blood-immersed bearings. Artificial Organs, 19(7):565–570, 1995.

[70] Shunsuke Saito, Taichi Sakaguchi, Shigeru Miyagawa, Yasushi Yoshikawa, Takashi Yamauchi, Takayoshi Ueno, Toru Kuratani, and Yoshiki Sawa. Biventricular support using implantable continuous-flow ventricular assist devices. The Journal of Heart and Lung Transplantation, 30(4):475–478, 2011.

[71] Stefan Christiansen, Alberto Perez-Bouza, Helmut Reul, and R¨udiger Autschbach. In vivo experimental testing of a microaxial blood pump for right ventricular support. Artificial organs, 30(2):94–100, 2006.

[72] Francis D Pagani. Continuous-flow rotary left ventricular assist devices with "3rd generation" design. In Seminars in thoracic and cardiovascular surgery, volume 20, pages 255–263. Elsevier, 2008.

[73] Daniel Timms. A review of clinical ventricular assist devices. Medical engineering & physics, 33(9):1041–1047, 2011.

[74] Richard Wampler, David Lancisi, Virote Indravudh, Raymond Gauthier, and Robert Fine. A sealless centrifugal blood pump with passive magnetic and hydrodynamic bearings. Artificial organs, 23(8):780–784, 1999.

[75] Kevin Bourque, Christopher Cotter, Charles Dague, Daniel Harjes, Onur Dur, Julien Duhamel, Kaitlyn Spink, Kelly Walsh, and Edward Burke. Design rationale and preclinical evaluation of the heartmate 3 left ventricular assist system for hemocompatibility. Asaio Journal, 62(4):375–383, 2016.

[76] Kevin Bourque, Charles Dague, David Farrar, Kelly Harms, Dan Tamez, William Cohn, Egemeun Tuzun, Victor Poirier, and O Howard Frazier. In vivo assessment of a rotary left ventricular assist device-induced artificial pulse in the proximal and distal aorta. Artificial organs, 30(8):638–642, 2006.

[77] Roland Hetzer, Thomas Krabatsch, Alexander Stepanenko, Ewald Hennig, and Evgenij V Potapov. Long-term biventricular support with the heartware implantable

continuous flow pump. The Journal of Heart and Lung Transplantation, 29(7):822–824, 2010.

[78] Martin Strueber, Anna L Meyer, Doris Malehsa, and Axel Haverich. Successful use of the heartware hvad rotary blood pump for biventricular support. The Journal of thoracic and cardiovascular surgery, 140(4):936, 2010.

[79] Jeffrey A LaRose, Daniel Tamez, Michael Ashenuga, and Carlos Reyes. Design concepts and principle of operation of the heartware ventricular assist system. Asaio Journal, 56(4):285–289, 2010.

[80] James K Kirklin, Francis D Pagani, Robert L Kormos, Lynne W Stevenson, Elizabeth D Blume, Susan L Myers, Marissa A Miller, J Timothy Baldwin, James B Young, and David C Naftel. Eighth annual intermacs report: special focus on framing

[81] Joseph C Cleveland Jr, David C Naftel, T Brett Reece, Margaret Murray, James Antaki, Francis D Pagani, and James K Kirklin. Survival after biventricular assist device implantation: an analysis of the interagency registry for mechanically assisted circulatory support database. The Journal of heart and lung transplantation, 30(8):862–869, 2011.

[82] Gianluca Torregrossa, Michiel Morshuis, Robin Varghese, Leila Hosseinian, Vladimiro Vida, Vincenzo Tarzia, Antonio Loforte, Daniel Duveau, Francisco Arabia, Pascal Leprince, et al. Results with syncardia total artificial heart beyond 1 year. Asaio Journal, 60(6):626–634, 2014.

[83] Marvin J Slepian, Richard G Smith, and Jack G Copeland. The syncardia cardiowest total artificial heart. FUNDAMENTAL AND CLINICAL CARDIOLOGY, 56:473, 2006.

[84] Paul Mohacsi and Pascal Leprince. The carmat total artificial heart, 2014.

[85] Carlo R Bartoli and Robert D Dowling. The future of adult cardiac assist devices: novel systems and mechanical circulatory support strategies. Cardiology clinics, 29(4):559–582, 2011.

[86] RT Kung, Long Sheng Yu, Burt D Ochs, Steven M Parnis, Michael P Macris, and OH Frazier. Progress in the development of the abiomed total artificial heart. ASAIO journal (American Society for Artificial Internal Organs: 1992), 41(3):M245–8, 1995.

[87] Daniel Timms, John Fraser, Mark Hayne, John Dunning, Keith McNeil, and Mark Pearcy. The bivacor rotary biventricular assist device: concept and in vitro investigation. Artificial organs, 32(10):816–819, 2008.

[88] Kiyotaka Fukamachi, David J Horvath, Alex L Massiello, Hideyuki Fumoto, Tetsuya Horai, Santosh Rao, and Leonard AR Golding. An innovative, sensorless, pulsatile, continuous-flow total artificial heart: device design and initial in vitro study. The Journal of Heart and Lung Transplantation, 29(1):13–20, 2010.

[89] Hideyuki Fumoto, David J Horvath, Santosh Rao, Alex L Massiello, Tetsuya Horai, Tohru Takaseya, Yoko Arakawa, Nicole Mielke, Ji-Feng Chen, Raymond Dessoffy, et al. In vivo acute performance of the cleveland clinic self-regulating, continuousflow total artificial heart. The Journal of Heart and Lung Transplantation, 29(1):21– 26, 2010.

[90] Daniela Rus and Michael T Tolley. Design, fabrication and control of soft robots. Nature, 521(7553):467, 2015.

[91] Ian D Walker. Continuous backbone "continuum" robot manipulators. Isrn robotics, 2013, 2013.

[92] Radosław Cie´slak and Adam Morecki. Elephant trunk type elastic manipulator-a tool for bulk and liquid materials transportation. Robotica, 17(1):11–16, 1999.

[93] Ian A Gravagne and Ian D Walker. Uniform regulation of a multi-section continuum manipulator. In Proceedings 2002 IEEE International Conference on Robotics and Automation (Cat. No. 02CH37292), volume 2, pages 1519–1524. IEEE, 2002.

[94] Michael W Hannan and Ian D Walker. Kinematics and the implementation of an elephant's trunk manipulator and other continuum style robots. Journal of robotic systems, 20(2):45–63, 2003.

[95] William McMahan, Bryan A Jones, and Ian D Walker. Design and implementation of a multi-section continuum robot: Air-octor. In 2005 IEEE/RSJ International Conference on Intelligent Robots and Systems, pages 2578–2585. IEEE, 2005.

[96] David B Camarillo, Christopher R Carlson, and J Kenneth Salisbury. Configuration tracking for continuum manipulators with coupled tendon drive. IEEE Transactions on Robotics, 25(4):798–808, 2009.

[97] Marcello Calisti, Andrea Arienti, Maria Elena Giannaccini, Maurizio Follador, Michele Giorelli, Matteo Cianchetti, Barbara Mazzolai, Cecilia Laschi, and Paolo Dario. Study and fabrication of bioinspired octopus arm mockups tested on a multipurpose platform. In 2010 3rd IEEE RAS & EMBS International Conference on Biomedical Robotics and Biomechatronics, pages 461–466. IEEE, 2010.

[98] Hesheng Wang, Weidong Chen, Xiaojin Yu, Tao Deng, Xiaozhou Wang, and Rolf Pfeifer. Visual servo control of cable-driven soft robotic manipulator. In 2013 IEEE/RSJ International Conference on Intelligent Robots and Systems, pages 57–62. IEEE, 2013.

[99] Pablo Valdivia y Alvarado and Kamal Youcef-Toumi. Design of machines with compliant bodies for biomimetic locomotion in liquid environments. Journal of dynamic systems, measurement, and control, 128(1):3–13, 2006.

[100] Andrew D Marchese and Daniela Rus. Design, kinematics, and control of a soft spatial fluidic elastomer manipulator. The International Journal of Robotics Research, 35(7):840–869, 2016.

[101] Panagiotis Polygerinos, Stacey Lyne, Zheng Wang, Luis Fernando Nicolini, Bobak Mosadegh, George M Whitesides, and Conor J Walsh. Towards a soft pneumatic glove for hand rehabilitation. In 2013 IEEE/RSJ International Conference on Intelligent Robots and Systems, pages 1512–1517. IEEE, 2013.

[102] Raphael Deimel and Oliver Brock. A novel type of compliant and underactuated robotic hand for dexterous grasping. The International Journal of Robotics Research, 35(1-3):161–185, 2016.

[103] Michael T Tolley, Robert F Shepherd, Bobak Mosadegh, Kevin C Galloway, Michael Wehner, Michael Karpelson, Robert J Wood, and George M Whitesides. A resilient, untethered soft robot. Soft robotics, 1(3):213–223, 2014.

[104] Andrew D Marchese, Cagdas D Onal, and Daniela Rus. Autonomous soft robotic fish capable of escape maneuvers using fluidic elastomer actuators. Soft Robotics, 1(1):75–87, 2014.

[105] Cagdas D Onal and Daniela Rus. Autonomous undulatory serpentine locomotion utilizing body dynamics of a fluidic soft robot. Bioinspiration & biomimetics, 8(2):026003, 2013.

[106] Koichi Suzumori, Satoshi Endo, Takefumi Kanda, Naomi Kato, and Hiroyoshi Suzuki. A bending pneumatic rubber actuator realizing soft-bodied manta swimming robot. In Proceedings 2007 IEEE International Conference on Robotics and Automation, pages 4975–4980. IEEE, 2007.

[107] Cagdas D Onal, Xin Chen, George M Whitesides, and Daniela Rus. Soft mobile robots with on-board chemical pressure generation. In Robotics Research, pages 525–540. Springer, 2017.

[108] Gregory McCarthy, Daniil Effraimidis, Brian Jennings, Nicholas Corso, Cagdas D Onal, and MB Popovic. Hydraulically actuated muscle (ham) exo-musculature. In Robot Makers: The Future of Digital Rapid Design and Fabrication of Robots"(RoMa) Workshop, 2014.

[109] Robert K Katzschmann, Andrew D Marchese, and Daniela Rus. Hydraulic autonomous soft robotic fish for 3d swimming. In Experimental Robotics, pages 405– 420. Springer, 2016.

[110] Panagiotis Polygerinos, ZhengWang, Kevin C Galloway, Robert JWood, and Conor J Walsh. Soft robotic glove for combined assistance and at-home rehabilitation. Robotics and Autonomous Systems, 73:135–143, 2015.

[111] Justin W Raade, Kurt R Amundson, and H Kazerooni. Development of hydraulic-electric power unit for mobile robots. In ASME 2005 International Mechanical Engineering Congress and Exposition, pages 27–34. American Society of Mechanical Engineers Digital Collection, 2005.

[112] Kurt Amundson, Justin Raade, Nathan Harding, and Hami Kazerooni. Hybrid hydraulic-electric power unit for field and service robots. In 2005 IEEE/RSJ International Conference on Intelligent Robots and Systems, pages 3453–3458. IEEE, 2005.

[113] Adam Zoss and H Kazerooni. Architecture and hydraulics of a lower extremity exoskeleton. In ASME 2005 International Mechanical Engineering Congress and Exposition, pages 1447–1455. American Society of Mechanical Engineers Digital Collection, 2005.

[114] Saeid Habibi and Andrew Goldenberg. Design of a new high performance electrohydraulic actuator. In 1999 IEEE/ASME International Conference on Advanced Intelligent Mechatronics (Cat. No. 99TH8399), pages 227–232. IEEE, 1999.

[115] Kyoung Kwan Ahn, Doan Ngoc Chi Nam, and Maolin Jin. Adaptive backstepping control of an electrohydraulic actuator. IEEE/ASME transactions on mechatronics, 19(3):987–995, 2013.

[116] Joerg Grabbel and Monika Ivantysynova. An investigation of swash plate control concepts for displacement controlled actuators. International journal of fluid power, 6(2):19–36, 2005.

[117] Sangok Seok, Cagdas Denizel Onal, Kyu-Jin Cho, Robert J Wood, Daniela Rus, and Sangbae Kim. Meshworm: a peristaltic soft robot with antagonistic nickel titanium coil actuators. IEEE/ASME Transactions on mechatronics, 18(5):1485–1497, 2012.

[118] Huai-Ti Lin, Gary G Leisk, and Barry Trimmer. Goqbot: a caterpillar-inspired soft-bodied rolling robot. Bioinspiration & biomimetics, 6(2):026007, 2011.

[119] Cecilia Laschi, Matteo Cianchetti, Barbara Mazzolai, Laura Margheri, Maurizio Follador, and Paolo Dario. Soft robot arm inspired by the octopus. Advanced Robotics, 26(7):709–727, 2012.

[120] Matteo Cianchetti, Tommaso Ranzani, Giada Gerboni, Thrishantha Nanayakkara, Kaspar Althoefer, Prokar Dasgupta, and Arianna Menciassi. Soft robotics technologies to address shortcomings in today's minimally invasive surgery: the stiff-flop approach. Soft robotics, 1(2):122–131, 2014.

[121] Marko B Popovic. Biomechatronics. Academic Press, 2019.

Chapter 2

Design, Dynamic Modelling and Experiment Validation of A Novel Alternating Flow Variable Displacement Hydraulic Pump

Mengtang Li[1], Ryan Foss[2], Kim Stelson[2], James Van De Ven[2], Eric Barth[1]

1. Vanderbilt University, Nashville, TN

2. University of Minnesota, Minneapolis, MN

From: *IEEE/ASME Transactions on Mechatronics*

Status: Accepted Jun 23, 2018; Published March 21, 2019.

2.1 Abstract

High power density, good controllability and low cost are the most appealing characteristics that make hydraulic systems the best choice for many applications. Current state of the art hydraulic variable displacement pumps show high efficiency at high displacement while they have poor efficiencies at low displacement. This paper proposes a novel alternating flow (AF) variable displacement hydraulic pump to 1) eliminate metering losses by acting as a high-bandwidth pump for displacement control, 2) achieve high efficiency across a wide range of operating conditions and displacements, and 3) allow multiple units to be easily common-shaft mounted for a compact multi-actuator displacement control system from a single prime-mover. A dynamic model using first principles describes the cylinder pressure, flows between pairs of cylinders, and net inlet and outlet flows as a function of the pump's phase shift angle. The model captures hydraulic check valve dynamics, the effective bulk modulus, leakage flows, and viscous friction. Piston kinematics and dynamics are discussed and energy loss models are presented. A first prototype of the AF pump was

constructed from two inline triplex pumps that were modified so that three piston pairs were created. Experiment tests were conducted and used to validate the model. After model validation, simulation results from the model can offer an initial evaluation of this novel pump concept and potential applications and can be used to guide the design for future prototype of the AF hydraulic pump.

2.2 Introduction

Traditional hydraulic circuits use metering valves to control the load, resulting in precise control and fast response. However, metering valve control results in significant energy dissipation, which is largely the reason that the average efficiency of hydraulic system is as low as 21% [1]. Load sensing (LS) circuits are widely used in industry to control the pressure source to match with the highest pressure load to minimize the throttling loss. An LS system does improve the system efficiency but when the required pressure levels from different loads are not close to each other, LS still suffers from throttling loss and poor efficiency. Instead of throttling the fluid and transforming the unnecessary power into heat, a more efficient alternative is to drive each actuator with a variable displacement pump and control the actuator with the pump displacement, termed displacement control [2]. An excavator employing displacement control with currently available variable pump/motors has experimentally demonstrated a 39% energy savings over throttling valve control in a load sensing circuit [3]. The modularity of displacement control brings another benefit. It makes the whole system more reliable than a single pump circuit with throttling valves. If one pump fails, the other axes are decoupled and still fully functional. Critical to displacement control is the performance and efficiency of the variable displacement pump across a wide range of displacements and pressures. For multi-actuator circuits, where multiple pumps are driven on a common shaft, the package size and weight of the pump are also important.

The family of variable positive displacement pumps includes: vane pump, axial piston

pump, bent axis pump, radial piston pump, along with some new architectures. Although much work has been done on improving the maximum efficiency of these variable displacement pumps [4-7], such pumps characteristically have low efficiency at low volumetric displacement since the largest energy losses do not scale with output power [8]. Axial piston pumps accommodate a through shaft, but are axially long making it challenging to common-shaft mount multiple pumps. Bent axis pumps are a variation of the axial piston machine with low piston side-loading, offering higher efficiencies. However, these pumps are typically more expensive and more complex and do not offer though shaft configurations. Vane pumps can also be variable, but incur high side loads on the pump shaft, operate at lower pressure levels, and have lower efficiency. Radial piston pumps are axially short and accommodate a through shaft, making them package well. They also are highly efficient and operate at higher pressures. However, currently, only few variable configurations are available beyond the Moog RKP, which also suffers from high shaft loads. Two relatively new architectures include the Artemis Digital Displacement® pump and the variable displacement linkage pump. The Artemis pump offers very high efficiencies and packages well due to its radial piston configuration. This pump however relies on the precise timing of inlet and outlet valves for fluid management. The variable displacement linkage pump uses a changing ground pivot of sixbar linkage to decrease swept volume while maintaining a constant dead/unswept volume. This pump offers very high efficiencies across a wide operating range but is bulky in the inline configuration and complex in the radial configuration [9].

An alternative to a mechanically variable displacement pump is to vary the flowrate of a fixed displacement pump through the speed control of an electric drive motor, known as electro-hydraulic actuator (EHA). While straightforward and more efficient, the high cost and lower power density of electronics restricts the usage of EHA [10]. The flowrate could also be controlled with high speed switching of digital valves, termed digital displacement. The most common approach to digital displacement is flow diverting, where the actively

controlled tank valve is held open for a portion of the upstroke of the piston, returning the fluid to tank. At a specified displacement fraction of the piston stroke, the tank valve is rapidly closed and the pressure valve is opened, sending flow to the load. While this approach eliminates the leakage and friction of the port plates of an axial piston or bent axis pump, it has several drawbacks. The valve transitions occur at high piston velocity, resulting in throttling energy loss across the partially open tank and pressure valves for a fraction of the piston stroke and generating water hammer creating noise and large flow pulsations [11, 12]. Viscous flow losses are incurred by pumping the unused flow back to tank, and there is a lack of digital valves with reasonable energy consumption that can switch fast enough for high-speed pumps.

Alternating flow hydraulics (AFH) is a special class of hydraulics characterized by the transmission of power with no net flow. Over the last century, work pertaining to AFH has been intermittent, beginning with Constantinesco's published work back in the early 1900's [13]. Weng developed a hybrid AFH-DC flow system called a pulsating flow system for the use of two different fluids [14]. Davis applied a lumped parameter transmission line method, commonly used in electrical systems, to AF hydraulic transmission [15]. And more recently, Marcu developed a prototype rotary hydraulic motor that is powered by alternating flow [16]. Although the geometry presented in the AF pump is to small for the effects of travelling pressure waves to be relevant, it nonetheless inspired the concept.

This paper proposes a novel AF hydraulic pump with the aim of eliminating throttling energy loss, having high efficiency across a wide range of operating conditions and displacements, and being compact to allow multiple units to be easily common-shaft mounted. In Chapter 2.3, the basic principles of the alternating flow (AF) hydraulic pump are presented. Next, dynamic models describing the cylinder pressure and flow rate between the connecting pipes are discussed in detail in Chapter 2.4. The model also captures hydraulic check valve dynamics and the effective bulk modulus. Chapter 2.5 describes an input motor torque model and various energy loss models. The construction of AF pump prototype 1

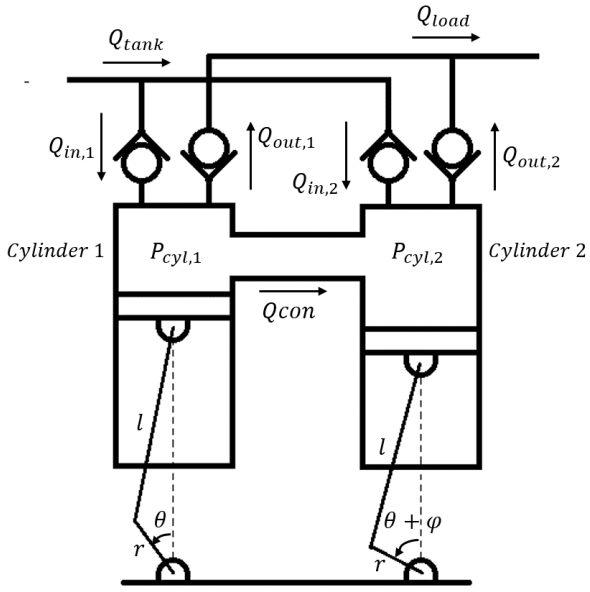

Figure 2.1: AF hydraulic pump concept.

along with experiment tests are presented in Chapter 2.6. Simulation results from the model are compared with experiment tests in Chapter 2.7 and a discussion follows in Chapter 2.8. Chapter 2.9 provides concluding remarks.

2.3 Alternating Flow Pump

The proposed AF hydraulic pump is formed by joining two radial piston pumps. Each pumping pair can be viewed as two sinusoidally-oscillating pistons of equal displacement with cylinders directly connected by a fluid conduit, as shown in Fig. 2.1. The output flow rate reaches a maximum when the motions of the two pistons are in phase. When the motions of the two pistons are 180 degrees out of phase, fluid is shuttled back and forth, resulting in zero net output flow rate. Continuously variable displacement is achieved through the variation of the phase shift angles between the pistons, as shown in Fig. 2.2.

The architecture of the radial piston pump provides AF hydraulic pump with several inherent benefits. First, it is one of the most efficient pump architectures of current the state of art. Second, it has a short axial compact size and can have a through shaft, which allows

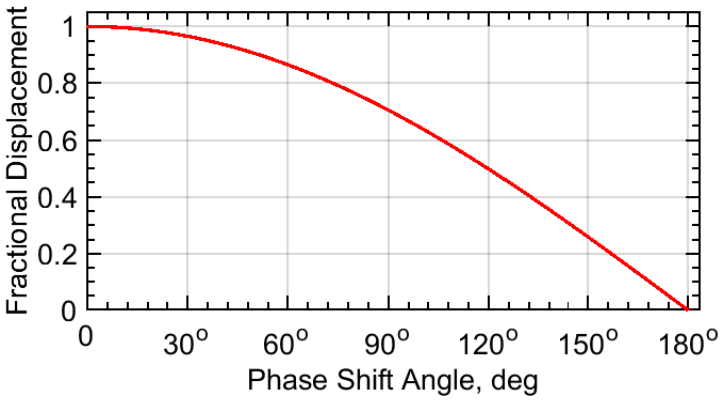

Figure 2.2: Variable displacement as a function of the phase shift angle.

multiple units to be common-shaft mounted to control a multiple actuator system. Third, with a multi-lobe cam, an AF hydraulic pump can achieve extremely high displacement density. The shift angle required for varying displacement is also reduced.

2.4 AF Pump Dynamic Model

A lumped parameter model is developed for each pair of pumping piston cylinders. A set of differential equations need to be solved numerically to obtain cylinder pressure $P_{cyl,i}$ in ith piston cylinder:

$$\dot{P}_{cyl,i} = \frac{\beta_{eff}}{V_{cyl,i}}(Q_{in,i} - Q_{out,i} - Q_{leak,i} - Q_{con} - \dot{V}_{cyl,i}) \tag{2.1}$$

where β_{eff} is the pressure-dependent effective bulk modulus, the inlet flow rate $Q_{in,i}$ is defined positive if oil flows into the cylinder, the output flow rate $Q_{out,i}$ is defined positive if oil flows out of the cylinder, leakage flow $Q_{leak,i}$ is assumed to be un-recoverable and the flow rate through the connecting pipe Q_{con} is defined positive if oil flows from cylinder 1 to cylinder 2.

A simple kinematic model is used in this paper to describe the motion of each piston.

The positions of piston 1 and piston 2 from the same pair are given by:

$$y_1 = r(1-\cos\theta) + l - \sqrt{l^2 - r^2\sin^2\theta} \tag{2.2}$$

$$y_2 = r(1-\cos(\theta+\phi)) + l - \sqrt{l^2 - r^2\sin^2(\theta+\phi)} \tag{2.3}$$

where θ is the rotated angle and ϕ is the phase shift angle.

Rotation of the first piston is assumed to start from its top dead center. The instantaneous volume for one pair of piston cylinders then is:

$$V = 2V_{tdc} + V_{con} + A_p(y_1 + y_2) \tag{2.4}$$

where V_{tdc} is the unswept dead volume of each cylinder chamber, V_{con} is the volume of the connecting pipe and A_p is the surface area of each piston.

For the sake of simplicity, Eqn. 2.4 can be approximated as follow if the connecting rod length l is at least 3 times longer than the crank radius r.

$$V = 2V_{tdc} + V_{con} + \frac{\pi d_p^2 r}{2}[1 - \cos\frac{\phi}{2}\cos(\theta + \frac{\phi}{2})] \tag{2.5}$$

where d_p is the diameter of the piston.

For a single cycle, the ideal output fluid volume is then:

$$V_{idealout} = max(V) - min(V) = \pi d_p^2 r\cos\frac{\phi}{2} \tag{2.6}$$

With Eqn. 2.6, the fractional displacement, X, of the AF pump can be obtained as follows:

$$X = \cos\frac{\phi}{2} \tag{2.7}$$

The total effective displacement D per revolution of the AF pump is then:

$$D = 2rnA_pX = \frac{\pi}{2}nd_p^2 r\cos\frac{\phi}{2} \tag{2.8}$$

where n is the number of pumping chambers (each with two pistons).

The change rates of cylinder volume of cylinder 1 and cylinder 2 from the same pair can be calculated by:

$$\dot{V}_{cyl,1} = A_p\omega r\left[1 + \frac{r\cos\theta}{\sqrt{l^2 - r^2\sin^2\theta}}\right] \tag{2.9}$$

$$\dot{V}_{cyl,2} = A_p\omega r\left[1 + \frac{r\cos(\theta+\phi)}{\sqrt{l^2 - r^2\sin^2(\theta+\phi)}}\right] \tag{2.10}$$

where ω is the pump rotating speed.

The bulk modulus is a fundamental property of fluid that represents the fluid's compressibility. Entrained and dissolved air in hydraulic oil can significantly change the numerical value of the bulk modulus. Many researches have been done to establish the model of effective fluid bulk modulus though definitions are not consistent. A good collection and comparison of those models is presented in [17] and the effective bulk modulus β_{eff} in this work is calculated by:

$$\beta_{eff} = \beta_0\left[\frac{(\frac{P_{cyl,i}}{P_o})^{\frac{1}{\gamma}}e^{\frac{P_o - P_{cyl,i}}{\beta}} + K}{(\frac{P_{cyl,i}}{P_o})^{\frac{1}{\gamma}}e^{\frac{P_o - P_{cyl,i}}{\beta}} + \frac{K}{\gamma}\frac{\beta_0}{P_{cyl,i}}}\right] \tag{2.11}$$

where β_0 is the bulk modulus of air free oil, P_o is the atmosphere pressure, γ is polytropic index for air/gas content, and K is entrained air fraction by volume.

2.4.1 Connecting Pipe Model

The two cylinders are directly connected with a pipe line, as shown in Fig. 2.1. A dynamic model for a short fluid pipeline with hydraulic resistance and inertance is established

to calculate the flow rate Q_{con}. The fluid is assumed to be incompressible and inviscid in the connecting pipe line. This assumption is valid since the volume of the connecting pipe is small.

The pressure drop introduced by the connecting pipe hydraulic inertance I is calculated by:

$$\Delta P_I = I\dot{Q}_{con} \tag{2.12}$$

$$I = \frac{\rho l_{con}}{A_{con}} \tag{2.13}$$

where $\dot{Q}_{con}$ is the rate of change of flowrate in the connecting pipe, ρ is the oil density, l_{con} and A_{con} are the effective length and cross sectional area of the connecting pipe, respectively.

The Reynolds number condition for a Laminar flow in the connecting pipe is given by:

$$Re_{con} = \frac{4\rho Q_{con}}{\pi\mu d_{con}} < 2300 \tag{2.14}$$

where Q_{con} is the flowrate in the connecting pipe, μ is the oil dynamic viscosity, and d_{con} is the diameter of the cross sectional area of the connecting pipe.

The hydraulic resistance R and therefore the pressure drop introduced by the connecting pipe resistance can be calculated by:

$$\Delta P_R = RQ_{con} \tag{2.15}$$

$$R = \frac{128\mu l_{con}}{\pi d_{con}^4} \tag{2.16}$$

The dynamic equation for the flow rate between each pair of cylinders can then be presented by:

$$\dot{Q}_{con} = \frac{1}{I}(P_{cyl,1} - P_{cyl,2} - \Delta P_R) \tag{2.17}$$

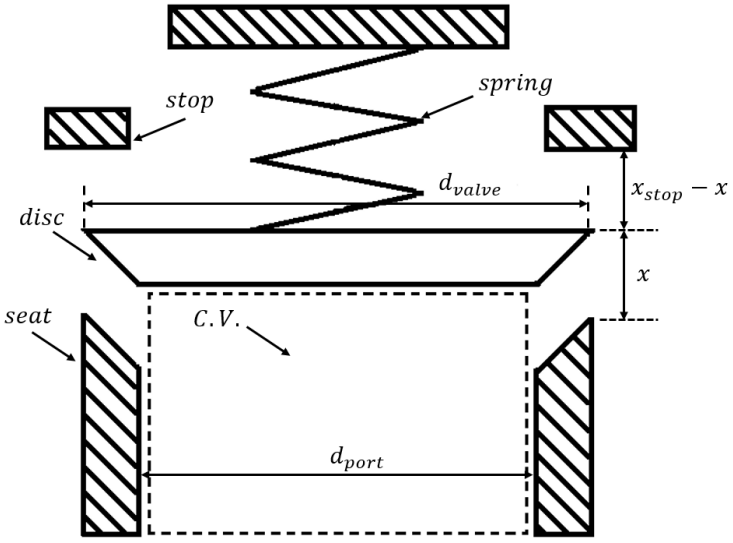

Figure 2.3: Disc style check valve concept.

2.4.2 Check Valve Model

A check valve is a passive flow control hydraulic device that ideally allows only unidirectional flow. The disc style check valve, shown in Fig. 2.3, utilizes a spring to seat a disc, which is of low mass and is able to respond quickly.

The dynamic motion equation for the disc is given by applying Newton's second law:

$$m_{disc}\ddot{x} = F \tag{2.18}$$

where m_{disc} is the mass of the check valve disk, x is the position of the disc and F is the summation of all external forces acting on the disc surface area A_{valve}. The main forces are hydraulic pressure force, $F_{pressure}$, spring force, F_{spring}, and seat/stop contact force, $F_{contact}$. Other external forces including stiction and flow force are negligible in general cases [18].

The pressure force $F_{pressure}$ acting on the disc is introduced by the pressure difference across the check valve disc:

$$F_{pressure} = \Delta P A_{valve} \tag{2.19}$$

For the inlet check valve:

$$\Delta P_{in} = P_{tank} - P_{cyl,i} \tag{2.20}$$

For the outlet check valve:

$$\Delta P_{out} = P_{cyl,i} - P_{load} \tag{2.21}$$

The spring force F_{spring} is calculated by:

$$F_{spring} = -k_{spring}(x + x_{preload}) \tag{2.22}$$

The allowable disc position is limited by the check valve seat ($x = 0$) and stop ($x = x_stop$). The contact force is modelled as the summation of elastic forces and dissipative reaction forces [18].

$$F_{contact} = \begin{cases} -k_{seat}x - C_{seat}\dot{x} & \text{, if } x < 0 \\ 0 & \text{, if } 0 \leq x \leq x_{stop} \\ -k_{stop}(x - x_{stop}) - C_{stop}\dot{x} & \text{, if } x > x_{stop} \end{cases} \tag{2.23}$$

where the k_{seat}, C_{seat}, k_{stop}, and C_{stop} are check valve seat/stop spring stiffness and check valve seat/stop damping coefficient respectively.

With Eqn. 2.18 solved, the ring shape check valve orifice area $A_{valve}(x)$ can be expressed as a function of disc position x:

$$A_{valve}(x) = max(0, \pi d_{port} x) \tag{2.24}$$

The discharge coefficient of the check valve, C_{dvalve}, depends on check valve Reynolds number, Re_{valve}. An empirical model is presented in [19] and a nonlinear least square

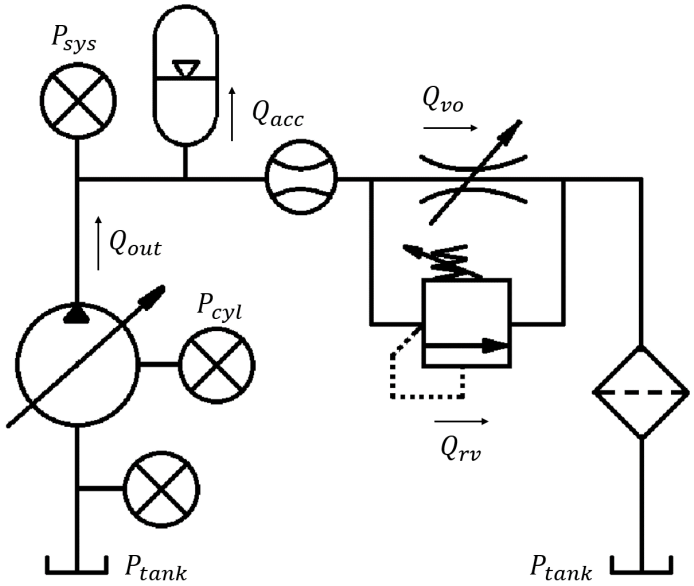

Figure 2.4: Schematic of the experimental test setup.

experimental result is given in [18].

$$Re_{valve} = \frac{4\rho Q_{valve}}{\pi \mu d_{port}} \tag{2.25}$$

$$C_{dvalve} = 0.79 - 0.87e^{-0.11\sqrt{Re_{valve}}} + 0.087e^{-0.95\sqrt{Re_{valve}}} \tag{2.26}$$

With all necessary equations solved, the inlet flow rate from ith piston cylinder $Q_{in,i}$ is:

$$Q_{in,i} = C_{dvalvein} A_{valvein} \sqrt{\frac{2}{\rho} \Delta P_{in}} \tag{2.27}$$

Similarly, the output flow rate from ith piston cylinder $Q_{out,i}$ is:

$$Q_{out,i} = C_{dvalveout} A_{valveout} \sqrt{\frac{2}{\rho} \Delta P_{out}} \tag{2.28}$$

2.4.3 Load Model

A simple hydraulic circuit is set up for experimental tests, shown in Fig. 2.4. A nitrogen gas accumulator is pre-charged to regulate the downstream pressure P_{load}, which is adjusted by a variable orifice (VO) placed in parallel with a pressure relief valve. A bi-directional flow meter is placed downstream before the VO. The total output flow rate from the AF pump, Q_{out}, is the summation of all pairs of piston cylinders:

$$Q_{out} = \sum Q_{out,i} \tag{2.29}$$

The flow rate relation is obtained by applying law of mass conservation with the assumption of incompressible flow:

$$Q_{out} = Q_{acc} + Q_{vo} \tag{2.30}$$

where Q_{acc} is the flow rate into the accumulator and Q_{vo} is the flow rate through the VO. A simple orifice model is used to model VO and its valve area A_{vo} is adjusted in such a way that the pressure is not high enough to open the pressure relief valve.

$$Q_{vo} = C_d A_{vo} \sqrt{\frac{2}{\rho}(P_{load} - P_{tank})} \tag{2.31}$$

The nitrogen gas in the accumulator is assumed to be adiabatic during compression and expansion and the hydraulic fluid is assumed to be incompressible compared with nitrogen gas. Then the load pressure P_{load} can be calculated by:

$$\dot{V}_{acc} = -Q_{acc} \tag{2.32}$$

$$P_{load} = P_{charge}\left(\frac{V_{charge}}{V_{acc}}\right)^{\gamma} \tag{2.33}$$

where V_{charge} and V_{acc} are accumulator pre-charge gas volume and instantaneous accumulator gas volume.

2.5 Energy Model

For the AF hydraulic pump, four types of energy losses are considered: leakage loss across the piston cylinder gap, viscous friction loss between piston and cylinder wall, check valve throttling loss and connecting pipe resistance loss. Note that the mechanical losses in the pump mechanism are neglected since this is not inherent to the concept. The motion of each piston is assumed to be only along the stroke direction, resulting in a constant gap height.

2.5.1 Leakage Loss Model

Leakage flow through the gap between the piston and the cylinder is created by a pressure drop across the piston. The leakage flow rate from ith piston cylinder is given by [20]:

$$Q_{leak,i} = \frac{\pi d_p h_p^3}{12 \mu l_p} (P_{cyl,i} - P_o) \tag{2.34}$$

where h_p is piston cylinder gap height and l_p is piston length.

Leakage energy loss from ith piston cylinder $E_{leak,i}$ can be obtained by integrating the product of leakage flow rate $Q_{leak,i}$ and cylinder pressure $P_{cyl,i}$ with respect to time:

$$E_{leak,i} = \int (P_{cyl,i} - P_o) Q_{leak,i} dt \tag{2.35}$$

2.5.2 Viscous Friction Loss Model

Viscous friction is introduced by shearing of the fluid between the piston and the cylinder. The viscous friction of ith piston cylinder is given by:

$$F_{viscous,i} = \frac{\pi d_p l_p \mu}{h_p} \dot{y}_i \tag{2.36}$$

where $\dot{y}_i$ is the velocity of the ith piston.

Viscous friction energy loss from ith piston cylinder $E_{viscous,i}$ can be obtained by integrating the product of viscous friction force $F_{viscous,i}$ and velocity of the ith piston $\dot{y}_i$ with respect to time:

$$E_{viscous,i} = \int F_{viscous,i} \dot{y}_i dt \tag{2.37}$$

2.5.3 Check Valve Throttling Loss Model

Conventionally used check valves in hydraulic pumps inevitably introduce throttling losses. The instantaneous power of throttling for an inlet check valve is:

$$\mathbb{P}_{throt,in,i} = \Delta P_{in} Q_{in,i} \tag{2.38}$$

Similarly, the instantaneous power of throttling for an outlet check valve is

$$\mathbb{P}_{throt,out,i} = \Delta P_{out} Q_{out,i} \tag{2.39}$$

The throttling energy loss can then by calculated by integrating the instantaneous power with respect to time:

$$E_{throt} = \int \mathbb{P}_{throt} dt \tag{2.40}$$

2.5.4 Connecting Pipe Loss Model

Energy loss associated with connecting pipe E_{con} is calculated by integrating the product of the pressure difference across the cinnecting pipe resistance RQ_{con} and the flowrate through the connecting pipe Q_{con} with respect to time:

$$E_{con} = \int RQ_{con}^2 dt \tag{2.41}$$

2.5.5 Input Motor Torque Model

With the input crank angle θ known, the velocity and the acceleration of the ith piston can be calculated by

$$\dot{y}_i = r\dot{\theta}\sin\theta + \frac{r^2\dot{\theta}\sin 2\theta}{2\sqrt{l^2 - r^2\sin^2\theta}} \tag{2.42}$$

$$\ddot{y}_i = r\dot{\theta}^2\cos\theta + \frac{r^2}{2}\frac{4\dot{\theta}^2\cos 2\theta(l^2 - r^2\sin^2\theta) + r^2\dot{\theta}^2\sin^2 2\theta}{2(l^2 - r^2\sin^2\theta)^{3/2}} \tag{2.43}$$

where a constant crank shaft speed assumption is made. This is a valid assumption for a high angular velocity and a crank shaft with sufficient inertia.

The dynamic motion equation for the piston is given by applying Newton's second law:

$$m_{piston}\ddot{y}_i = F \tag{2.44}$$

where m_{piston} is the mass of the piston, F is the summation of all external forces. To simplify the model while maintaining accuracy, only cylinder pressure force $F_{cyl,i}$, atmospheric force F_{atmo}, viscosity force $F_{viscous,i}$ and rod force $F_{rod,i}$ acting on the ith piston are considered.

The instantaneous hydraulic cylinder pressure force $F_{pressure,i}$ acting on the ith piston is calculated by:

$$F_{pressure,i} = P_{cyl,i}A_p \tag{2.45}$$

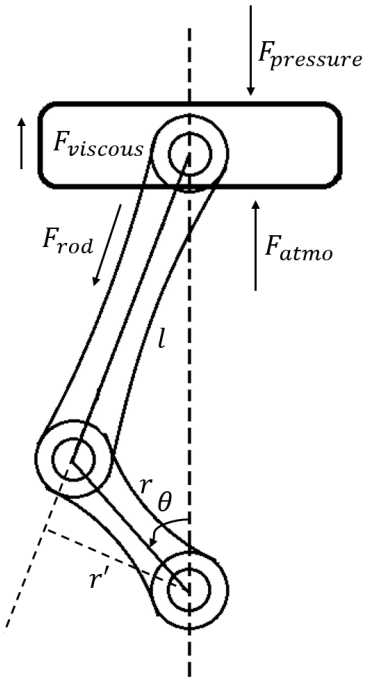

Figure 2.5: Piston force diagram.

The atmospheric pressure force F_{atmo} only acting on the other side of the ith piston is calculated by:

$$F_{atmo,i} = P_{atmo} A_p \tag{2.46}$$

The viscous friction force $F_{viscous,i}$ always acts along the opposite direction of the velocity of the ith piston. The rod force $F_{rod,i}$ can therefore be calculated with Eqn. 2.44 and the input motor torque T_i to drive ith piston can therefore be given by:

$$T_i = F_{rod} r_i' \tag{2.47}$$

The total input motor torque is therefore the summation of all T_i:

$$T_{motor} = \sum T_i \tag{2.48}$$

2.5.6 AF Pump Efficiency

All mechanical transmission torques, T_{trans}, are assumed to be constant and are out of the consideration of this design. The mechanical transmission work is calculated by:

$$W_{trans} = \int \omega T_{trans} dt \tag{2.49}$$

The total input work is calculated as:

$$W_{in} = \int \omega T dt = \int \omega (T_{motor} + T_{trans}) dt \tag{2.50}$$

The output fluid work is calculated as:

$$W_{out} = \int Q_{out} P_{load} dt \tag{2.51}$$

With input motor work and output fluid work determined, the total pump efficiency can be defined as:

$$\eta_{pump} = \frac{W_{out}}{W_{in}} \tag{2.52}$$

2.6 AF Pump Prototype

To demonstrate the concept of the AF pump and validate the model developed previously, a prototype pump was designed, assembled and tested. Instead of creating a complex device from scratch, a simplified version is preferred for the proof-of-concept prototype.

2.6.1 Methods

As shown in Fig. 2.6. Two 3CP1120 Cat Pump®pumps were placed face to face with the crankshaft from one of them being reversed to synchronize the crankshaft rotation direction. Holes were drilled on top of each pair of cylinder chambers. A short hydraulic

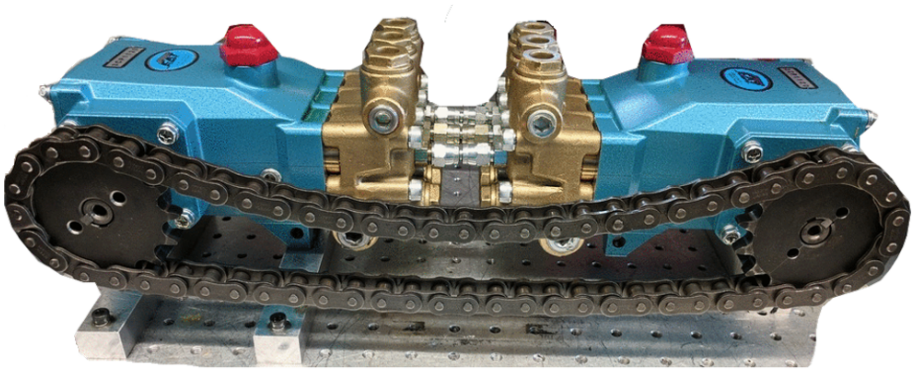

Figure 2.6: Alternating flow pump prototype 1 created from two triplex piston pumps.

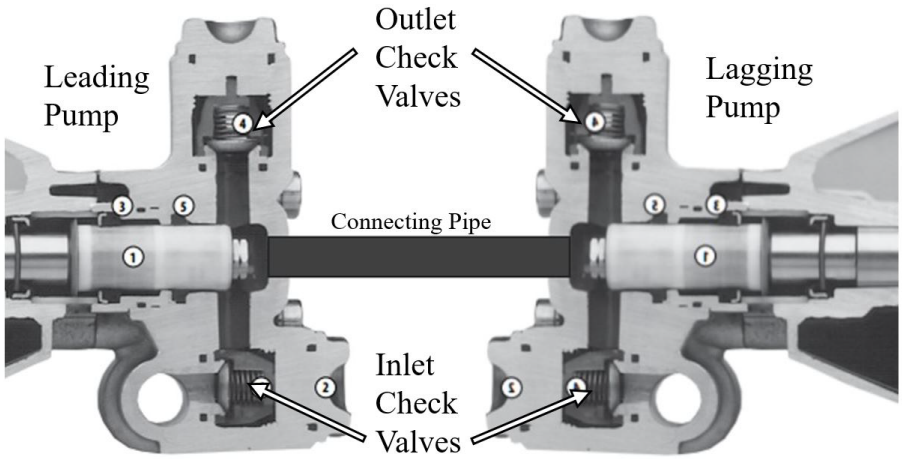

Figure 2.7: Cross section view of the two connected triplex piston pumps.

rigid pipe was used to connect each pair of cylinders. The cross sectional view of this arrangement is shown in Fig. 2.7. To connect the two rotating crankshafts, a chain-and-sprocket transmission was used. To maintain tension on the chain, an adjustable idler gear is rigidly mounted halfway between the two pumps. The chain-and-sprocket allows for the measurement and adjustment of the phase angle between the pumps, although this requires disassembling the transmission. This disassembly requirement does not allow real time adjustment of the phase which will be addressed in future prototypes. The detailed specifications of the prototype are given in Tab. 2.1.

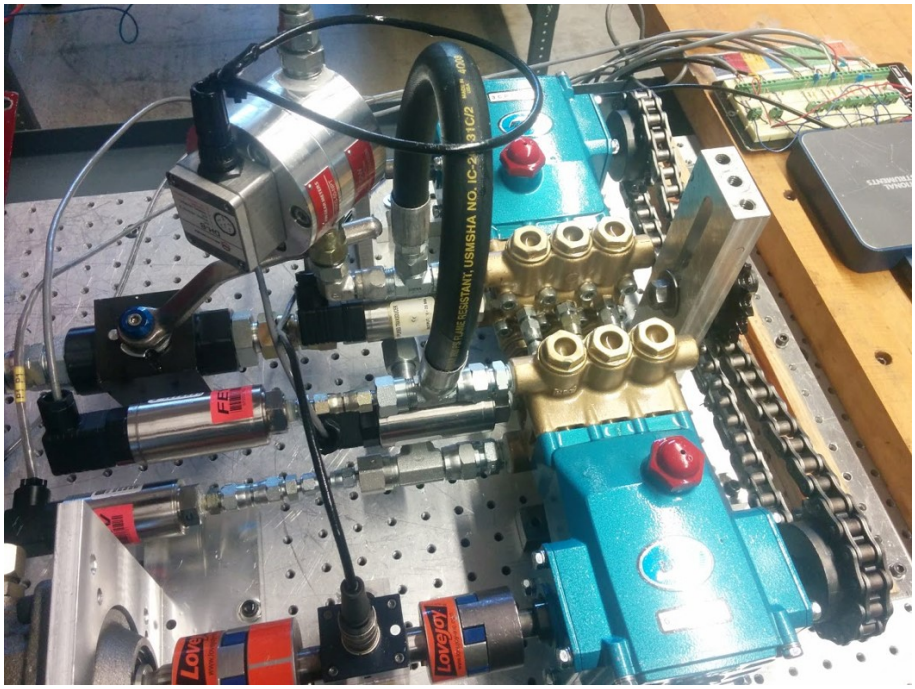

Figure 2.8: First generation prototype of AF pump used for experiment validation.

2.6.2 Experiment Setup

An experiment was devised to test the prototype pump and compare the simulated and measured efficiencies and dynamics. A schematics of the experiment system is shown in Fig. 2.4 and a diagram of the experiment showing the location of the various sensors and hydraulic components is shown in Fig. 2.8. A nitrogen gas accumulator was pre-charged to regulate the downstream system pressure, which can be adjusted by a variable orifice (VO). A pressure relief valve was placed in parallel with the VO. The inlet pressure, the output pressure and the pressure in the individual piston cylinder pairs were measured by Honeywell®pressure transducers. Do note the two pressure transducers protruding from the side of the manifolds are to measure the pressure in each chamber of the piston pair and validate the pressure drop across the connecting pipe predicted by the model. The input motor torque was measured with a Futek®TRS300 transducer and the rotary speed was measured with US Digital®HB6M rotary encoder. An AW Lake®gear flow meter measured the average output flow rate.

Table 2.1: Prototype Spec Table

Symbol	Description	Value
C_{seat}	Check valve seat damping coefficient	$10^4 Ns/m$
C_{stop}	Check valve stop damping coefficient	$10^4 Ns/m$
d_{con}	Connecting pipe diameter	$4.2mm$
d_p	Piston diameter	$17.6mm$
d_{port}	Check valve port diameter	$8.2mm$
d_{valve}	Check valve disk diameter	$10.7mm$
h_p	Piston cylinder gap height	$9\mu m$
k_{seat}	Check valve seat spring stiffness	$10^9 N/m$
k_{stop}	Check valve stop spring stiffness	$10^9 N/m$
k_{spring}	Check valve spring stiffness	$200N/m$
l	Connecting rod length	$43.81mm$
l_{con}	Connecting pipe length	$50mm$
l_p	Piston length	$10mm$
m_{disc}	Mass of the check valve disc	$5g$
m_{piston}	Mass of the cylinder piston	$50g$
r	Crank radius	$6.35mm$
V_{tdc}	Cylinder top dead volume	$7.95cm^3$
$x_{preload}$	Check valve spring preload	$6mm$
x_{stop}	Maximum check valve displacement	$3.52mm$

Experiments were run at a variety of phase shift angles and speeds. The different phase angles were realized by disassembling the chain-and-sprocket transmission and rotating one of the sprockets on its associated crankshaft. The speed of the pump was managed by a hydraulic motor which was controlled by a flow control valve. To measure the crankshaft angle of each pump, a block with dowel pins was slid into a pair of the machined holes in the sprocket mounted to the crankshaft. The machined holes align with the keyway of the crankshaft at TDC of cylinder 1. A digital angle gauge was used to measure the angle of the leading crankshaft and the lagging crankshaft and the difference between the two was the phase shift. This fixture is shown in Fig. 2.9. The pressure, flowrate, torque, and optical

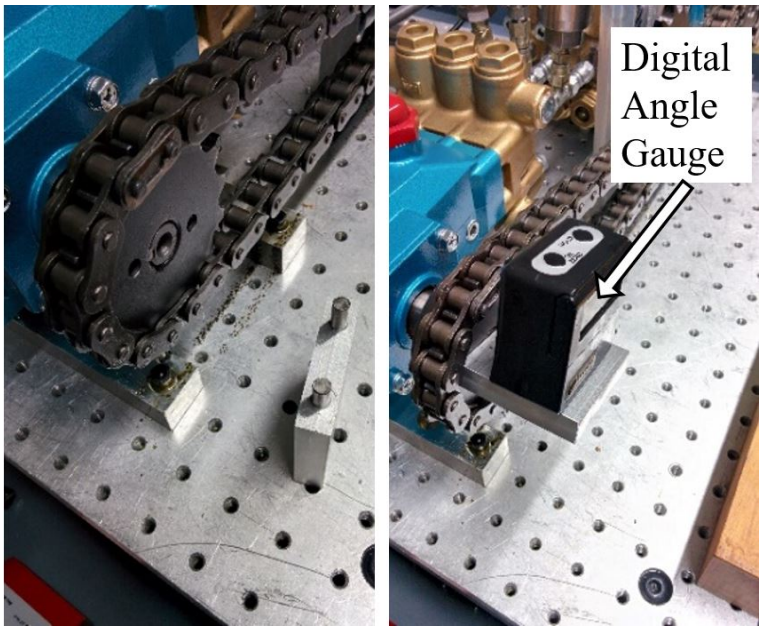

Figure 2.9: Phase measuring fixture for AF pump.

encoder sensors were all read with a PCIe-6353 National Instruments®DAQ board on a desktop computer. A series of experiments were run at all discrete phase angles achievable with the chain and sprocket. Once the transmission was installed and the phase angle was measured, the pump was driven by a hydraulic motor controlled with a flow control valve. For each experiment, the speed of the pump and load had to be set simultaneously due to the load being an adjustable orifice. Once the speed and pressure were set, the DAQ acquired data for 3 seconds after the system reaches a steady state at a rate of $10Ks/s$.

The measured system pressure, flowrate, input torque, and shaft speed are used to calculate the total efficiency of the pump, given as:

$$\eta_{pump} = \eta_m \eta_v \tag{2.53}$$

$$\eta_m = \frac{P_{load} D}{2\pi T} \tag{2.54}$$

$$\eta_v = \frac{2\pi Q_{out}}{\omega D} \tag{2.55}$$

where η_m is the mechanical efficiency and η_v is the volumetric efficiency.

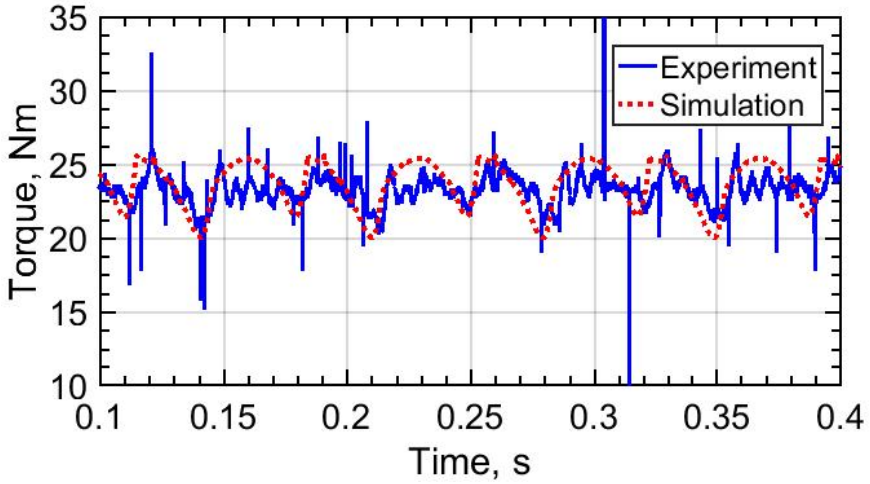

Figure 2.10: Input motor torque comparison between experiment tests and model predictions at 2 degree phase shift angle.

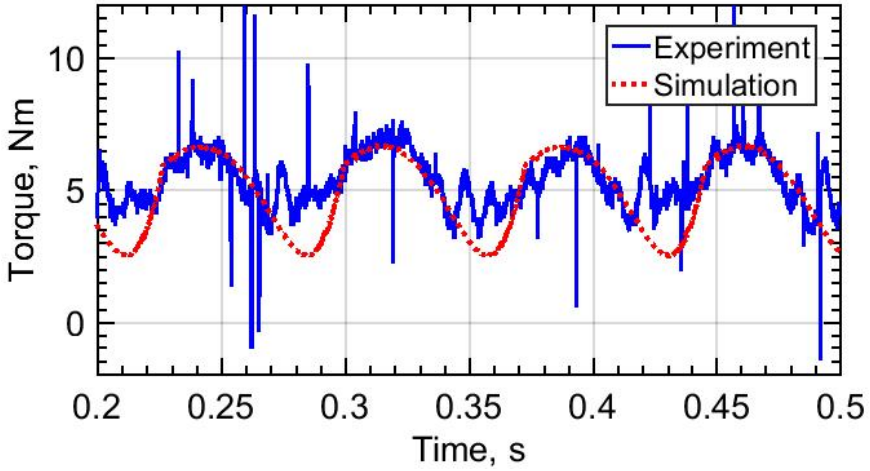

Figure 2.11: Input motor torque comparison between experiment tests and model predictions at 165 degree phase shift angle.

2.7 Model Validation

A series of experiments were conducted with various operating conditions and displacements. The crankshaft speed varied from $4.167Hz$ ($250rpm$) to $16.667Hz$ ($1000rpm$) while the system pressure was held constant at $6.895MPa$ ($1000psi$). The achievable phase shift angles were determined by the number of teeth of on the sprockets. The minimum available phase angle was 2 degrees and the maximum was 165 degrees.

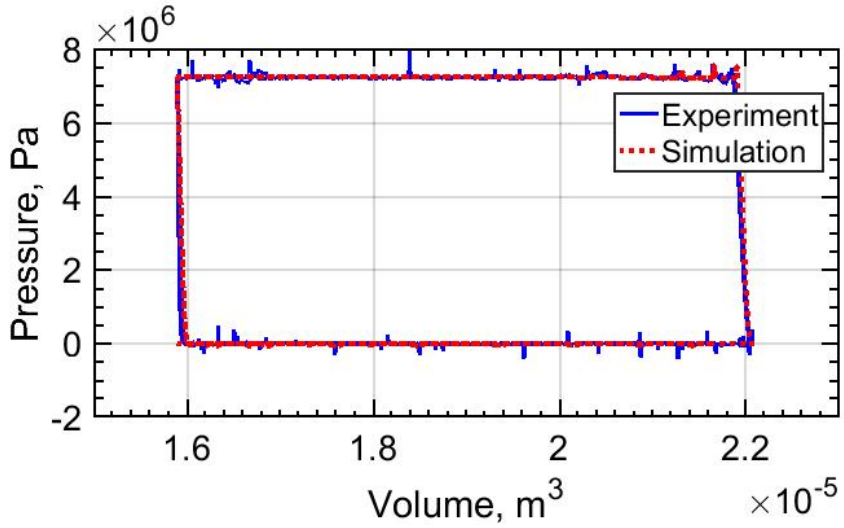

Figure 2.12: PV curve comparison between experiment tests and model predictions at 2 degree phase shift angle.

Two different torque versus time curves are shown in Fig. 2.10 and Fig. 2.11 under the operating condition of 4.167Hz (250rpm) and 6.895MPa (1000psi), with phase shift angle of 2 degrees and 165 degrees respectively. The dynamic model for the input torque correlates well with the experimental results. As can be shown from the comparison between Fig. 2.10 and Fig. 2.11, the motor driving torque required reduces as the phase shift angle increases. This can be explained by the motoring effect introduced by the connecting pipe mechanism.

Two different pressure versus volume curves are shown in Fig. 2.12 and Fig. 2.13, both showing a full cycle of the AF pump operating at 4.167Hz (250rpm) and 6.895MPa (1000psi), with phase shift angle of 2 degrees and 165 degrees respectively.

The model agrees well with the pressure vs. volume plots except for the 165 degree case once the pressure in the chamber starts to decrease, as shown in the top-left portion of Fig. 2.13. Some insight into what may be happening at this point in the cycle can be seen in Fig. 2.14 where about halfway through the compressed volume cycle there is a dip in pressure of 1MPa (145psi). The numerical model was not able to capture this effect well, which is evident in the pressure versus volume curves, but does not affect the measured

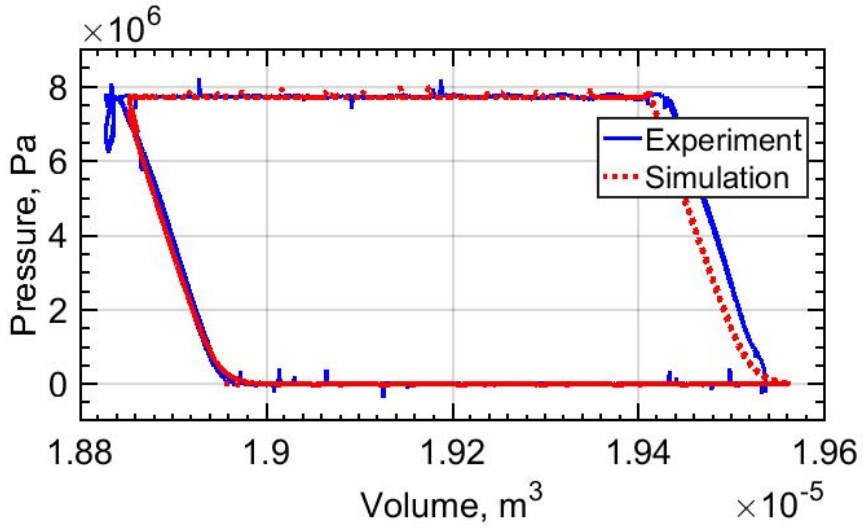

Figure 2.13: PV curve comparison between experiment tests and model predictions at 165 degree phase shift angle.

and modelled energy curves. This is likely due to the piston motion not being perfectly sinusoidal due to the kinematics of the crank-slider a slight negative change in the total volume of the two cylinders at the high phase shift angle.

Figure 2.15 compares the input motor torque work done in 0.5 seconds from the experimental measures and from the previously described model. Figure 2.16 shows the output fluid energy in 0.5 seconds from experimental measures and from the model. As can be seen from Fig. 2.15 and Fig. 2.16, the model shows close agreement to the experiment results for both input and output energy. The reason behind the unevenness of the efficiency curves is that for each conducted test, the shaft speed and the system pressure varied around the nominal values due to the coarse control of the experimental setup.

The input model matches with experiment data closer than the output model does for all operating conditions and displacements. This is mainly because the input model depends on the experimental system pressure and crankshaft speed data. The output model is capable of matching with experiment data for most of the operating conditions and displacements while the discrepancies become bigger as the phase shift angle becomes higher. Many things can attribute to this phenomenon. First of all, the inaccuracy of the simple crank

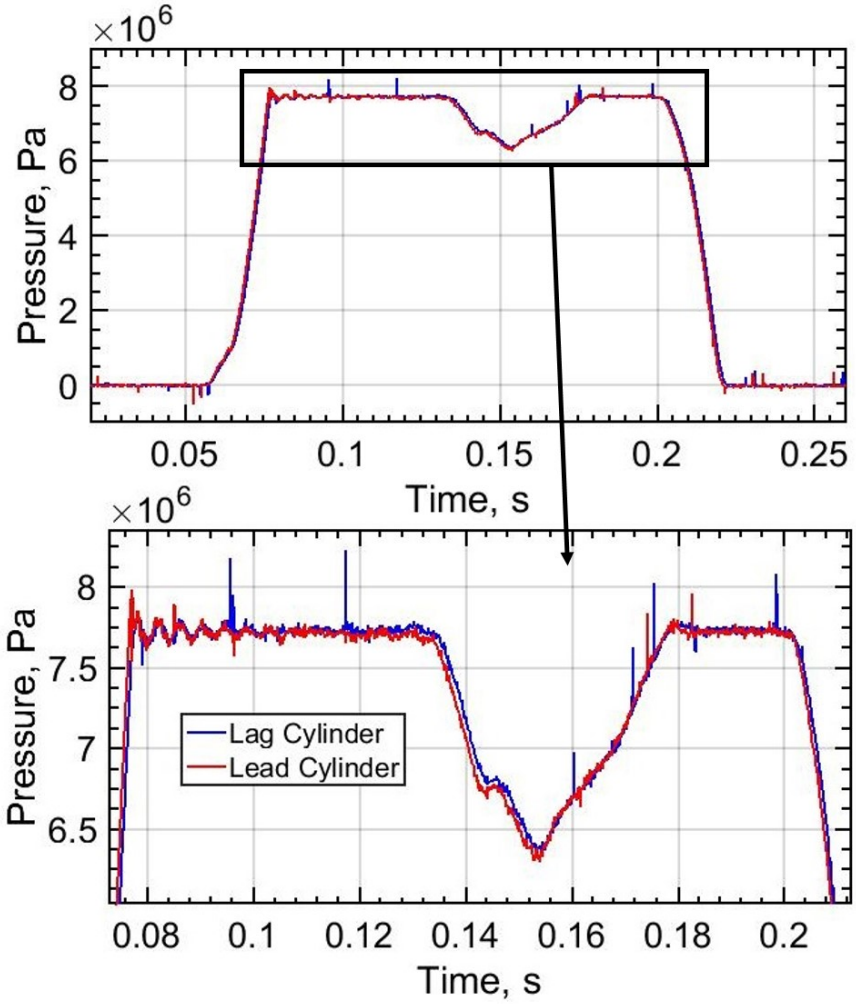

Figure 2.14: Pressure signal at either end of connecting pipe for 165 degree phase shift angle.

slider motion model increases as the phase shift angle approaches to 180 degrees. The model predicted output flowrate then diverges from the experimental data, which is shown in Fig. 2.17. Secondly, for simplicity, two inline triplex water pumps with bigger unswept dead volume, compared with normal hydraulic pumps, were chosen to build the prototype. As the displaced volume compared with the cylinder volume is quite small at the high phase shift angle, the inaccuracies in the predicted fluid effective bulk modulus become magnified. Thirdly, at high phase angle, the actual geometry structure of the connecting pipe introduces complicated dynamic and a more complex model is needed to accurately

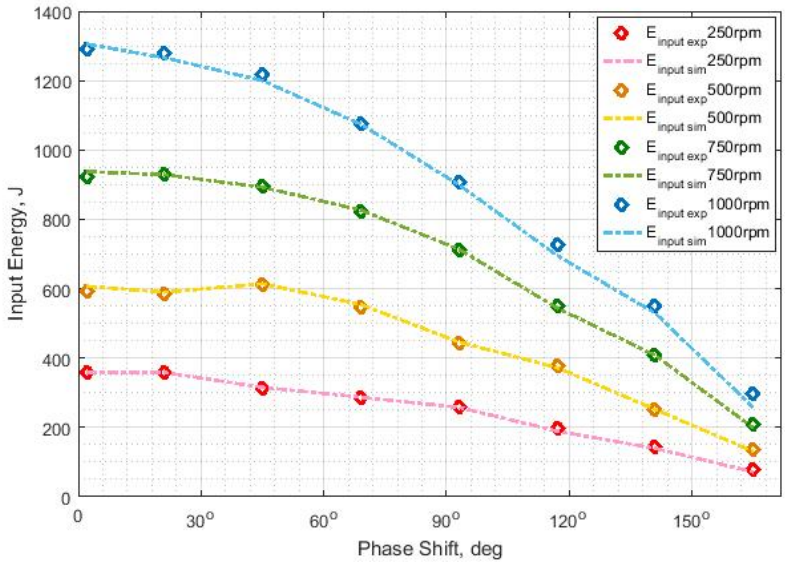

Figure 2.15: Input energy comparison between experiment tests and model predictions.

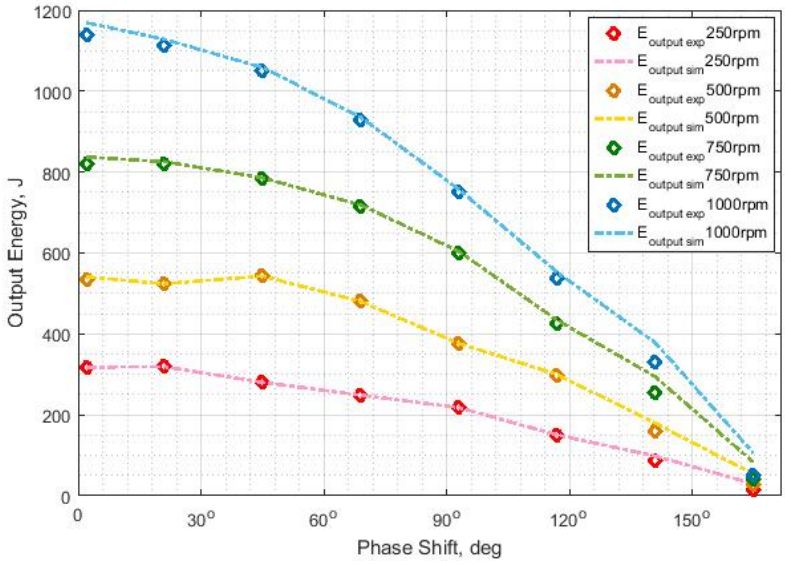

Figure 2.16: Output energy comparison between experiment tests and model predictions.

describe it.

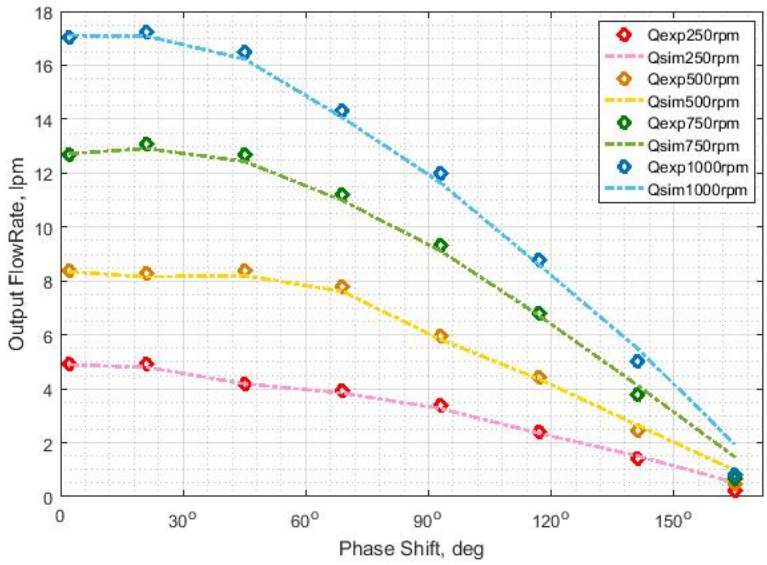

Figure 2.17: Output flowrate comparison between experiment tests and model predictions.

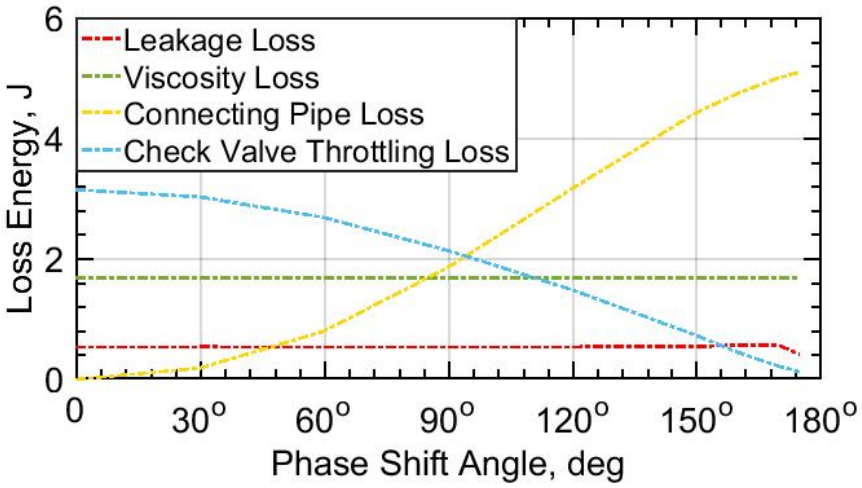

Figure 2.18: Four types of energy loss v.s. phase shift angle.

2.8 Discussion

With the dynamic model validated, it can be used to explore the parameter space and guide design optimization of future generation prototypes.

Although the connecting pipe offers a mechanism for two piston cylinders to balance their pressure levels, some energy is dissipated in the form of hydraulic resistance. Figure 2.18 plots the four modeled energy losses accumulated in 0.5 seconds versus different phase

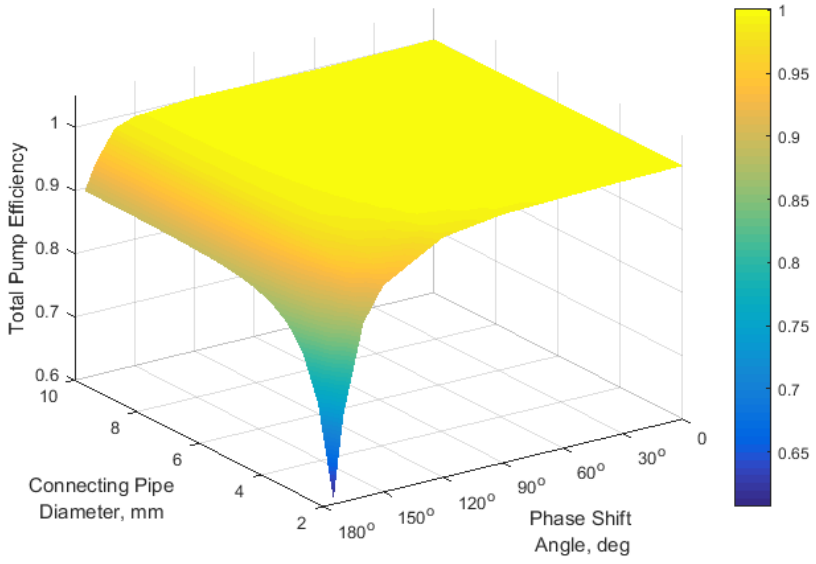

Figure 2.19: Model predicted efficiency v.s. phase shift angle and connecting pipe diameter.

shift angles. It can be seen that the hydraulic resistance loss introduced by the connecting pipe is a function of the phase shift angle ϕ. Also note that the check valve throttling loss drops as the phase shift angle increases. These phenomena agree to the basic principles of the AF hydraulic pump since more fluid is shuttled through the connecting pipe at higher phase shift angles.

Note that many different types of mechanical losses exist in the transmission parts of every hydraulic pump and huge chain-and-sprocket was used in this first generation prototype AF pump. Therefore, those mechanical transmission losses are not in the scope of design consideration and are neglected here.

To optimize the connecting pipe structure of the AF hydraulic pump, the model predicted pump efficiency is plotted in Fig. 2.19 against various phase shift angles and different connecting pipe diameters ranging between 2*mm* and 10*mm* with a constant connecting pipe length of 50*mm*. Figure 2.20 plots the model predicted pump efficiency versus various phase shift angles and different connecting pipe lengths ranging from 10*mm* to 150*mm* with a constant connecting pipe diameter of 4.2*mm* under the same operating pressure and

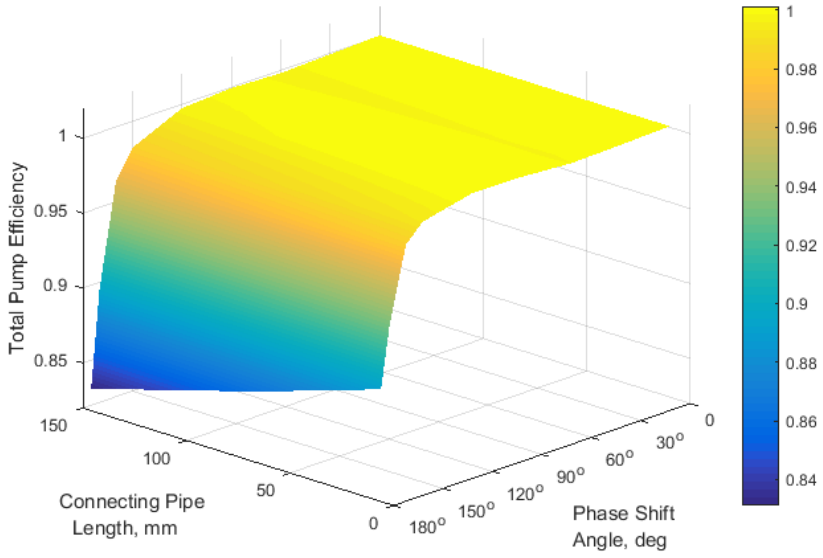

Figure 2.20: Model predicted efficiency v.s. phase shift angle and connecting pipe length.

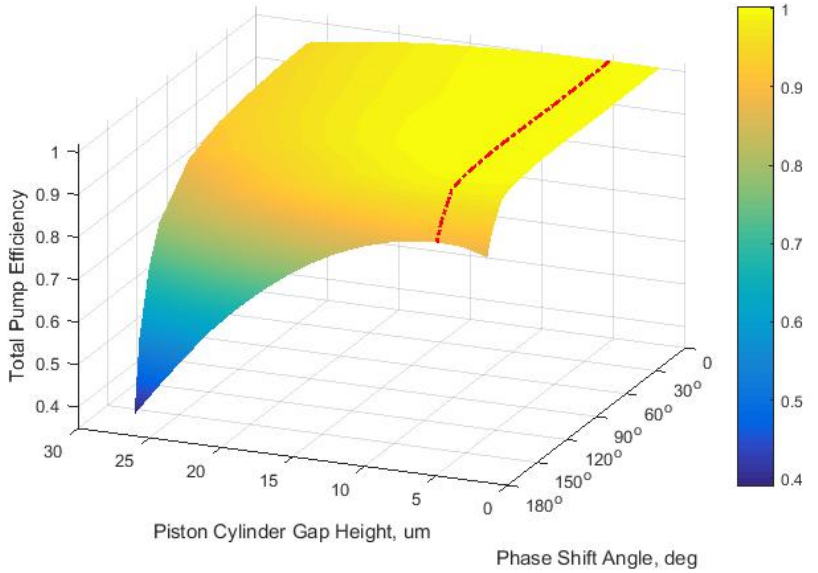

Figure 2.21: Model predicted efficiency v.s. phase shift angle and piston cylinder gap height.

frequency conditions. Generally, it can be seen that the AF hydraulic pump prefers a short and large connecting pipe to minimize the energy loss associated with hydraulic pipe resistance. Once the diameter of the connecting pipe reaches at approximately 4*mm*, for the first generation prototype, the overall pump efficiency remains high across most of the

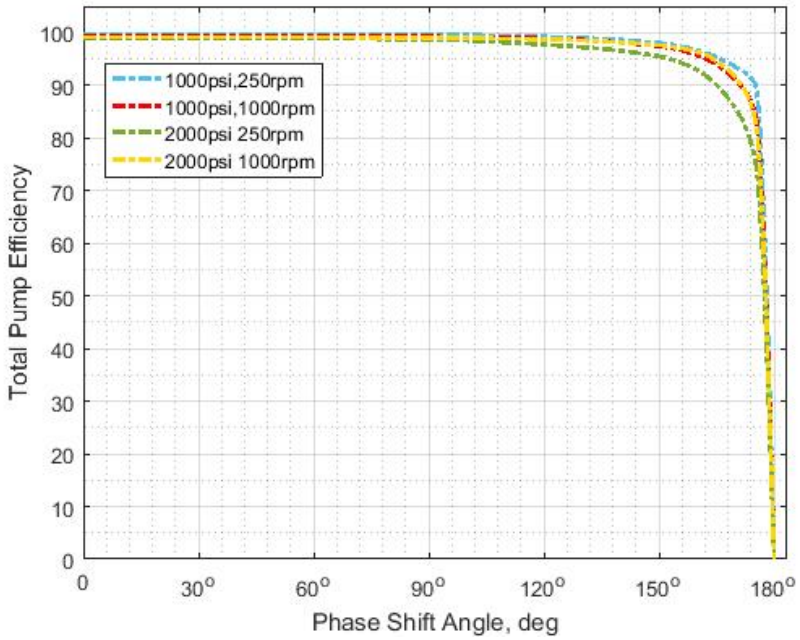

Figure 2.22: Model predicted efficiency v.s. phase shift angles.

phase shift angles. The AF pump favors a short connecting pipe to 1) reduce the associated energy loss and 2) avoid complicated phenomena brought by long hydraulic pipes such as reflected pressure waves.

The predicted pump efficiency curve against various phase shift angles and piston cylinder gap heights varying between $1\mu m$ and $28\mu m$ under the same operating conditions, is shown in Fig. 2.21. It shows that the optimal piston cylinder gap height (red dash line) is independent of the different phase shift angle ϕ. This results shows agreement with minimum energy dissipation analysis [21] and with the closed form model developed by the authors [22]. Unlike the connecting pipe, due to the manufacture accuracy, the piston cylinder gap height cannot be made too small.

With all mechanical losses of the AF pump mechanism taken out of design consideration, a series of simulations were run with various operating conditions and displacements. The load pressure varied between $6.895MPa$ ($1000psi$) to $13.789MPa$ ($2000psi$) and the input shaft speed were between $4.167Hz$ ($250rpm$) to $16.667Hz$ ($1000rpm$). The phase

shift angles varied between 0 and 175 degrees and is shown in Fig. 2.22.

2.9 Conclusion

This paper presents the basic principles and advantages of a novel alternating flow (AF) hydraulic pump. A dynamic model describing the cylinder pressure, the flow between a pair of cylinders, and the inlet and output flow as a function of phase shift angle is developed in detail. The hydraulic check valve dynamics and the effective bulk modulus are taken into consideration. A first generation prototype was built with two inline triplex Cat Pump®pumps to demonstrate the concept. Experiments were run and data was collected to validate the model. With the model validated, it can be used to explore the parameter space and optimize future prototype designs. Taking four types of energy losses into consideration, the model results show that the novel AF hydraulic pump is able to achieve high efficiencies of greater than 90% for displacements greater than 10% (approximately 168 degrees).

2.10 Acknowledgement

This project is sponsored by the Center for Compact and Efficient Fluid Power (CCEFP) under NSF grant #0540834 with funding from the National Fluid Power Association (NFPA) Education and Technology Foundation. We also thank Cat Pump for donating the experimental prototype.

2.11 References

[1] Lonnie J Love. Estimating the impact (energy, emissions and economics) of the us fluid power industry. Technical report, Oak Ridge National Laboratory (ORNL), 2012.

[2] Kim Heybroek. Saving energy in construction machinery using displacement control hydraulics: Concept realization and validation. PhD thesis, Link¨oping University Electronic Press, 2008.

[3] Christopher Williamson. Efficiency study of an excavator hydraulic system based on displacement-controlled actuators. In Proceedings of the Bath/ASME Symposium on Fluid Power and Motion Control (FPMC), 2008, pages 291–307, 2008.

[4] Monika Ivantysynova. Innovations in pump design-what are future directions? In Proceedings of the JFPS International Symposium on Fluid Power, volume 2008, pages 59–64. The Japan Fluid Power System Society, 2008.

[5] Chao Zhang, Shaokang Huang, Jun Du, Xingjian Wang, Shaoping Wang, and Haiyan Zhang. A new dynamic seven-stage model for thickness prediction of the film between valve plate and cylinder block in axial piston pumps. Advances in Mechanical Engineering, 8(9):1687814016671446, 2016.

[6] Lizhi Shang and Monika Ivantysynova. A temperature adaptive piston design for swash plate type axial piston machines. International Journal of Fluid Power, 18(1):38–48, 2017.

[7] G Rizzo, GP Massarotti, A Bonanno, R Paoluzzi, M Raimondo, M Blosi, F Veronesi, A Caldarelli, and G Guarini. Axial piston pumps slippers with nanocoated surfaces to reduce friction. International Journal of Fluid Power, 16(1):1–10, 2015.

[8] Shawn R Wilhelm and James D Van de Ven. Synthesis of a variable displacement linkage for a hydraulic transformer. In ASME 2011 International Design Engineering Technical Conferences and Computers and Information in Engineering Conference, pages 309–316. American Society of Mechanical Engineers, 2011.

[9] Shawn Wilhelm and James Van de Ven. Adjustable linkage pump: efficiency modeling and experimental validation. Journal of Mechanisms and Robotics, 7(3):031013, 2015.

[10] SR Wilhelm and James D Van de Ven. Design of a variable displacement triplex pump. International Fluid Power ExpositionLas Vegas, NV, 2014.

[11] Md Ehsan, WHS Rampen, and SH Salter. Modeling of digital-displacement pump-motors and their application as hydraulic drives for nonuniform loads. Journal of dynamic systems, measurement, and control, 122(1):210–215, 2000.

[12] Matti Linjama. Digital fluid power: State of the art. In 12th Scandinavian International Conference on Fluid Power, Tampere, Finland, May, pages 18–20, 2011.

[13] George Constantinesco. Theory of Wave Transmission: A Treatise on Transmission of Power by Vibrations, volume 1. Walter Haddon, Proprietor of Patents Controlling Wave Transmission, 1922.

[14] Cheng-Kuo Weng. Transmission of fluid power by pulsating-flow (pf) concept in hydraulic systems. Journal of Basic Engineering, 88(2):316–321, 1966.

[15] Durham C Davis. On Alternating Flow Hydraulic Systems. PhD thesis, Monash University, 1982.

[16] Ioan-Lucian Marcu. A new concept of rotary hydraulic motor working with alternating flows. In Proc. of the 6th International Conference on Hydraulic Machinery and Hydrodynamics-HMH2004 in Trans. of Mechanics, Tom 49 (63), pages 361–362, 2004.

[17] Hossein Gholizadeh, Richard Burton, and Greg Schoenau. Fluid bulk modulus: comparison of low pressure models. International journal of fluid power, 13(1):7–16, 2012.

[18] Anthony L Knutson and James D Van de Ven. Modelling and experimental validation of the displacement of a check valve in a hydraulic piston pump. International Journal of Fluid Power, 17(2):114–124, 2016.

[19] Duqiang Wu, Richard Burton, and Greg Schoenau. An empirical discharge coefficient model for orifice flow. International journal of fluid power, 3(3):13–19, 2002.

[20] John S Cundiff. Fluid power circuits and controls: fundamentals and applications. CRC Press, 2001.

[21] Jaroslav Ivantysyn and Monika Ivantysynova. Hydrostatic pumps and motors: principles, design, performance, modelling, analysis, control and testing. Tech Books International, 2003.

[22] Mengtang Li, Ryan Foss, Kim A Stelson, James D Van de Ven, and Eric J Barth. A design optimization model for an alternating flow (af) hydraulic pump based on first principles. In ASME 2017 Dynamic Systems and Control Conference, pages V003T27A007–V003T27A007. American Society of Mechanical Engineers, 2017.

Chapter 3

Bond Graph Modeling of Mechanical Circulatory Support (MCS) Device - Cardiovascular System Interactions

Mengtang Li[1], Marvin Slepian[2], Eric Barth[1]

1. Vanderbilt University, Nashville, TN

2. University of Arizona, Tucson, AZ

From: *ASME Journal of Biomechanical Engineering*

Status: Accepted December, 2019

3.1 Abstract

Though mechanical circulatory support (MCS) devices, such as ventricular assist devices (VAD) and total artificial hearts (TAH), provide heart failure patients with bridges to heart transplantation or are alternatives to transplantation, device performance and corresponding control strategies are often difficult to evaluate. Difficulties arise due to the complex interaction of multiple domains – i.e. biological, hydraulic, hemodynamics, electromechanical, system dynamics, and controls. In an attempt to organize, integrate and clarify these interactions, a technique often used in hydraulic pump design and robotics, called "bond graph modeling," is applied to describe the performance and functionality of MCS devices and the interaction between the cardiovascular system and the MCS device.

This technical brief demonstrates the advantages of this tool in formulating a model for the systemic circulation interacting with the left side of a TAH, adopting the fundamental structure of either a hydraulic mechanism (i.e. AbioCor/Carmat) or a pneumatic mechanism (i.e. SynCardia), combined with a systemic circulation loop. The model captures the

dynamics of the membrane, the hydraulic source or pneumatic source, and the systemic circulation. This multi-disciplinary cross-pollination of an analytical tool from the field of dynamic systems may provide important insight to further aid and improve the design and control of future MCS systems.

3.2 Introduction

A "bond graph" is a graphical modeling method to describe the energy relationship within any physical dynamic system [1,2]. Although seemingly similar to a block diagram or a signal flow graph, a bond graph mainly represents bi-directional energy exchange flows, instead of uni-directional information flows. Energy ports are linked via bonds. The energy flow within each bond is denoted by a pair of power variables called "effort" and "flow," over all connected bonds is the same while the flows sum to zero, and 1-junctions, where the flow through all connected bonds is the same while the efforts sum to zero. A unified model can be derived for multi-energy-domain systems using this method. Another significant feature of a bond graph is the causality, which indicates the feasibility of mathematical relationships in the real world. One dominant power variable (e.g. voltage) eventually specifies the other one (e.g. current), with the whole system energy exchange mechanism known (e.g. impedance). The effort and flow variables form a "handshake" mechanism between dynamic elements. In this manner, bond graphs allow modeling of subsystems with a first-principles mechanism of interaction with connected subsystems. Even though the cardiovascular system and an MCS device are very different, the bond graph methodology allows us to study their multi-energy-domain interaction.

3.3 Modeling

Research has been done to develop accurate models for the human circulation, including systemic and pulmonary circulations [3-7] and on the inter-dependence between the two sides [8]. Using a bond graph representation, such models can be paired with models

of MCS devices to study their interactions [9,10]. To illustrate the bond graph technique, using a model similar to the cardiovascular system as described in [7], the interaction of the systemic circulation with one side of a TAH system is considered here. Distinct pressure locations are marked with 0-junctions and connected with cardiovascular elements through 1-junctions, as shown in Fig.3.1a and Fig.3.1b. The bond graph energy bonds (purple line with half arrow and end bar) were then obtained and marked by numbers. Due to four different modes of these two valves, three different cardiac phases, i.e. ejection phase, injection phase and isovolumetric phase, exist. Considering that only passive valves are used in currently available TAHs (Syncardia), such as the FDA approved rotating disk valve [11], the isovolumetric phase is not modeled here for the systemic circulation combined with a TAH.

3.3.1 Ejection Phase Modeling

During the ejection phase, the aortic valve is open while the mitral valve is closed. The bond graph equations Eqns.(**??**-3.17) are derived below. The left atrial pressure (LAP), arterial pressure (AP), aortic pressure (AoP), aortic flowrate and outlet flowrate from the TAH are e_{12}, e_9, e_4, f_6 and f_1 respectively.

$$f_1 = f_2 = f_3 \tag{3.1}$$

$$e_1 = e_2 + e_3 \tag{3.2}$$

$$e_2 = R_3 f_2 \tag{3.3}$$

$$e_3 = e_4 = e_5 \tag{3.4}$$

$$f_3 = f_4 + f_5 \tag{3.5}$$

$$\dot{e}_4 = (1/C_4) f_4 \tag{3.6}$$

$$f_5 = f_6 = f_7 = f_8 \tag{3.7}$$

$$e_5 = e_6 + e_7 + e_8 \tag{3.8}$$

$$\dot{f}_6 = (1/I)e_6 \tag{3.9}$$

$$e_7 = R_4 f_7 \tag{3.10}$$

$$e_8 = e_9 = e_{10} \tag{3.11}$$

$$f_8 = f_9 + f_{10} \tag{3.12}$$

$$\dot{e}_9 = (1/C_3)f_9 \tag{3.13}$$

$$f_{10} = f_{11} = f_{12} \tag{3.14}$$

$$e_{10} = e_{11} + e_{12} \tag{3.15}$$

$$e_{11} = R_1 f_{11} \tag{3.16}$$

$$\dot{e}_{12} = (1/C_2)f_{12} \tag{3.17}$$

3.3.2 Injection Phase Modeling

During the injection phase, the aortic valve is closed while the mitral valve is open. The bond graph model equations Eqns. (3.18-3.35) are derived below. The LAP, AP, AoP, aortic flowrate and inlet flowrate from TAH are e_{16}, e_{20}, e_{24}, f_{23} and f_{13} respectively.

$$f_{13} = f_{14} = f_{15} \tag{3.18}$$

$$e_{13} = f_{14} + f_{15} \tag{3.19}$$

$$e_{14} = R_2 f_{14} \tag{3.20}$$

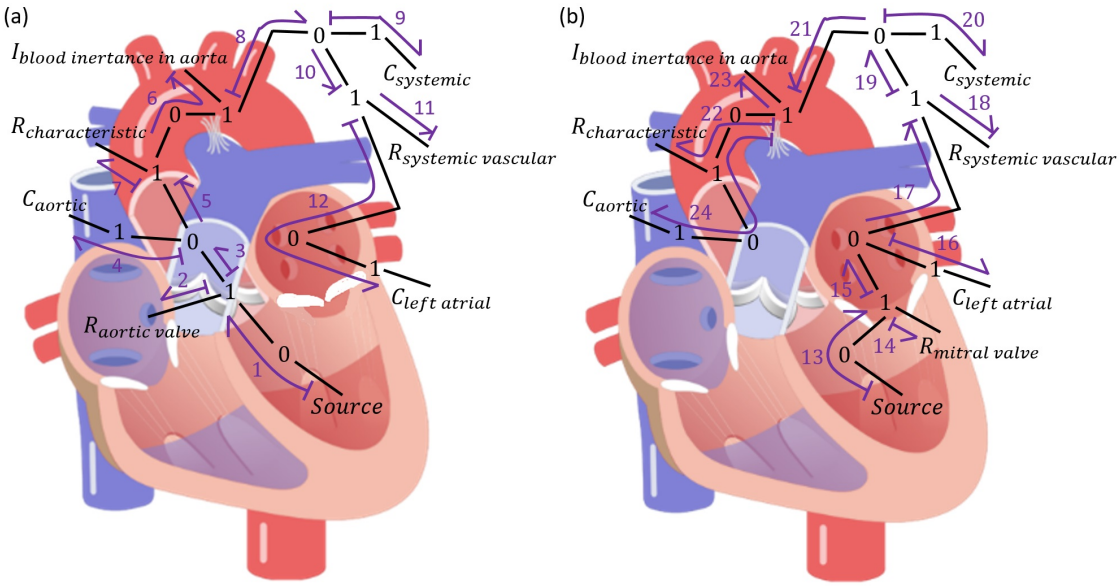

Figure 3.1: (a) Bond graph graphic modeling of ejection phase (b) Bond graph graphic modeling of injection phase.

$$e_{15} = e_{16} = e_{17} \tag{3.21}$$

$$f_{15} = f_{16} + f_{17} \tag{3.22}$$

$$\dot{e}_{16} = (1/C_2) f_{16} \tag{3.23}$$

$$f_{17} = f_{18} = f_{19} \tag{3.24}$$

$$e_{17} = e_{18} + e_{19} \tag{3.25}$$

$$e_{18} = R_1 f_{18} \tag{3.26}$$

$$e_{19} = e_{20} = e_{21} \tag{3.27}$$

$$f_{19} = f_{20} + f_{21} \tag{3.28}$$

$$f_{19} = f_{20} + f_{21} \tag{3.29}$$

$$\dot{e}_{20} = (1/C_3) f_{20} \tag{3.30}$$

$$f_{21} = f_{22} = f_{23} = f_{24} \tag{3.31}$$

$$e_{21} = e_{22} + e_{23} + e_{24} \tag{3.32}$$

$$e_{22} = R_4 f_{22} \tag{3.33}$$

$$\dot{f}_{23} = (1/I) e_{23} \tag{3.34}$$

$$\dot{e}_{24} = (1/C_4) f_{24} \tag{3.35}$$

3.3.3 Hydraulic-Based TAH Modeling

A self-contained implantable MCS device, the Carmat TAH, consists of two independent ventricles separated by membranes into compartments for blood and hydraulic oil, four tricuspid valves for uni-direction flow, internal battery and transcutaneous energy transfer coils, as shown in Fig.3.2a. Two external gear pumps are placed below the two ventricles and rotate back and forth to pump hydraulic oil to move the membranes, thus creating a pulsatile blood flow [12]. The fundamental pumping mechanism of the Carmat TAH can be modeled as a mass-spring-damper system powered by a controllable flow source, as in Fig.3.2b. The elastic membrane is considered as a solid piston while its elasticity is modeled by spring stiffness and damping. The simplified bond graph model is shown in Fig.3.2c and corresponding equations (3.36-3.47) are derived below.

$$f_{h1} = S_f \tag{3.36}$$

$$f_{h2} = D f_{h1} \tag{3.37}$$

$$e_{h1} = D e_{h2} \tag{3.38}$$

$$f_{h3} = (1/A_{mem}) f_{h2} \tag{3.39}$$

$$e_{h2} = (1/A_{mem}) e_{h3} \tag{3.40}$$

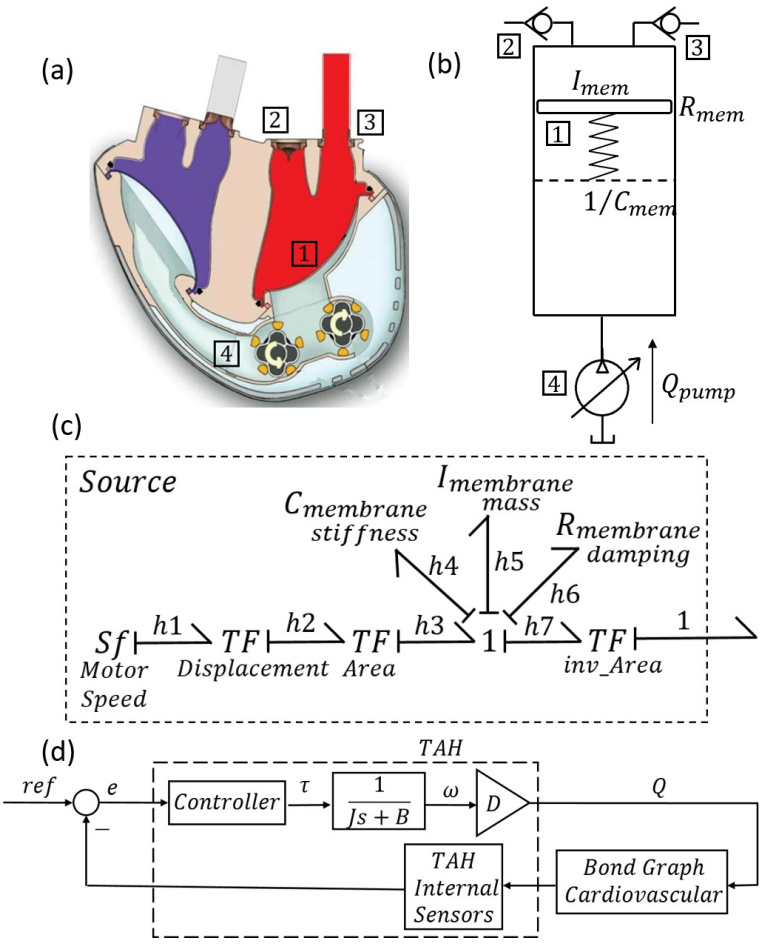

Figure 3.2: (a) Cross-sectional view of Carmat TAH: ①membrane, ②inlet valve, ③outlet valve, ④gear pumps (b) Simplified dynamic model of Carmat TAH (c) Bond graph of Carmat TAH (d) Control block diagram

$$f_{h3} = f_{h4} = f_{h5} = f_{h6} = f_{h7} \tag{3.41}$$

$$e_{h3} = e_{h4} + e_{h5} + e_{h6} + e_{h7} \tag{3.42}$$

$$\dot{e}_{h4} = (1/C_{mem}) f_{h4} \tag{3.43}$$

$$\dot{f}_{h5} = (1/I_{mem}) e_{h5} \tag{3.44}$$

$$e_{h6} = R_{mem} f_{h6} \tag{3.45}$$

$$f_1 = A_{mem} f_{h7} \tag{3.46}$$

$$e_{h7} = A_{mem} e_1 \tag{3.47}$$

With 16 unknowns but only 15 equations, the following restriction or relation can be obtained.

$$f_1 = DS_f \tag{3.48}$$

which means the flowrate of the hydraulic pump determines the flowrate of the TAH directly without the effect of the cardiovascular system. Once the driving signal, pump speed $S_f = f_{h1}$, is given, the equation set is solvable and the interaction between the TAH and the circulation system can be simulated and analyzed.

3.3.4 Pneumatic Based TAH Modeling

As the only FDA approved TAH for use as a bridge to transplantation (2004) and for long-term (destination) implantation (2012), the SynCardia heart, shown in Fig.3.3a, is composed of two independent polyurethane ventricles with 70 mL volume, four mechanical valves for uni-directional flow control, and two percutaneous pneumatic tubes for connecting to the external console. Blood inflow and ejection motion is realized by the membranes which are controlled by a pneumatic pressure differential across the membranes. The dynamic mechanism of the membrane can be modeled as a mass-spring-damper system powered by a controllable pressure source, as in Fig.3.3b. The semi-elastic membrane is considered as a solid piston while its elasticity is modeled by spring stiffness and damping. The simplified bond graph model is shown in Fig.3.3c. As mathematically proven in Eqn.(3.48) previously, the TAH flowrate equals that of the source. While for the hydraulic based TAH, such as the Carmat or AbioCor, the source flow is known (specified by the controlled motor speed), for the pneumatic based TAH, such as SynCardia, the flow from the source is unknown and it depends on the interaction with the rest of the cardiovascular system (pressure is the specified effort source).

The dynamic model of the pneumatic power mass-spring-damper system is described

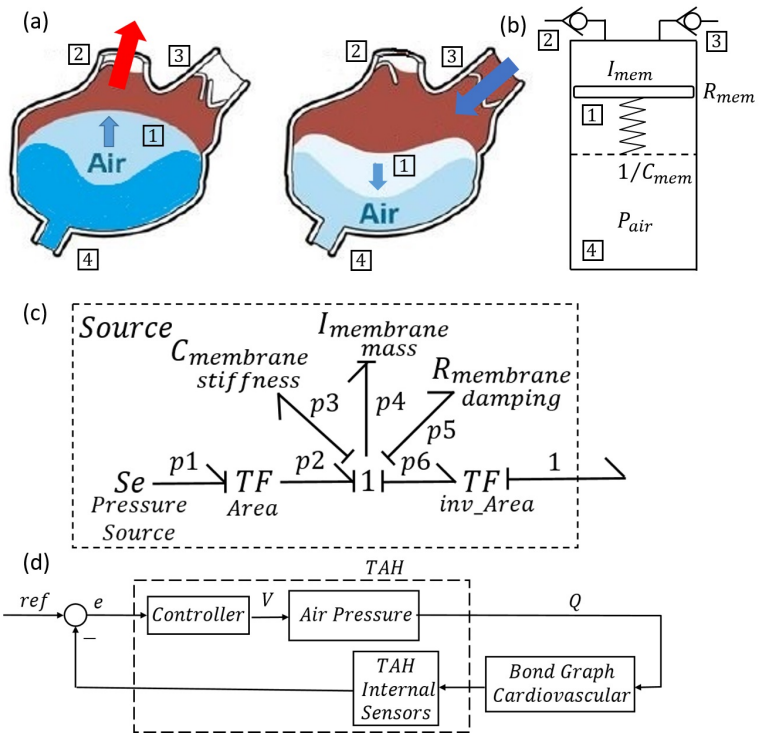

Figure 3.3: (a) Cross view of SynCardia TAH: ①membrane, ②outlet valve, ③inlet valve, ④ external pressure source (b) Simplified dynamic model of SynCardia TAH (c) Bond graph model of SynCardia TAH (d) Control block diagram

as follows

$$f_1 = f_{p1} \tag{3.49}$$

$$I_{mem}\ddot{f}_{p2} = A_{mem}(e_{p1} - e_1) - R_{mem}\dot{f}_{p2} - C_{mem}f_{p2} \tag{3.50}$$

$$f_1 = Af_{p2} \tag{3.51}$$

$$e_1 = \begin{cases} AoP + R_3 f_1 & \text{, if } f_1 > 0 \\ LAP + R_2 f_1 & \text{, if } f_1 < 0 \end{cases} \tag{3.52}$$

Once the driving signal, air pressure $S_e = e_{p1}$, is given, the equation set is solvable and the interaction between the TAH and the circulation system can be simulated and analyzed.

3.4 Results

Various methods and tools exist to solve the bond graph model. Our results demonstrate that the model can be utilized to investigate the effects of either varying CV conditions encoded by the model's parameters (e.g. afterload) or altering mechanical properties of the TAH (e.g. damping, moment of inertia of the pump rotor, or stiffness of the pneumatic membrane). Such investigation is useful in evaluating a particular design and thereby guide and improve any model-guided design iteration. The hydraulic and pneumatic based TAHs are controlled to track a cardiac output and flowrate emulating a human heart [13], with the associated control block diagram shown in Fig.3.2d and Fig.3.3d respectively.

Bond graph model parameters for the systemic circulation [14] and hydraulic and pneumatic based TAHs are listed in Tab.3.1. To ensure the correctness and consistency of the modeling from the energy point of view, SI units are used and then converted into medical standard units.

3.4.1 Hydraulic Based TAH + Circulation

The hemodynamics of the hydraulic based TAH circulation system under four different afterload operating conditions are shown in Fig.3.4. As the afterload increases, higher LVP is required to open aortic valve to eject blood into aorta. The delayed valve open time and decreased blood pumping effects are also noticeable from Fig.3.4a and 3.4b. Note that compared with the native heart, the blood pumping chamber of this hydraulic based TAH is smaller (to fit the entire device in a patient's chest), which leads the end systolic pressure volume relationship (ESPVR) in Fig.3.4c intersects with horizontal axis at a different location.

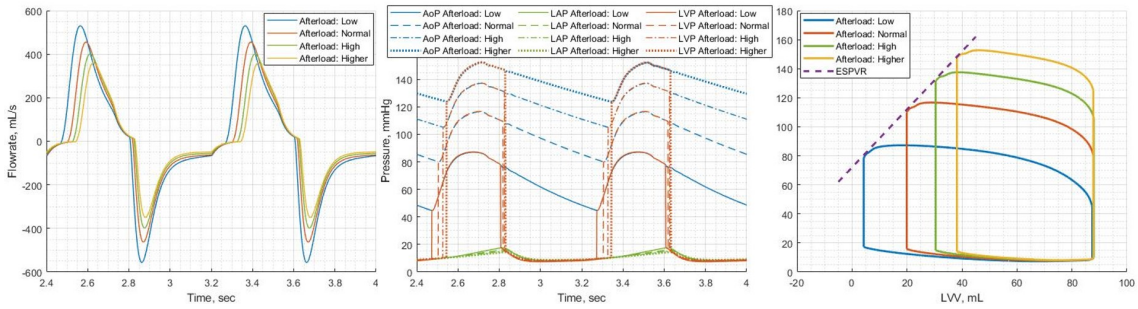

Figure 3.4: (a) Flowrate vs time (b) Pressure vs time (c) PV-loops of the hydraulic based TAH with different afterload

3.4.2 Pneumatic Based TAH + Circulation

Unlike the hydraulic-based TAH, the control strategy for a pneumatic-based TAH is more complex. Figure 3.5 plots the hemodynamics of the pneumatic based TAH circulation system under four different afterload operating conditions. Reduced pressure required to open aortic valve, delayed valve opening time and decreased amount of pumping blood due to increased afterload pressure can be seen from Fig.3.5. Also, compared with the native heart, the blood pumping chamber of a pneumatic based TAH (e.g. 70 mL for SynCardia) is smaller in size to fit within the patient's chest. The consequence of this smaller size, at least for this control algorithm, is that it cannot comply with the ESPVR once it reaches the volume limits, as the blue PV-loop shown in Fig.3.5c.

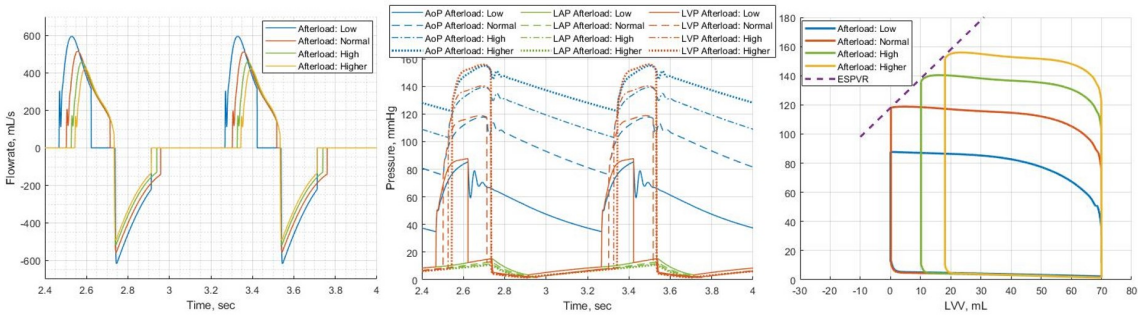

Figure 3.5: (a) Flowrate vs time (b) Pressure vs time (c) PV-loops of the pneumatic based TAH with different afterload

3.5 Conclusions

The net performance of implanted MCS devices involves the balance of interaction between the device and the overall cardiovascular system of the individual patient into whom it is implanted. Bond graph modeling provides a quantitative methodology for universally describing a complex system containing subsystems from the perspective of differing energy domains. This technical brief highlights this methodology to suggest its value, and offer it as a tool to further understand MCS-human CV system interactions, as well as to examine the behavior of parameters and variables which may be optimized to enhance device and system design. This approach adds an additional tool to the cardiovascular biomechanical engineer, physiologist and physician with potential for enhancing the safety and efficacy of MCS systems, thereby reducing adverse events and improving their clinical utility.

3.6 Limitations

Here we present only a simple bond graph model describing the interaction between the systemic circulation loop with the left side of a basic TAH. A more detailed model is needed to take into account the right (pulmonary) side of the heart and interdependence between left and right sides, isovolumetric phase, and the dynamics of heart valves. What we present is a starting point, as ultimately further model validation will be needed. Finally, we must keep in mind that the traditional bond graph technique utilizes SI units during calculation, resulting in un-common medical standard units.

3.7 Acknowledgment

We acknowledge support for the Arizona Center for Accelerated Biomedical Innovation (ACABI) of the University of Arizona.

3.8 References

[1] Henry M Paynter. Analysis and design of engineering systems. MIT press, 1961.

[2] Dean Karnopp and Ronald C Rosenberg. Analysis and simulation of multiport systems: The bond graph approach to physical system dynamics. 1968.

[3] J Bai, K Ying, and D Jaron. Cardiovascular responses to external counterpulsation: a computer simulation. Medical and Biological Engineering and Computing, 30(3):317–323, 1992.

[4] C De Lazzari, G Ferrari, R Mimmo, G Tosti, and D Ambrosi. A desk-top computer model of the circulatory system for heart assistance simulation: effect of an lvad on energetic relationships inside the left ventricle. Medical engineering & physics, 16(2):97–103, 1994.

[5] Longya Xu and Minghua Fu. Computer modeling of interactions of an electric motor, circulatory system, and rotary blood pump. ASAIO journal, 46(5):604–611, 2000.

[6] Antonio Ferreira, Shaohui Chen, Marwan A Simaan, J Robert Boston, and James F Antaki. A nonlinear state-space model of a combined cardiovascular system and a rotary pump. In Proceedings of the 44th IEEE Conference on Decision and Control, pages 897–902. IEEE, 2005.

[7] Marwan A Simaan, Antonio Ferreira, Shaohi Chen, James F Antaki, and David G Galati. A dynamical state space representation and performance analysis of a feedback-controlled rotary left ventricular assist device. IEEE Transactions on Control Systems Technology, 17(1):15–28, 2008.

[8] William P Santamore and Daniel Burkhoff. Hemodynamic consequences of ventricular interaction as assessed by model analysis. American Journal of Physiology-Heart and Circulatory Physiology, 260(1):H146–H157, 1991.

[9] GK Klute, U Tasch, and DB Geselowitz. An optimal controller for an electric ventricular-assist device: Theory, implementation, and testing. IEEE transactions on biomedical engineering, 39(4):394–403, 1992.

[10] U Tsach, DB Geselowitz, Alok Sinha, and HK Hsu. A novel output feedback pusher plate controller for the penn state electric ventricular assist device. Journal of dynamic systems, measurement, and control, 111(1):69–74, 1989.

[11] Marvin J Slepian, Yared Alemu, Jo˜ao Silva Soares, Richard G Smith, Shmuel Einav, and Danny Bluestein. The syncardia total artificial heart: in vivo, in vitro, and computational modeling studies. Journal of biomechanics, 46(2):266–275, 2013.

[12] Paul Mohacsi and Pascal Leprince. The carmat total artificial heart, 2014.

[13] Jan-Willem Lankhaar, Fleur A R¨ovekamp, Paul Steendijk, Theo JC Faes, Berend E Westerhof, Taco Kind, Anton Vonk-Noordegraaf, and Nico Westerhof. Modeling the instantaneous pressure–volume relation of the left ventricle: a comparison of six models. Annals of biomedical engineering, 37(9):1710–1726, 2009.

[14] Yih-Choung Yu, J Robert Boston, Marwan A Simaan, and James F Antaki. Estimation of systemic vascular bed parameters for artificial heart control. IEEE Transactions on Automatic Control, 43(6):765–778, 1998.

Table 3.1: Bond graph model parameters

Symbo	Description	Value
Systemic Circulation		
$R1$	Systemic vascular resistance	$0.6667 - 2.6667 \times 10^{-4}[kPa.sec/mm^3]$
$R2$	TAH inlet valve resistance	$6.6661 \times 10^{-7}[kPa.sec/mm^3]$
$R3$	TAH outlet valve resistance	$1.3332 \times 10^{-7}[kPa.sec/mm^3]$
$R4$	Characteristic resistance	$5.3062 \times 10^{-6}[kPa.sec/mm^3]$
$C2$	Left atrial compliance	$3.3003 \times 10^{4}[mm^3/kPa]$
$C3$	Systemic compliance	$9.9758 \times 10^{3}[mm^3/kPa]$
$C4$	Aortic compliance	$6.0005 \times 10^{3}[mm^3/kPa]$
I	Inertance of blood in Aorta	$6.6661 \times 10^{2}[kPa.sec^2/mm^3]$
HR	Heart beat frequency	$75[bpm]$
Hydraulic Based TAH		
A_{mem}	Effective surface area of membrane	$2.83 \times 10^{-3}[m^2]$
C_{mem}	Reciprocal of membrane spring stiffness	$10^{-2} - 10^{-1}$
I_{mem}	Membrane mass	$5 \times 10^{-2}[kg]$
R_{mem}	Membrane damping	$1 - 10[mN.sec/mm]$
B	Rotary damping of Motor+Pump	$50 - 500 \times 10^{-7}[kg.m^2/sec]$
D	Gear Pump Displacement	$50 \times 10^{3}[mm^3]$
J	Moment of Inertia of Motor+Pump	$50 - 200 \times 10^{-7}[kg.m^2]$
Pneumatic Based TAH		
A_{mem}	Membrane surface area	$2.8274 \times 10^{3}[mm^2]$
I_{mem}	Membrane mass	$5 \times 10^{-2}[kg]$
C_{mem}	Membrane spring stiffness	$10 - 100[mN/mm]$
R_{mem}	Membrane damping	$1 - 10[mN.sec/mm]$
V_{max}	Total chamber volume	$70 \times 10^{3}[mm^3]$

Table 3.2: Hemodynamic parameters for the hydraulic based TAH with different afterload

Afterload $[mmHg.sec/mL]$	SV$[mL]$	CO$[LPM]$	AoP$[mmHg]$ $sys/dia/mean$	LAP$[mmHg]$ $max/min/mean$
0.5	83.82	6.2867	87.07/44.58/67.21	17.63/7.99/11.08
1.0	68.19	5.1143	116.52/77.99/99.35	16.19/8.32/10.98
1.5	57.59	4.3193	137.24/105.16/121.92	15.31/8.54/10.88
2.0	50.01	3.7508	152.33/123.62/138.41	14.58/8.65/10.72

Table 3.3: Hemodynamic parameters for the pneumatic based TAH with different afterload

Afterload $[mmHg.sec/mL]$	SV$[mL]$	CO$[LPM]$	AoP$[mmHg]$ $sys/dia/mean$	LAP$[mmHg]$ $max/min/mean$
0.5	70	5.2500	85.31/34.87/56.07	15.36/3.51/8.84
1.0	70	5.2500	117.86/75.72/97.41	13.15/2.07/7.02
1.5	59.94	4.4955	139.40/103.03/121.78	11.75/1.91/6.42
2.0	52.03	3.9022	155.06/122.18/138.72	10.92/1.95/6.18

Chapter 4

Spherical Gerotor: Synthesis of a Novel Valveless Pulsatile Flow Spherical Total Artificial Heart

Mengtang Li, Eric Barth

Vanderbilt University, Nashville, TN

From: *Journal of Mechanics Engineering and Automation*

Status: Published June, 2018

4.1 Abstract

Though mechanical circulatory support (MCS) devices, such as ventricular assist device (VAD) and total artificial heart (TAH), indeed provide heart failure patients with an alternative to transplantation, many complications are provided at the same time due to the non-pulsatile blood flow or high blood shear induced by those MCS. A novel spherical total artificial heart (TAH) based on the concept of hydraulic gerotor pump is proposed. This spherical TAH features volumetric pumping mechanism, pulsatile flow generating and low blood shear. It consists of four time-varying chambers partitioned by two orange shape wedges and one complex curve cut disk. The disk rotates as twice fast as the wedges, while all in the same direction. The TAH sucks in and pumps out blood through four ports located at the pump peripheral. This paper presents the fundamental equations which establish the geometric shape of the TAH, develop the range of the size specs, and show the analytical model for the time-varying chamber volume.

4.2 Introduction

Heart failure has a prevalence of 1.7 in 100 persons globally [1, 2], with the number of patients expected to grow by 50% over the next 15 years [3, 4]. For end stage cases, surgical transplantation of a healthy heart from a donor requires a group of surgeries lasting several hours, a post-operative ICU stay and significant potential morbidity and discomfort. While this surgery does offer an effective way to overcome heart failure and the number of heart transplants worldwide has reached at approximately 5,000 in 2016, only twenty percent of the patient population are fortunate enough to receive heart transplant and waiting list is the life destination for a considerable number of unfortunate patients [5-9]. Though mechanical circulatory support (MCS) devices, such as ventricular assist device (VAD) and total artificial heart (TAH), indeed provide heart failure patients with a bridge to eventual heart transplantation or an alternative to transplantation [10], many complications, such as aortic insufficiency [11-13], thromboembolic complications [14, 15], gastrointestinal bleeding [16-18] and impaired renal function [19, 20], are provided at the same time due to the non-pulsatile blood flow or high blood shear induced by those MCSs [21]. Those complications can also be the consequences of mechanical heart valves (MHV) [4]. The high prevalence of heart failure and the lifelong anticoagulation needs as a consequence of current MCS implantation motivate a novel TAH design.

In Chapter 4.3, a brief review of current TAH and VAD is presented, with their pros and cons discussed. Next, the fundamental working principle of the proposed spherical gerotor based TAH pump, along with the advantages of the hydraulic gerotor pump, is presented in Chapter 4.4.1. Methods to derive the geometry shape of the spherical gerotor pump are described in details in Sections Chapter 4.4.3. Chapter 4.4.4 Chapter 4.4.5 follows and establishes an analytical model to calculate the chamber volume with respect to rotated angle. A discussion follows in Chapter 4.5. Chapter 4.6 provides concluding remarks.

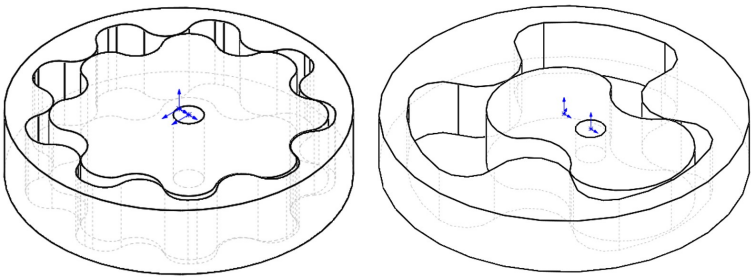

Figure 4.1: (a) A gerotor core with 8-tooth inner gear and 9-tooth outer gear; (b) a gerotor core with 2-tooth inner gear and 3-tooth outer gear.

4.3 Brief Review of Current TAH and VAD

Most of the current TAH pumps and VADs can be generally classified into (in the manner of hydraulics terms) positive displacement pump and non-positive displacement pump [22]. A positive displacement TAH pump usually consists of a reciprocating piston or a membrane driven by controlled pneumatic air (e.g. SynCardia) or hydraulic oils (e.g. Carmat) on the other side. With the aid of MHVs, those pumps are able to generate pulsatile blood flow like the real one. Yet, the usage of elastic membranes limits the durability, the overall size requires bulky space [23, 24] and the involvement of four valves increases the device thrombogenicity. Most of the current VADs and some TAHs are continuous flow pumps, which usually utilize a magnetically levitated impeller (e.g. BiVACOR, HeartMate 3). Compared with the previous type, they are more durable, much smaller, and require no valve. However, the output flow of these non-positive displacement pumps is pressure dependent [23]. And non-pulsatile blood flow induces many complications [21]. Another type of TAH is to mimic the real one [25], though even the current state of the art material does not allow a long time of massive deformation. Two recent designs are interesting and deserve more research. A rotary piston blood pump, adopting the architecture of a vehicle rotary engine, combines the benefits of membrane pump and rotary pump [26]. Another one, which is similar to our concept, is a spherical shape TAH with four chambers divided by two rotating disks [23].

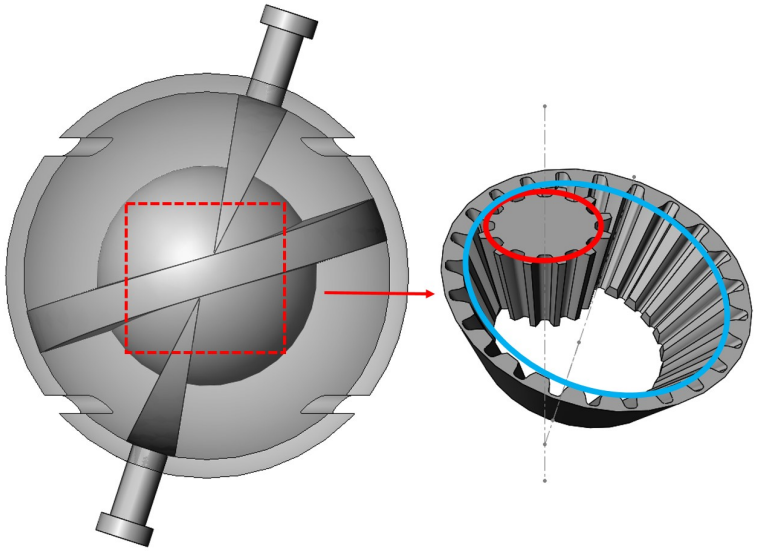

Figure 4.2: (a) A 4-chamber version of the spherical gerotor TAH; (b) the inner bevel gear set.

4.4 Method

4.4.1 Device Description

The proposed novel spherical gerotor is inspired by the hydraulic gerotor pump, which is among the most common pump architectures in fluid power systems. Compared with other rotary positive displacement pumps (e.g. external gear pump, axial impeller pump), both the inner and outer rotors of a gerotor pump rotate together, which leads to dramatically lower shear stress since the velocity gradient is much smaller. A gerotor core is shown in Fig. 4.1a with a 8-tooth inner gear and a 9-tooth outer gear, and another gerotor core with a 2-tooth inner gear and a 3-tooth outer gear is shown in Fig. 4.1b. Note that there is an eccentricity between the inner gear and outer gear. Since the inner and outer gears have different number of teeth, the rotation speeds are also different, causing the volumes of those chambers partitioned by those gear teeth vary cyclically.

The spherical gerotor TAH pump consists of four time-varying chambers partitioned by two wedges and one rotating disk. For the sake of concept illustration, the two-chamber version is presented here first. As shown in Fig. 2a, the wedge rotates along its own axial

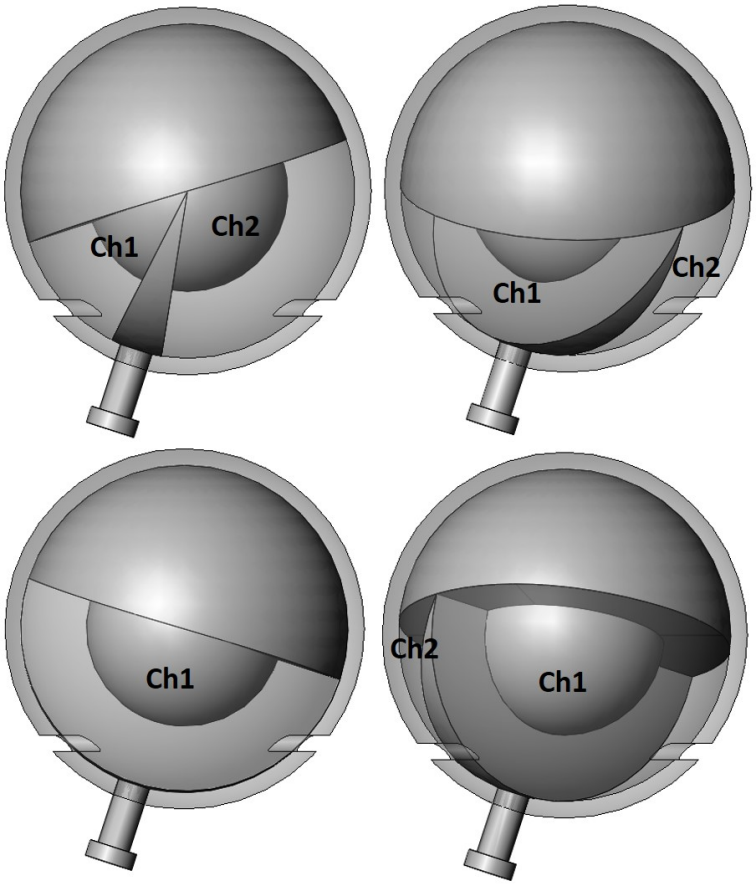

Figure 4.3: Working principle: (a) rotated angle $wt = 0rad$, (b)rotated angle $wt = \pi/4rad$, (c) rotated angle $wt = \pi/2rad$, (d) rotated angle $wt = 3\pi/2rad$.

axis through the center of the sphere and the semi-sphere part rotates along a virtual vertical axis with twice the speed of the wedge, which is realized through a costumed designed bevel gear set with 1:2 gear ratio as shown in Fig. 4.2b. The overall system has only 1 degree of freedom now and rotation of the wedge entrains the rotation of the semi-sphere, causing the volumes of the two chambers vary cyclically. The device working principle is further illustrated in Fig. 4.3. Two chambers are partitioned by the wedge, namely $Ch1$ and $Ch2$. At the beginning, $Ch1$ reaches the minimum volume and $Ch2$ reaches the maximum volume. As the wedge is rotating with respect to its own axial axis through the center of the sphere in the right-hand direction, the volume of $Ch1$ is increasing while that of $Ch2$ is decreasing. When the rotated angle equals to π, $Ch1$ reaches the maximum and the $Ch2$

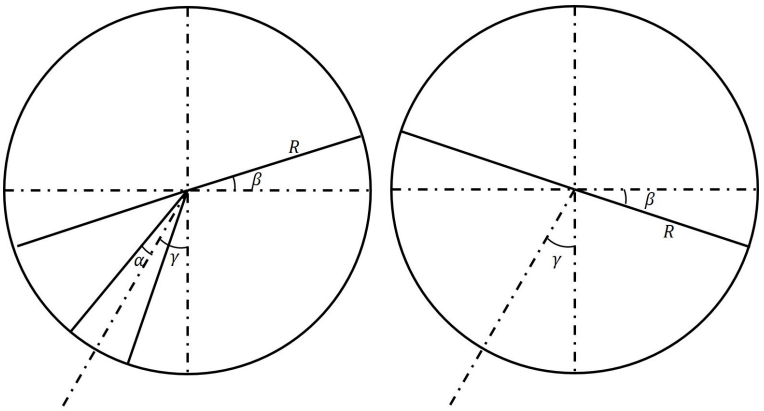

Figure 4.4: Working principle: (a) front view at rotated angle $wt = 0rad$. (b) front view at rotated angle $wt = \pi/2rad$.

reaches the minimum. After π as the rotation continued, the volume of $Ch1$ is decreasing while that of $Ch2$ is increasing. A complete cycle is finished once the wedge rotates 2π and the semi-sphere rotates 4π.

4.4.2 Shape Design

The most significant part of the novel spherical gerotor design is the geometry of the seemingly semi-sphere which allows the sliding contact between the wedge and the semi-sphere. As it will be shown here through the kinematic equations, the seemingly semi-sphere has a complex shape and it is little different between the 2-chamber version and the 4-chamber version.

4.4.3 2-Chamber Version

Simple angle constraints are considered first before deriving the actual kinematic equations of the wedge. Intuitively, since the $1:2$ gear ratio, when the wedge rotates $wt = \pi/2rad$, the semi-sphere rotates $2wt = \pi rad$. Figure 4.4a shows a front view for the spherical gerotor at $wt = 0rad$ and Fig. 4.4b shows the front view at $wt = pi/2rad$. The angle

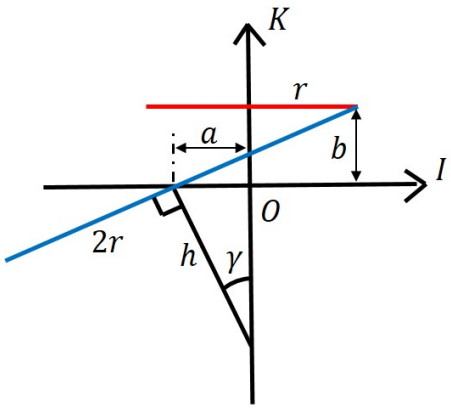

Figure 4.5: Front view of the planetary gear set.

constraints are then

$$\alpha < \beta = \gamma \tag{4.1}$$

To derive the kinematic equations of the two tips of the wedge and therefore the geometry of the semi-sphere, the bevel gear set of Fig. 4.2b is treated as a planetary gear set shown in Fig. 4.5. The pinion gear (red in Fig. 4.2b and Fig. 4.5) is fixed as the sun and the bevel gear (blue in Fig. 4.2b and Fig. 4.5) is rotating as the planet. The following geometry relationships exist:

$$h = r\frac{2\cos\gamma - 1}{\sin\gamma} \tag{4.2}$$

$$a = h\sin\gamma = r\frac{2\cos\gamma - 1}{\sin\gamma} \tag{4.3}$$

$$b = 2r\sin\gamma \tag{4.4}$$

Three frames are introduced to ease the kinematic equation derivation, shown in Fig. 4.6. The first inertial frame, IJK, is fixed at the origin O. The center of the second one, a local frame ijk, is rotating on the IJ-plane at a speed of $2w$ with a radius of a. Its i-axis and j-axis lie in the bevel gear plane and its k-axis perpendicular to the bevel gear. In order for the two gears to rotate correctly, meaning no slip between the red and blue cycles in Fig. 4.2b, the third frame, another local frame xyz, is rotating with a speed of $-w$. Its z-axis

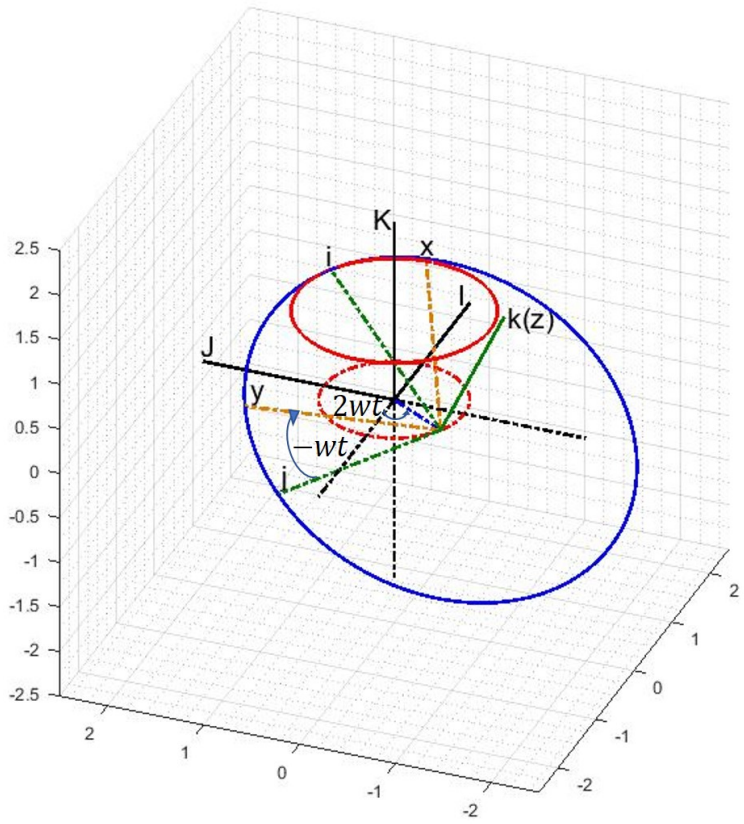

Figure 4.6: Transformation matrices.

coincides with the k-axis. The transformation matrices bellow allow the conversion of the local coordinates xyz to global inertial coordinates IJK. For the sake of space, $c()$ and $s()$ represent $cos()$ and $sin()$ respectively.

$$R_1 \begin{bmatrix} \bar{i} \\ \bar{j} \\ \bar{k} \end{bmatrix} = \begin{bmatrix} c\beta c(2wt) & -s(2wt) & -s\beta c(2wt) \\ c\beta s(2wt) & c(2wt) & -s\beta s(2wt) \\ s\beta & 0 & c\beta \end{bmatrix} \begin{bmatrix} \bar{i} \\ \bar{j} \\ \bar{k} \end{bmatrix} = \begin{bmatrix} \bar{I} \\ \bar{J} \\ \bar{K} \end{bmatrix} \tag{4.5}$$

$$R_2 \begin{bmatrix} \bar{x} \\ \bar{y} \\ \bar{z} \end{bmatrix} = \begin{bmatrix} c(-wt) & -s(-wt) & 0 \\ s(-wt) & c(-wt) & 0 \\ 0 & 0 & 1 \end{bmatrix} \begin{bmatrix} \bar{x} \\ \bar{y} \\ \bar{z} \end{bmatrix} = \begin{bmatrix} \bar{i} \\ \bar{j} \\ \bar{k} \end{bmatrix} \tag{4.6}$$

$$R_3 \begin{bmatrix} \bar{x} \\ \bar{y} \\ \bar{z} \end{bmatrix} = R_1 R_2 \begin{bmatrix} \bar{x} \\ \bar{y} \\ \bar{z} \end{bmatrix} = \begin{bmatrix} \bar{I} \\ \bar{J} \\ \bar{K} \end{bmatrix} \tag{4.7}$$

The distance between the global origin and the center of bevel gear is

$$\bar{\boldsymbol{R}} = -h\sin\beta\cos(2wt)\bar{I} - \sin\beta\sin(2wt)\bar{J} + 0\bar{K} \tag{4.8}$$

The local coordinates for the two tips on the wedge are simply two points on a circle

$$\bar{\boldsymbol{\rho}}_1 = \begin{bmatrix} 2r\cos(\frac{\pi}{2}) \\ 2r\sin(\frac{\pi}{2}) \\ 0 \end{bmatrix}^T \begin{bmatrix} \bar{x} \\ \bar{y} \\ \bar{z} \end{bmatrix} = \begin{bmatrix} 2r\cos(\frac{\pi}{2}) \\ 2r\sin(\frac{\pi}{2}) \\ 0 \end{bmatrix}^T R_3^{-1} \begin{bmatrix} \bar{I} \\ \bar{J} \\ \bar{K} \end{bmatrix} \tag{4.9}$$

$$\bar{\boldsymbol{\rho}}_2 = \begin{bmatrix} 2r\cos(\frac{3\pi}{2}) \\ 2r\sin(\frac{3\pi}{2}) \\ 0 \end{bmatrix}^T \begin{bmatrix} \bar{x} \\ \bar{y} \\ \bar{z} \end{bmatrix} = \begin{bmatrix} 2r\cos(\frac{3\pi}{2}) \\ 2r\sin(\frac{3\pi}{2}) \\ 0 \end{bmatrix}^T R_3^{-1} \begin{bmatrix} \bar{I} \\ \bar{J} \\ \bar{K} \end{bmatrix} \tag{4.10}$$

The global coordinates for the two tips on the wedge are then

$$\bar{\boldsymbol{r}}_1 = \bar{\boldsymbol{R}} + \bar{\boldsymbol{\rho}}_1 \tag{4.11}$$

$$\bar{\boldsymbol{r}}_2 = \bar{\boldsymbol{R}} + \bar{\boldsymbol{\rho}}_2 \tag{4.12}$$

Note that the transformation matrices R_1, R_2, R_3 are time varying, so $\bar{\boldsymbol{r}}_1, \bar{\boldsymbol{r}}_2$ will give the trajectories (blue dash line) of the two tips of the wedge (blue solid line), which of course are the same one, shown in Fig. 7. Remember that the gear set is treated as a planetary gear set for the sake of derivation easiness. To get the actual trajectory, both of the gears should rotate which means the center of the wedge should be moved to the global origin

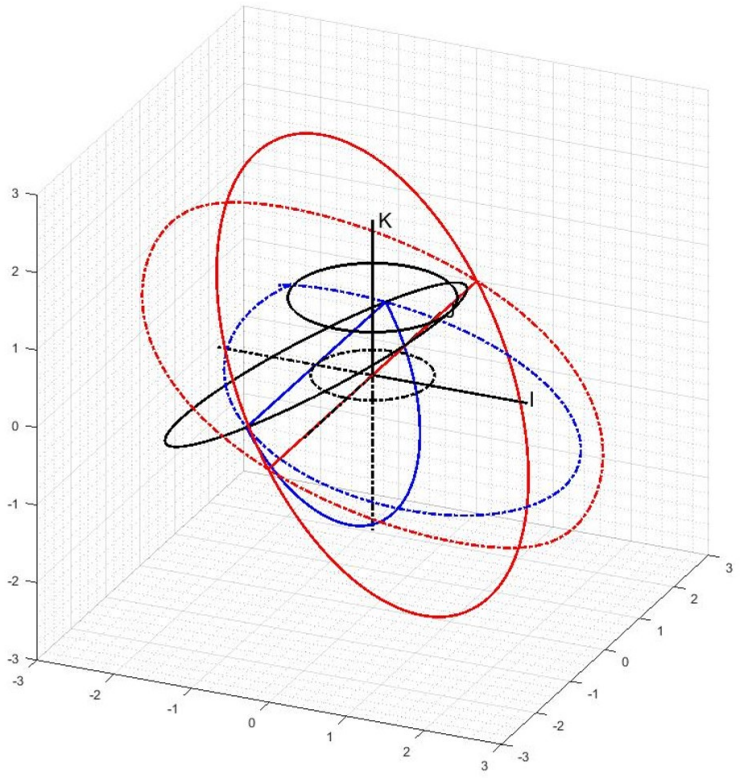

Figure 4.7: Trajectories for the two tips on the wedge.

and the radius of the spherical gerotor R, instead of the gear $2r$, should be used here. The local coordinates of the two tips on the wedge are:

$$\bar{\rho}_1' = \begin{bmatrix} R\cos(\frac{\pi}{2}) \\ R\sin(\frac{\pi}{2}) \\ -h \end{bmatrix}^T \begin{bmatrix} \bar{x} \\ \bar{y} \\ \bar{z} \end{bmatrix} = \begin{bmatrix} R\cos(\frac{\pi}{2}) \\ R\sin(\frac{\pi}{2}) \\ -h \end{bmatrix}^T R_3^{-1} \begin{bmatrix} \bar{I} \\ \bar{J} \\ \bar{K} \end{bmatrix} \tag{4.13}$$

$$\bar{\rho}_2' = \begin{bmatrix} R\cos(\frac{3\pi}{2}) \\ R\sin(\frac{3\pi}{2}) \\ -h \end{bmatrix}^T \begin{bmatrix} \bar{x} \\ \bar{y} \\ \bar{z} \end{bmatrix} = \begin{bmatrix} R\cos(\frac{3\pi}{2}) \\ R\sin(\frac{3\pi}{2}) \\ -h \end{bmatrix}^T R_3^{-1} \begin{bmatrix} \bar{I} \\ \bar{J} \\ \bar{K} \end{bmatrix} \tag{4.14}$$

The global coordinates for the two tips on the wedge are then

$$\bar{r}_1' = \bar{R} + \bar{\rho}_1' + h\cos\beta\bar{K} \tag{4.15}$$

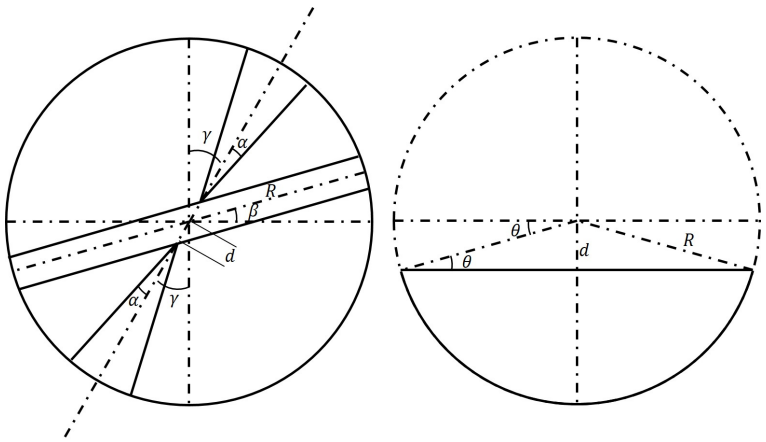

Figure 4.8: (a) Front view at rotated angle $wt = 0rad$. (b) side view of the modified wedge.

$$\bar{r}_2' = \bar{\boldsymbol{R}} + \bar{\rho}_2' + h\cos\beta\bar{K} \tag{4.16}$$

The actual trajectory of wedge of the spherical gerotor is obtained and is shown with red dash line in Fig. 4.7. A surface defined by this trajectory allows smooth contact between the wedge and the seemingly semi-sphere part.

4.4.4 4-Chamber Version

The above design can be extended a little further to contain four chambers in one single sphere. The surface defined above should be modified. Simply mirroring another wedge part to the upper side will not work because that would require an infinite thin piece to separate the upper and lower side. A front view of the 4-chamber spherical gerotor at $wt = 0rad$ is shown in Fig. 4.8a and a side view of the modified wedge is shown in Fig. 4.8b. The following geometry relationship exists

$$d = R\sin(\theta) \tag{4.17}$$

Similar to Eqns. 4.13 and 4.14, the local coordinates of the four tips on the upper

modified wedge and the two tips on the lower modified wedge respectively are:

$$\bar{\rho}_1'' = \begin{bmatrix} R\cos(\frac{\pi}{2})\cos\theta \\ R\sin(\frac{\pi}{2})\cos\theta \\ R\sin\theta - h \end{bmatrix}^T R_3^{-1} \begin{bmatrix} \bar{I} \\ \bar{J} \\ \bar{K} \end{bmatrix} \tag{4.18}$$

$$\bar{\rho}_2'' = \begin{bmatrix} R\cos(\frac{\pi}{2})\cos(\pi-\theta) \\ R\sin(\frac{\pi}{2})\cos(\pi-\theta) \\ R\sin(\pi-\theta) - h \end{bmatrix}^T R_3^{-1} \begin{bmatrix} \bar{I} \\ \bar{J} \\ \bar{K} \end{bmatrix} \tag{4.19}$$

$$\bar{\rho}_3'' = \begin{bmatrix} R\cos(\frac{\pi}{2})\cos(\pi+\theta) \\ R\sin(\frac{\pi}{2})\cos(\pi+\theta) \\ R\sin(\pi+\theta) - h \end{bmatrix}^T R_3^{-1} \begin{bmatrix} \bar{I} \\ \bar{J} \\ \bar{K} \end{bmatrix} \tag{4.20}$$

$$\bar{\rho}_4'' = \begin{bmatrix} R\cos(\frac{\pi}{2})\cos(2\pi-\theta) \\ R\sin(\frac{\pi}{2})\cos(2\pi-\theta) \\ R\sin(2\pi-\theta) - h \end{bmatrix}^T R_3^{-1} \begin{bmatrix} \bar{I} \\ \bar{J} \\ \bar{K} \end{bmatrix} \tag{4.21}$$

The global coordinates of the four tips are then respectively

$$\bar{r}_1'' = \bar{R} + \bar{\rho}_1'' + h\cos\beta\bar{K} \tag{4.22}$$

$$\bar{r}_2'' = \bar{R} + \bar{\rho}_2'' + h\cos\beta\bar{K} \tag{4.23}$$

$$\bar{r}_3'' = \bar{R} + \bar{\rho}_3'' + h\cos\beta\bar{K} \tag{4.24}$$

$$\bar{r}_4'' = \bar{R} + \bar{\rho}_4'' + h\cos\beta\bar{K} \tag{4.25}$$

The actual trajectories of the two wedges of the 4-chamber spherical gerotor are obtained and are shown with red dash line in Fig. 4.9. Two surfaces defined by these tra-

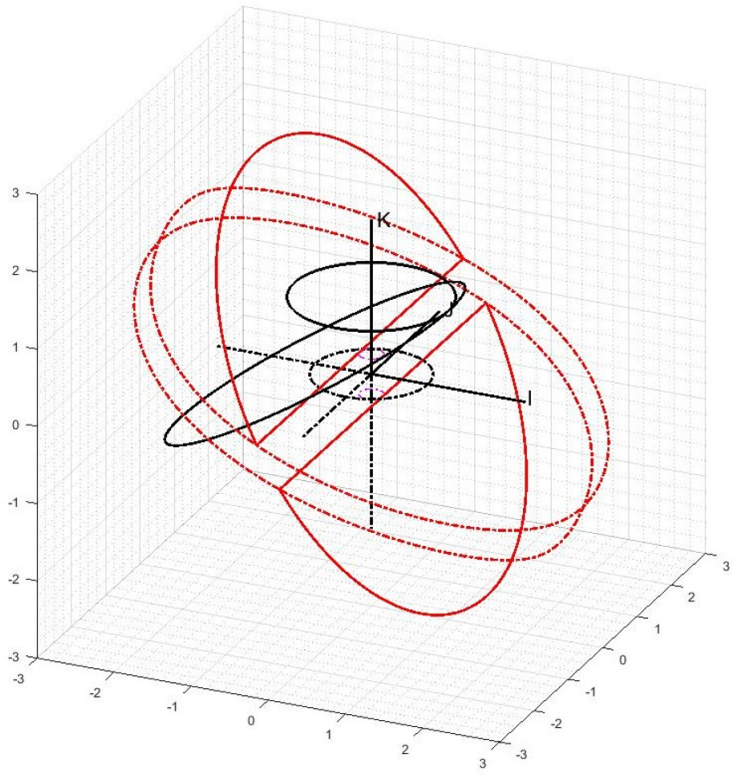

Figure 4.9: Trajectories of the four tips on the modified wedge.

jectories allow smooth contact between the upper and lower wedges and the middle disk part.

4.4.5 Time-Varying Volume

As the working principle of this novel spherical gerotor TAH is only brief introduced in section II, an analytical model for the time-varying volume of each chamber is developed in this section to better describe the pump behavior, shown in Fig. 4.10. The complex surface mathematically defined above is treated as an infinite thin circular surface to derive the chamber volume. The assumption is solid once the wedge modified distance d is small and tilt angle γ is not too big. Noting that the volume of each chamber at every position is

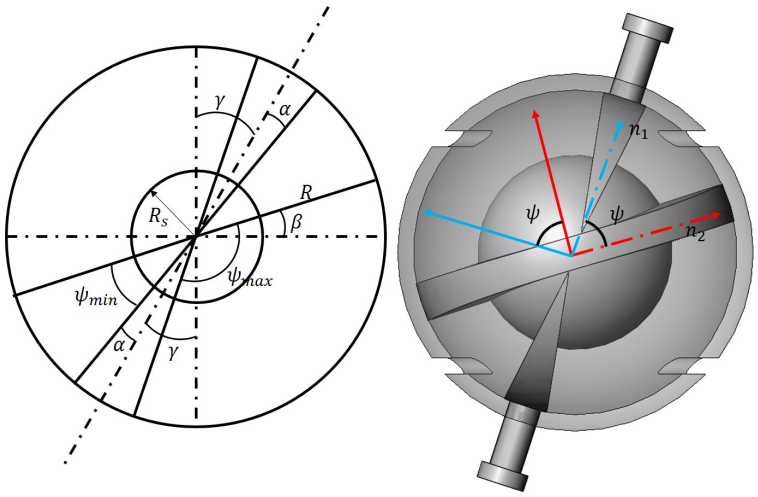

Figure 4.10: (a) Calculation of the angle between the infinite thin circular surface and the axial axis of the wedge. (b) normal directions of the infinite thin circular surface and the axial axis of the wedge.

a portion of the whole sphere, the volume can be expressed as

$$V = \frac{\psi}{2\pi}\frac{4}{3}\pi(R^3 - R_s^3) \tag{4.26}$$

where R_s is the radius of the middle sphere which contains the gear set.

To allow the TAH have the similar volume range as a real heart, the minimum volume ($Ch1$ in Fig. 4.4a) and maximum volume ($Ch2$ in Fig. 4.4a) are set to have the following relation

$$\frac{V_{min}}{V_{max}} = \frac{\frac{\psi_{min}}{2\pi}\frac{4}{3}\pi(R^3 - R_s^3)}{\frac{\psi_{max}}{2\pi}\frac{4}{3}\pi(R^3 - R_s^3)} = \frac{\frac{\pi}{2} - \alpha - \beta - \gamma}{\frac{\pi}{2} - \alpha + \beta + \gamma} = \frac{50mL}{130mL} \tag{4.27}$$

With Eqn. 4.27 solved, we obtain $0 < \alpha = \frac{\pi}{2} - \frac{9}{2}\beta < \beta$. A solution set of $(\alpha, \beta, R, R_S) = (9^o, 18^o, 50mm, 30mm)$ gives a good result of $V_{min} = 51.31mL, V_{max} = 133.41mL$, which are similar to the values of a real heart.

Since the chamber volume is a portion of a sphere, it is equivalent to calculate the angle between the ideal infinite thin circular plane and the axial axis of the wedge, which is the

same angle as the one between their normal directions, shown in Fig. 10b.

$$\bar{\boldsymbol{n}}_1 = \sin\beta\bar{I} + 0\bar{J} + \cos\beta\bar{K} \tag{4.28}$$

$$\bar{\boldsymbol{n}}_2 = \bar{\boldsymbol{R}} + \begin{bmatrix} R\cos 0 \\ R\sin 0 \\ -h \end{bmatrix}^T R_3^{-1} \begin{bmatrix} \bar{I} \\ \bar{J} \\ \bar{K} \end{bmatrix} + h\cos\beta\bar{K} \tag{4.29}$$

$$\psi = \arccos\left(\frac{\bar{\boldsymbol{n}}_1\bar{\boldsymbol{n}}_2}{|\bar{\boldsymbol{n}}_1||\bar{\boldsymbol{n}}_2|}\right) \tag{4.30}$$

So the chamber volume can be calculated with Eqns. 4.26, 4.28-4.30. The working principle of this 4-chamber version spherical gerotor is illustrated in Fig. 4.11. Figure 4.12 plots the four varying chamber volumes against the rotated angle wt, where the rotating speed w is assumed to be constant here though it does not have to be.

4.5 Discussion

Unlike those continuous flow TAHs or VADs which are non-positive displacement pumps, the proposed spherical gerotor TAH is a positive displacement pump, meaning a volumetric pump, the mean flow rate is determined by the rotating speed and the geometry displacement. If desired, good control algorithms can be applied to control the rotating speed to produce a physiological-friendly blood flow rate. Also, compared with those axial rotary TAH pumps, the blood shear stress by the proposed TAH itself is minimized theoretically by the low pump rotating speed and low speed gradient. Most of the current MHVs are pivot mechanism based and they induce thrombus formation, which requires life long anti-coagulation. The usage of obturators proposed in [27] to replace those MHVs can be applied to our proposed design to achieve valveless property.

The inherent architectures of existing pulsatile flow TAHs (e.g. SynCardia, Carmat)

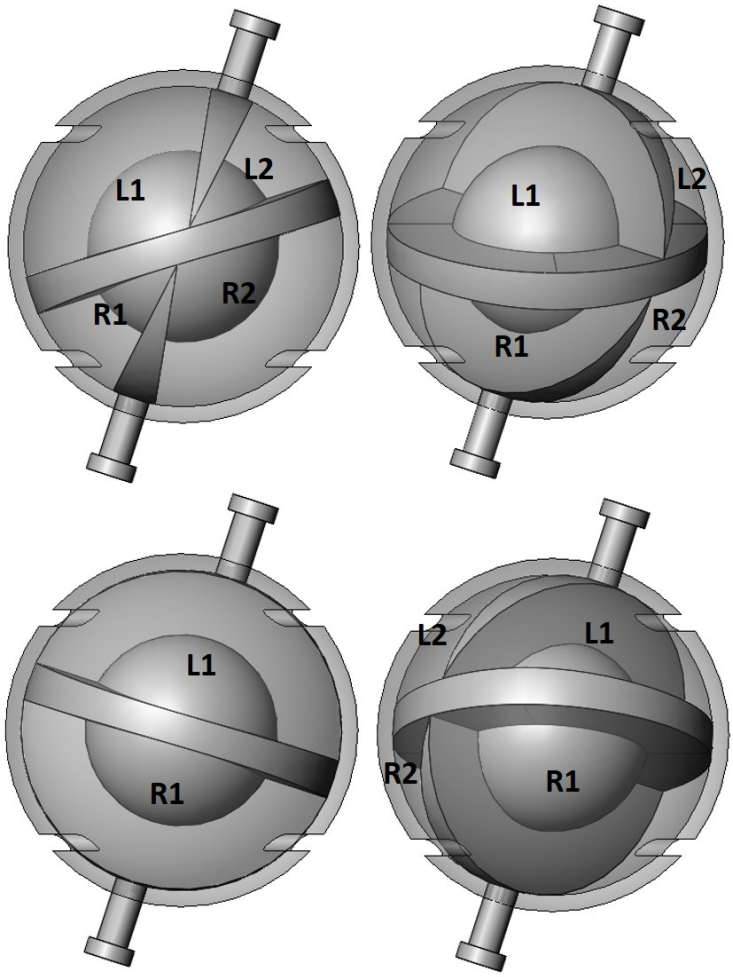

Figure 4.11: Working principle: (a) rotated angle $wt = 0rad$, (b)rotated angle $wt = \pi/4rad$, (c) rotated angle $wt = \pi/2rad$, (d) rotated angle $wt = 3\pi/2rad$.

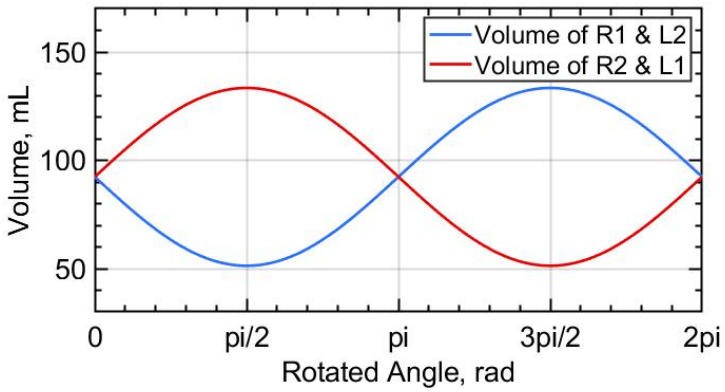

Figure 4.12: Chamber volume v.s. rotated angle wt.

pre-determine the bulky size of themselves. The proposed spherical gerotor TAH pump takes advantage of its own geometry characteristics to contain four variable chambers in one compact sphere, like the real one. Since the system degree of freedom (DoF) is reduced to one, only one servo motor, with necessary control circuits, is required to drive the whole TAH. Wireless battery recharge can also be applicable. The main drawback of this architecture, though, is that since the DoF is reduced to one, the motions of the left side and right side are coupled together, unlike the real one.

4.6 Conclusion

This paper presents the design of a novel spherical total artificial heart (TAH) based on the concept of hydraulic gerotor pump. This spherical TAH features volumetric pumping mechanism, pulsatile flow generating and low blood shear. The fundamental working principle of the proposed spherical gerotor based TAH pump is presented and methods to derive the geometry shape of the spherical gerotor pump are described in details. An analytical model to calculate the chamber volume with respect to rotated angle is presented. Future work would include but not limit to (1) built the first prototype with Plexigals®made spherical part and brass made rotating disk and wedges; (2) demonstrate proof-of-principle with regard to showing the low device thrombogenicity of proposed TAH *in silico* using Device Thrombogenicity Emulation (DTE) methodology[3, 4].

4.7 Acknowledgement

This project is sponsored by the Center for Compact and Efficient Fluid Power (CCEFP) under NSF grant #0540834 with funding from the National Fluid Power Association (NFPA) Education and Technology Foundation.

4.8 References

[1] Katharine H Fraser, Tao Zhang, M Ertan Taskin, Bartley P Griffith, and Zhongjun J Wu. A quantitative comparison of mechanical blood damage parameters in rotary ventricular assist devices: shear stress, exposure time and hemolysis index. Journal of biomechanical engineering, 134(8):081002, 2012.

[2] Donald Lloyd-Jones, Robert Adams, Mercedes Carnethon, Giovanni De Simone, T Bruce Ferguson, Katherine Flegal, Earl Ford, Karen Furie, Alan Go, Kurt Greenlund, et al. Heart disease and stroke statistics—2009 update: a report from the american heart association statistics committee and stroke statistics subcommittee. Circulation, 119(3):e21–e181, 2009.

[3] Gaurav Girdhar, Michalis Xenos, Yared Alemu, Wei-Che Chiu, Bryan E Lynch, Jolyon Jesty, Shmuel Einav, Marvin J Slepian, and Danny Bluestein. Device thrombogenicity emulation: a novel method for optimizing mechanical circulatory support device thromboresistance. PloS one, 7(3):e32463, 2012.

[4] Michalis Xenos, Gaurav Girdhar, Yared Alemu, Jolyon Jesty, Marvin Slepian, Shmuel Einav, and Danny Bluestein. Device thrombogenicity emulator (dte)- design optimization methodology for cardiovascular devices: A study in two bileaflet mhv designs. Journal of biomechanics, 43(12):2400–2409, 2010.

[5] Roger D Yusen, Leah B Edwards, Anne I Dipchand, Samuel B Goldfarb, Anna Y Kucheryavaya, Bronwyn J Levvey, Lars H Lund, Bruno Meiser, Joseph W Rossano, and Josef Stehlik. The registry of the international society for heart and lung transplantation: thirty-third adult lung and heart–lung transplant report—2016; focus theme: Primary diagnostic indications for transplant. The Journal of Heart and Lung Transplantation, 35(10):1170–1184, 2016.

[6] Dariush Mozaffarian, Emelia J Benjamin, Alan S Go, Donna K Arnett, Michael J Blaha, Mary Cushman, Sarah De Ferranti, Jean-Pierre Despr´es, Heather J Fullerton, Virginia J Howard, et al. Heart disease and stroke statistics—2015 update: a report from the american heart association. Circulation, 131(4):e29–e322, 2015.

[7] Jan D Schmitto, Daniel Zimpfer, Arnt E Fiane, Robert Larbalestier, Steven Tsui, Paul Jansz, Andre Simon, Stephan Schueler, and Martin Strueber. Long-term support of patients receiving a left ventricular assist device for advanced heart failure: a followup analysis of the registry to evaluate the heartware left ventricular assist system. European Journal of Cardio-Thoracic Surgery, 50(5):834–838, 2016.

[8] Heart Failure Society of America et al. Hfsa 2006 comprehensive heart failure practice guideline. J Card Fail, 12:e1–e2, 2006.

[9] James K Kirklin, David C Naftel, Francis D Pagani, Robert L Kormos, Lynne W Stevenson, Elizabeth D Blume, Marissa A Miller, J Timothy Baldwin, and James B

Young. Sixth intermacs annual report: a 10,000-patient database. The Journal of Heart and Lung Transplantation, 33(6):555–564, 2014.

[10] Jack G Copeland, Francisco A Arabia, Pei H Tsau, Paul E Nolan, Douglas McClellan, Richard G Smith, and Marvin J Slepian. Total artificial hearts: bridge to transplantation. Cardiology clinics, 21(1):101–113, 2003.

[11] George V Letsou, Nyma Shah, Igor D Gregoric, Timothy J Myers, Reynolds Delgado, and OH Frazier. Gastrointestinal bleeding from arteriovenous malformations in patients supported by the jarvik 2000 axial-flow left ventricular assist device. The Journal of heart and lung transplantation, 24(1):105–109, 2005.

[12] Peter M Eckman and Ranjit John. Bleeding and thrombosis in patients with continuous-flow ventricular assist devices. Circulation, 125(24):3038–3047, 2012.

[13] Sheri Crow, Dong Chen, Carmelo Milano,William Thomas, Lyle Joyce, Valentino Piacentino, Riti Sharma, Jogin Wu, Gowthami Arepally, Dawn Bowles, et al. Acquired von willebrand syndrome in continuous-flow ventricular assist device recipients. The Annals of thoracic surgery, 90(4):1263–1269, 2010.

[14] Jennifer Cowger, Francis D Pagani, Jonathan W Haft, Matthew A Romano, Keith D Aaronson, and Theodore J Kolias. The development of aortic insufficiency in left ventricular assist device-supported patientsclinical perspective. Circulation: Heart Failure, 3(6):668–674, 2010.

[15] Behzad Soleimani, Annick Haouzi, Angela Manoskey, Edward R Stephenson, Aly El-Banayosy, and Walter E Pae. Development of aortic insufficiency in patients supported with continuous flow left ventricular assist devices. ASAIO Journal, 58(4):326–329, 2012.

[16] Ashim Aggarwal, Rashmi Raghuvir, Paula Eryazici, Gregory Macaluso, Priya Sharma, Christopher Blair, Antone J Tatooles, Pat S Pappas, and Geetha Bhat. The development of aortic insufficiency in continuous-flow left ventricular assist device–supported patients. The Annals of thoracic surgery, 95(2):493–498, 2013.

[17] Kavitha Muthiah, Desiree Robson, Peter S Macdonald, AnneMKeogh, Eugene Kotlyar, Emily Granger, Kumud Dhital, Phillip Spratt, Paul Jansz, and Christopher S Hayward. Thrombolysis for suspected intrapump thrombosis in patients with continuous flow centrifugal left ventricular assist device. Artificial organs, 37(3):313–318, 2013.

[18] Castigliano M Bhamidipati, Gorav Ailawadi, James Bergin, and John A Kern. Early thrombus in a heartmate ii left ventricular assist device: a potential cause of hemolysis and diagnostic dilemma. The Journal of thoracic and cardiovascular surgery, 140(1):e7–e8, 2010.

[19] Jamil Borgi, Athanasios Tsiouris, Arielle Hodari, ChadMCogan, Gaetano Paone, and Jeffrey A Morgan. Significance of postoperative acute renal failure after continuousflow left ventricular assist device implantation. The Annals of thoracic surgery, 95(1):163–169, 2013.

[20] Ami M Patel, Gbemisola A Adeseun, Irfan Ahmed, Nanhi Mitter, J Eduardo Rame, and Michael R Rudnick. Renal failure in patients with left ventricular assist devices. Clinical Journal of the American Society of Nephrology, pages CJN–06210612, 2012.

[21] Nader Moazami, Walter P Dembitsky, Robert Adamson, Robert J Steffen, Edward G Soltesz, Randall C Starling, and Kiyotaka Fukamachi. Does pulsatility matter in the era of continuous-flow blood pumps? The Journal of Heart and Lung Transplantation, 34(8):999–1004, 2015.

[22] Takashi Yamane. What kinds of artificial hearts are available? In Mechanism of Artificial Heart, pages 3–12. Springer, 2016.

[23] Piergiorgio Tozzi, Audrey Maertens, Jonathan Emery, Samuel Joseph, Matthias Kirsch, and Franc¸ois Avellan. An original valveless artificial heart providing pulsatile flow tested in mock circulatory loops. The International journal of artificial organs, 40(12):683–689, 2017.

[24] Gino Gerosa, Silvia Scuri, Laura Iop, and Gianluca Torregrossa. Present and future perspectives on total artificial hearts. Annals of cardiothoracic surgery, 3(6):595, 2014.

[25] Nicholas H Cohrs, Anastasios Petrou, Michael Loepfe, Maria Yliruka, Christoph M Schumacher, A Xavier Kohll, Christoph T Starck, Marianne Schmid Daners, Mirko Meboldt, Volkmar Falk, et al. A soft total artificial heart—first concept evaluation on a hybrid mock circulation. Artificial organs, 41(10):948–958, 2017.

[26] Johannes Wappenschmidt, Simon J Sonntag, Martin Buesen, Sascha Gross-Hardt, Tim Kaufmann, Thomas Schmitz-Rode, Ruediger Autschbach, and Andreas Goetzenich. Fluid dynamics in rotary piston blood pumps. Annals of biomedical engineering, 45(3):554–566, 2017.

Chapter 5

Design, Modeling, and Experimental Characterization of A Valveless Pulsatile Flow Mechanical Circulatory Support (MCS) Device

Mengtang Li[1], Ye Chen[1], Marvin Slepian[2], Joseph Howard[1], Benjamin Thomas[1], Eric Barth[1]

1. Vanderbilt University, Nashville, TN

2. University of Arizona, Tucson, AZ

Submit to *ASME Journal of Biomechanical Engineering*

Status: To be Submitted

5.1 Abstract

Mechanical circulatory support (MCS) devices, i.e. ventricular assist devices (VADs) and total artificial hearts (TAHs), while effective and vital in restoring hemodynamics in patients with circulatory compromise in advanced heart failure, remain limited by significant adverse thrombotic, embolic and bleeding events. Many of these complications relate to chronic exposure, via these devices, to non-pulsatile flow and the high shear stress created by current methods of blood propulsion or use of prosthetic valves. Here we proposes a novel valveless pulsatile flow MCS device to: 1) lower the shear stress imparted to blood by dramatically reduced pump operating speed; 2) eliminate utilization of prosthetic valves thus diminishing potential shear stress generations; 3) allow direct flowrate control to generate physically desired blood flowrate include pulsatile flow; and 4) achieve compactness to fit into the majority of patients. The fundamental working principle and governing design equations are introduced first with multiple design and performance objectives presented. A first prototype was fabricated and experimental tests were conducted to validate

the model. After model validation, the proposed MCS was controlled to illustrate the ability of pulsatile flow generation. The presented work offers a novel MCS design and paves the way for next steps in device hemocompatibility testing.

5.2 Introduction

Heart failure, the final common pathway of all forms of heart disease, has a high prevalence domestically and globally, and is on the rise [1]. Mechanical circulatory support (MCS) devices, such as ventricular assist devices (VADs) and total artificial heart (TAH) [2-5], have emerged as approved frontline therapy, providing restoration of failing circulation, as either a bridge to transplantation, or an alternative to transplantation as destination therapy. While MCS is vital and effective in restoring hemodynamics, sadly, more than 70% of implanted MCS patients require re-hospitalization within one year of implant due to thrombosis and bleeding [6]. These adverse events are largely related to chronic blood exposure to disturbed, high shear, non-pulsatile flows [7, 8]. Infection from device bulk and exiting drivelines is a major limitation as well [9-11].

To attempt to overcome these adverse events, here we have taken a fresh look at contributory mechanisms which drive these complications. We advance a pump design which addresses fluid mechanical issues, as well as other design considerations which also contribute to observed adverse events limiting overall device safety and effectiveness. Specifically we hypothesize that a small foot print sliding vane pump, driven electrically, with optimized fluid mechanical properties will address design requirements and be an improvement in efficacy as an MCS system.

As such, we propose a novel MCS device with a design aimed at lowering shear stress imparted to blood via dramatically reducing pump speed and though the elimination of use of prosthetic valves. Our design further offers direct control of desired blood flow generation and is compact, reducing device bulk, for more ready patient fit and reduced infection risk. As a first step we define the design parameters and outline the fundamental principles

of the proposed design. Second, the geometry-governing design equations are derived and described, together with design and performance objectives. Third we present the construction of first prototypes along with the experiment testing setup. Finally, pump performance experimental results are presented including the ability of pulsatile flow generation. The present design offers an advance over present bulk bi-ventricular support/replacement systems.

5.3 Non-Compressing Single Sliding Vane MCS Pump

The proposed MCS pump, a non-compressing single sliding vane pump, consists of a rolling cylinder (rotor), a sliding vane, case(s), a flow straightener, and ports. The rotating cylinder has a through-all slot to allow the vane to slide through completely, and the vane separates the chamber into two compartments while pumping blood. Vitally, the wall geometry of the case is designed to serve as a guide for the vane to slide against, ensuring both ends of the vane touch the wall nearly continuously. The flow straightener straightens the flow into and out of the pump and also serves as a guide for the vane to slide against.

Two chambers are sectioned by the sliding vane and blood is pulled in and pumped out cyclically. As depicted in Fig. 5.1, as the vane rotates, the volume of one chamber is decreasing and blood is being pumped out while the volume of the other chamber is increasing and blood is being drawn in. Throughout this process, blood gently pulsates into and out of the MCS without need of prosthetic valves, the vane effectively serving as a valve.

5.4 Design of the Non-Compressing Single Sliding Vane MCS Pump

5.4.1 Geometric Design

A parametric equation describes the trajectory of the sliding vane's end-point, which in return determines the shape of the wall case.

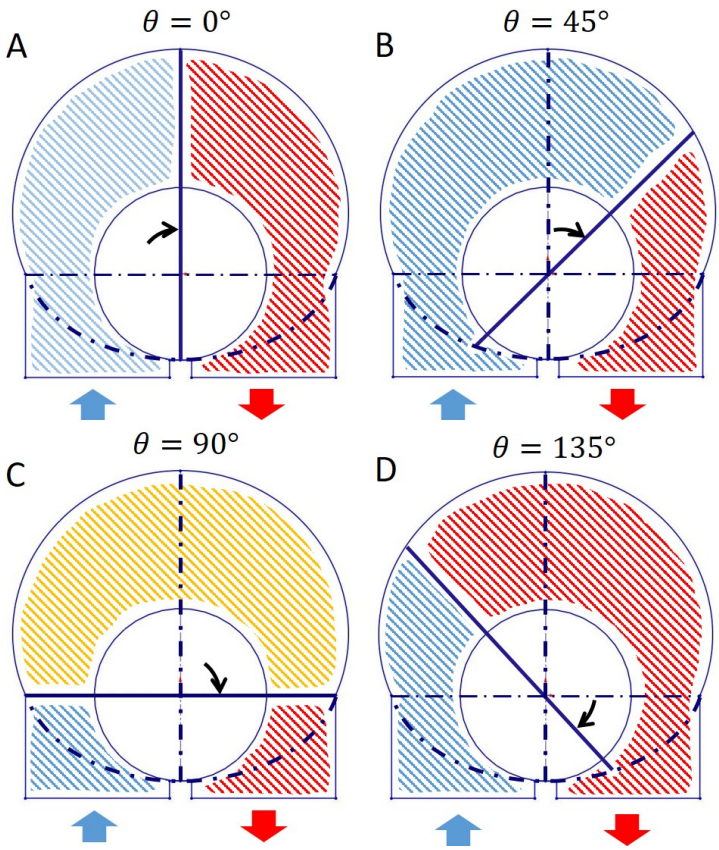

Figure 5.1: Working principle: Left blue arrow: inlet port, right red arrow: outlet port. Blue shaded area: low pressure, red shaded area: high pressure, yellow shaded area: middle pressure.

$$d_1(\theta) + d_2(\theta) = R + r + e \tag{5.1}$$

where d_1 and d_2 are distances from the two ends of the sliding vane to the center of the case respectively; θ is the rotating angle of the sliding vane, measured from the vertical position; R is pseudo radius of the case; r is the radius of the rolling cylinder; and e is the eccentricity, as shown in Fig. 5.2.

With boundary conditions $[d_1, d_2] = [R+e, r]$ at $\theta = 0$, $[d_1, d_2] = [(R+e+r)/2, (R+e+r)/2]$ at $\theta = \pi/2$, and $[d_1, d_2] = [r, R+e]$ at $\theta = \pi$, one smooth and continuous solution to Eqn. 5.1 is obtained as follows:

$$d_1(\theta) = \frac{1+\cos\theta}{2}(R+e) + \frac{1-\cos\theta}{2}r \tag{5.2}$$

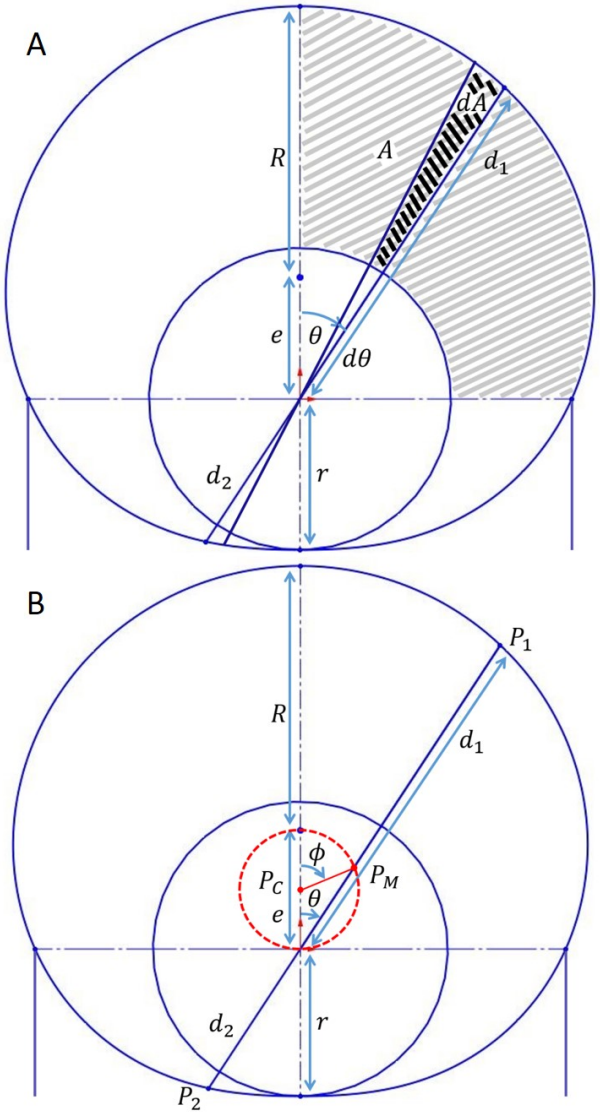

Figure 5.2: (A) Displacement and Instantaneous flowrate calculation (B) Kinematics of the sliding vane.

5.4.2 Porting

The chamber volume reaches a maximum when $\theta = \pi/2$, and in order to avoid compressing the working fluid, blood, porting should start at this position. Ideally porting should end at $\theta = \pi$ because this position mathematically separates the low- and high-pressure sides. Actual design results in a little narrow porting size and the porting ends at $\theta < \pi$ because wall thickness would occupy some space.

5.4.3 Displacement and Instantaneous Flowrate Calculation

Displacement volume of a VAD is vital as a trade-off between overall pump size and pump speed always exists and both of them are of vital significance. Therefore the next design step is to derive displacement equation. It can be seen from Fig. 5.1 and Fig. 5.2A that one full cycle pumps out 4-folded shaded volume. The planar area A is calculated as

$$\begin{aligned} A &= \frac{1}{2}\int_0^{\frac{\pi}{2}} d_1^2(\theta)d\theta - \frac{1}{4}\pi r^2 \\ &= \frac{1}{32}[(R+e)^2(3\pi+8) + r^2(3\pi-8) + 2\pi(R+e)r] - \frac{1}{4}\pi r^2 \end{aligned} \tag{5.3}$$

Therefore the overall displacement volume per revolution is obtained by multiplying planar area A and the chamber height h by four.

$$V_{disp} = 4Ah \tag{5.4}$$

The total size of the pump can be obtained similarly

$$A_{total} = \frac{1}{2}\int_0^{\pi} d_1^2(\theta)d\theta \tag{5.5}$$

$$V_{total} = 2A_{total}h \tag{5.6}$$

Another important feature of the proposed MCS pump is inherent pulsatility - even at constant rotational speeds. The instantaneous output flowrate, $Q(t)$, is equal to the change rate of an infinitesimal volume displacement, hdA, and infinitesimal time step, dt:

$$\begin{aligned} Q(t) &= \frac{hdA}{dt} = \frac{h(\frac{1}{2}d_1^2(\theta)d\theta - \frac{1}{2}r^2 d\theta)}{dt} = \frac{h}{2}(d_1^2(\theta) - r^2)\frac{d\theta}{dt} \\ &= \frac{h}{2}[(R+e)^2\cos^4\frac{\theta}{2} + r^2\sin^4\frac{\theta}{2} + \frac{(R+e)r}{2}\sin^2\theta - r^2]\dot{\theta} \\ t &\in [0, T/4], T = 2\pi/\omega \end{aligned} \tag{5.7}$$

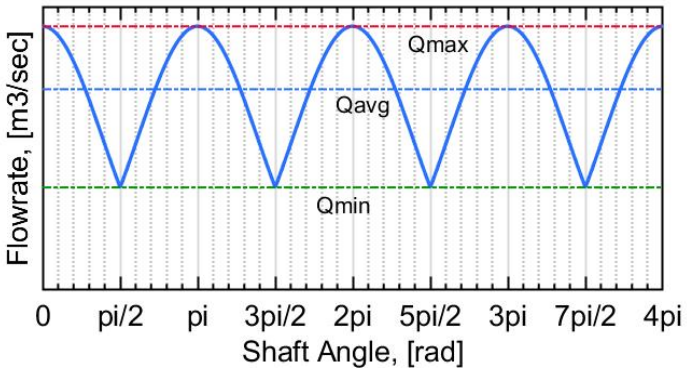

Figure 5.3: Instantaneous flowrate. Inherent pulsatile flow at a constant rotary speed.

Figure 5.3 plots out instantaneous flowrate $Q(t)$ against θ at a constant speed $\dot{\theta} = \omega$. It clearly shows that the instantaneous flowrate reaches its minimum at $\theta = ((2i+1)\pi)/2$ and its maximum at $\theta = 2i\pi$, $i \in N$. Therefore, two flow pulses are generated for every revolution (2π) of the driving shaft.

5.4.4 Kinematics of the Sliding Vane

The kinematics of the sliding vane are derived here to obtain a better understanding of the motion of the proposed MCS pump and also to allow easier motion definition in CFD simulation. From Eqns. 5.1 & 5.2, the instantaneous locations of the sliding vane's distal points P_1 and P_2 are

$$\begin{bmatrix} P_{1x}(\theta) \\ P_{1y}(\theta) \\ P_{2x}(\theta) \\ P_{2y}(\theta) \end{bmatrix} = \begin{bmatrix} d_1(\theta)\sin(\theta) \\ d_1(\theta)\cos(\theta) \\ d_2(\theta)\sin(\theta) \\ d_2(\theta)\cos(\theta) \end{bmatrix} \tag{5.8}$$

The instantaneous location of the center of mass P_M andits trajectory are obtained as follows:

$$\begin{bmatrix} P_{cx}(\theta) \\ P_{cy}(\theta) \end{bmatrix} = \begin{bmatrix} (P_{1x}(\theta) + P_{2x}(\theta))/2 \\ (P_{1y}(\theta) + P_{2y}(\theta))/2 \end{bmatrix} \tag{5.9}$$

$$P_{cx}^2(\theta) + (P_{cy}(\theta) - \frac{R+e-r}{4})^2 = (\frac{R+e-r}{4})^2 \tag{5.10}$$

where the geometric relation $\Phi = 2\theta$ exists according to Fig. 5.2B. It can be seen from Eqn. 5.10 that the center of mass of the sliding vane P_M forms a circular trajectory around $(0,(R+e-r)/4)$ with radius $(R+e-r)/4$. Conclusively, the motion of the sliding vane can be described as a combination of a circular motion of the center of mass at a speed $\dot{\Phi} = 2\dot{\theta}$ and a rotation of the rigid body about the center of mass at a speed $\dot{\theta}$.

5.4.5 Design Objectives and Constraints

The first objective is to allow the proposed pump to generate enough output flowrate, $\bar{Q}(t)$, to satisfy blood demand under the majority of body conditions. Accordingly, $6[LPM]$ is used here [12]. Second, as elevated shear stress within MCS devices leads to shear mediated platelet activation, causing many adverse hemocompatibility-related events [13], the rotor speed ω should be minimized, resulting in lower shear stress imparted to the blood [14]. Third, to avoid violating of multiple body cavities and to be as compact as possible under the standard fit criteria of a body surface area of $1.7[m^2]$ and an anteroposterior distance greater than $10[cm]$ from the sternum to the 10th thoracic vertebra [2], the overall pump size V_{total} should be minimized.

$$\bar{Q}(t) \in [0, 6LPM] \tag{5.11}$$

$$\min \omega \tag{5.12}$$

$$\min V_{total} \tag{5.13}$$

$$\max V_{disp}/V_{total} \tag{5.14}$$

With multiple conflicting objectives to be optimized, there exist various possible optimal designs. A Pareto front can be found through different optimization search algorithms.

Table 5.1: Sliding Vane MCS Pump Prototype Spec

Term	Variable	Value
Pseudo radius	R	$18[mm]$
Rolling cylinder radius	r	$10[mm]$
Eccentricity	e	$8[mm]$
Length of sliding vane	$d_1 + d_2$	$36[mm]$
Height of pump chamber	h	$18[mm]$
Displacement volume (per revolution)	V_{disp}	$24.8[mL]$
Inner diameter of port	d_{port}	$12.7[mm]$
Cross sectional area of port (each)	A_{port}	$126.68[mm^2]$

Besides the above design constraints, other geometric optimization needs also exist such as size ratio $|R/h-1|$ and shape or size of the flow straightener etc. Advanced computational fluid dynamics (CFD) is required to optimize the hemocompatibility design [15-17]. Since this is not the goal of this paper, a final design spec of a first generation prototype is given in Tab. 5.1.

5.5 Prototype Manufacture and Experiment Setup

To demonstrate the concept of the non-compressing single sliding vane pump, validate the model developed previously and illustrate the inherent pulsatility, a first generation prototype was designed, assembled and tested.

5.5.1 Methods

The design of the MCS pump is illustrated in Fig. 5.4. All blood contact parts were manufactured by computer numerical control (CNC) machine with polytetrafluoroethylene (PTFE). The lower and upper cases have counterbore-like structures to constrain the rolling cylinder to rotary motion only. The flow straightener was designed to offer a smooth guide for the vane to slide against. It also separates and prevents the flow path from inlet to outlet.

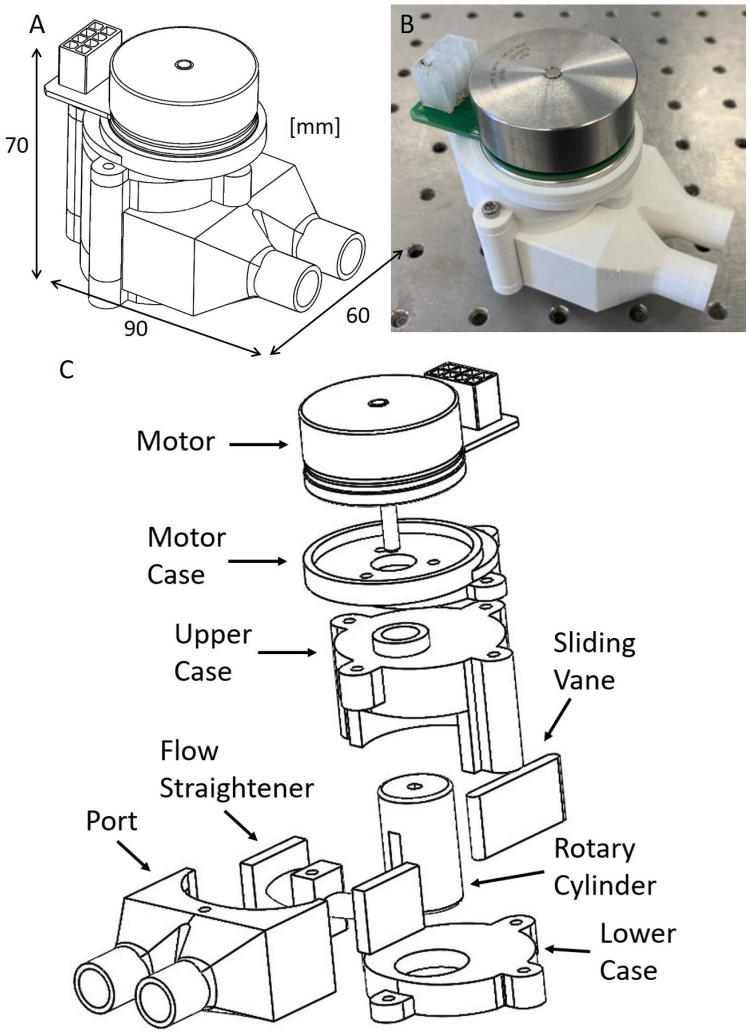

Figure 5.4: (A) isometric view of CAD design (B) exploded view of CAD design (C) isometric view of first prototype on an experimental bench table.

Different sizes and orientations of the ports are optional to better fitting with cardiac vessels and here a straight configuration with 0.50" ID was used here. Silicone sealant (GE) was used to provide further sealing between all surfaces. A brushless DC motor (Maxon EC 45) was used as a prime driver, with motor shaft filed to a D-shape profile. A motor case was 3D printed by acrylonitrile butadiene styrene (ABS) to fasten the motor and to couple with the pump. A custom-made motor with longer shaft and thinner rotor size may further compact the overall size of the MCS pump in the future.

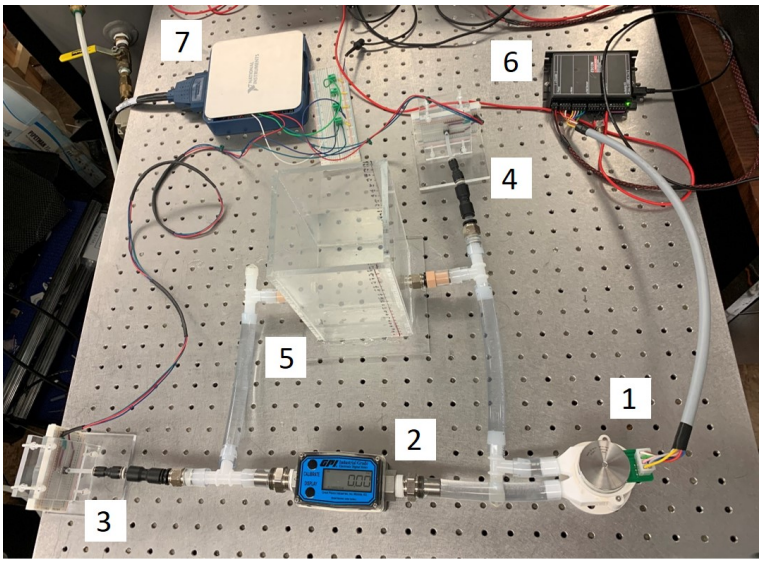

Figure 5.5: Experiment setup: (1) prototype MCS pump, (2) flow meter, (3) pressure sensor at outlet, (4) pressure sensor at inlet, (5) reservoir, (6) motor controller, (7) DAQ.

5.5.2 Experiment Setup

An experimental loop was constructed using 0.5" tubing to characterize the MCS pump performance and to show its inherent flow pulsatility, as shown in Fig. 5.5. An industrial grade flow meter (McMaster Part No. 4352K51) was placed at the outlet to measure the flowrate. The inlet and outlet pressures were measured by two Honeywell pressure transducers (Part No. ABPDANT005PGAA5). The motor speed was measured with motor's integrated hall-effect sensor. A mixture of water and glycerol with a mass ratio of 54 to 46 was circulated in the loop to represent the density ($1.10[g/mL]$) and viscosity ($3.6[mPaS]$) of blood [14]. The MCS prototype was controlled to run at several constant speeds against various pressure differences, which was achieved by a resistance clamp (not shown in the figure). The flowrate and pressure difference were chosen according to human heart operating conditions and range from 0 to $6[LPM]$ and 0 to $120[mmHg]$, respectively. All electronic control schemes and data collections were implemented using MATLAB Simulink and an xPC Target machine using a PCI-6229 National Instrument DAQ board.

5.6 Results of Experimental Test

5.6.1 MCS Pump Performance Characterization

A series of experiments were conducted with various operating conditions. The motor speed varied from 100 to 300$[RPM]$ while the system pressure difference was adjusted by the clamp from 0 to 120$[mmHg]$.

The resulting pressure difference versus flowrate curves (HQ curves) of the MCS prototype are shown in Fig. 5.6. Non-positive displacement feature can be noted that the flowrate decreases as the load pressure across the pump increases. Compared with prevailing rotary VADs such as Heartware, HeartMate2 [18] and CH-VAD [19], the sliding vane MCS pump have flatter HQ curves and can be regard as positive displacement pump with leakage. The reason behind the flatness is because of the positive displacement pump architecture. The leakage could be explained in Fig. 5.7 by that 1) gap between rolling cylinder and flow straightener's flow separator so there may be leakage from outlet directly to inlet; 2) gap between vane and wall so there may be leakage from one chamber to the other. Nonetheless, fairly linear relationships between pressure and flowrate are apparent ($R^2 > 0.9700$) and corresponding linear least squares regression fittings are obtained as follows (with Q, ω, and ΔP have units of $[LPM]$, $[RPM]$, and $[mmHg]$ respectively).

$$Q(\omega|_{100}, \Delta P) = -1.045 \times 10^{-2} \Delta P + 1.9095, R^2 = 0.9762 \tag{5.15}$$

$$Q(\omega|_{150}, \Delta P) = -9.01 \times 10^{-3} \Delta P + 3.2570, R^2 = 0.9804 \tag{5.16}$$

$$Q(\omega|_{200}, \Delta P) = -9.34 \times 10^{-3} \Delta P + 4.2960, R^2 = 0.9783 \tag{5.17}$$

$$Q(\omega|_{250}, \Delta P) = -9.10 \times 10^{-3} \Delta P + 5.4050, R^2 = 0.9702 \tag{5.18}$$

$$Q(\omega|_{300}, \Delta P) = -1.032 \times 10^{-2} \Delta P + 6.6086, R^2 = 0.9778 \tag{5.19}$$

Theoretically, with specifications shown in Tab. 5.1, the MCS pump is a positive dis-

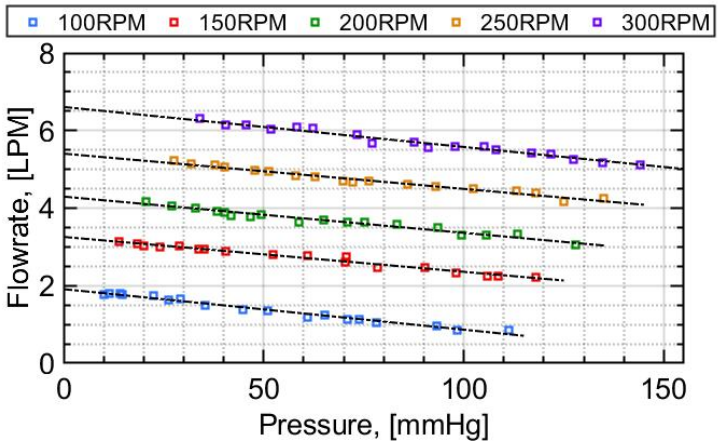

Figure 5.6: HQ curves. Colorful dots are from experiment measurements. Dash lines are linear data fitting curves.

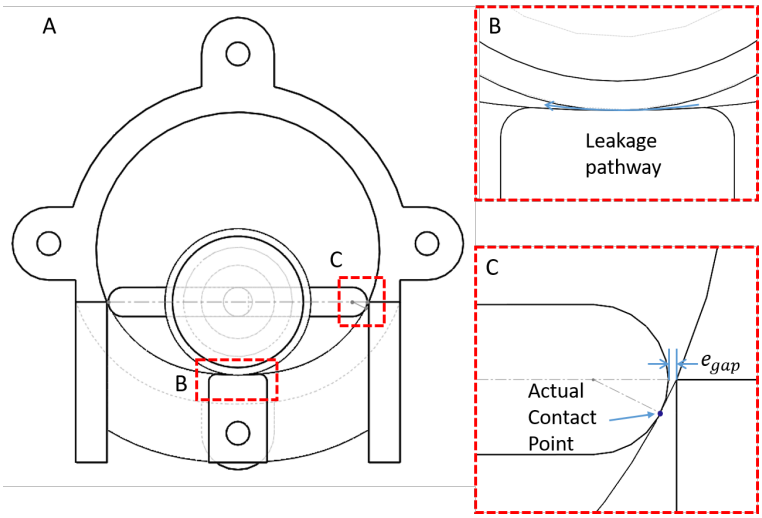

Figure 5.7: Geometric details: (A) gap between the rolling cylinder and flow straightener's flow separator, (B) because the sliding vane has thickness and circular ends, locations of two ends of the vane touches the wall vary along the circular end as the vane rotates. So the length of the sliding vane is shorter than the design value $d_1 + d_2$ (C) And this results in a gap between the vane and the wall as the vane is near $\theta = 0$ position.

placement pump and has a displacement of $24.8[mL/rev]$. The theoretical output flowrate with respect to rotary speed is plotted as a solid blue line in Fig. 5.8. No-leakage flowrates of the experimental MCS prototype pump under different operating speeds can be acquired by extrapolating the above linear fittings (dashed lines) and intersecting with the y-axis. The intersect points are depicted as red dots in Fig. 5.8. The no-leakage flowrates under

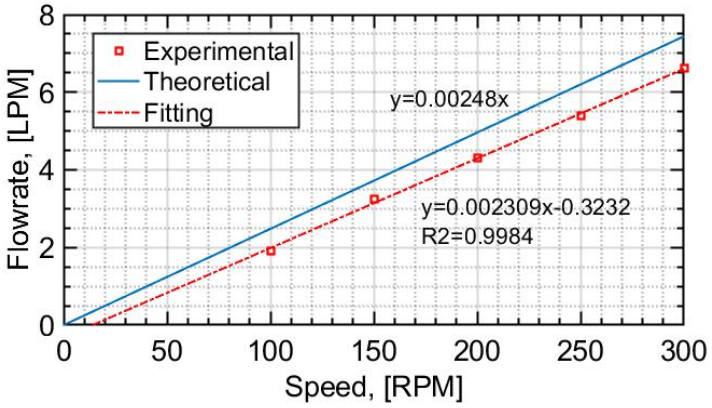

Figure 5.8: Comparison between theoretical and experimental displacements of the prototype MSC pump.

100 to 300$[RPM]$ show that the first prototype has a fairly linear displacement pumping ability with respect to rotary speed. The mathematical model developed previously for displacement calculation matches well with experimental displacement result (93.10%).

$$V_{disp:experimental}/V_{disp:theoretical} = 23.09/24.80 = 93.10\% \tag{5.20}$$

5.6.2 Pulsatile Flow

To illustrate the MCS pump's pulsatility, an estimator of the MCS flowrate is needed since accurate, high-bandwidth, flow meters are not available at an acceptable price. Even expensive and bulky flowmeters are either low-bandwidth or high-bandwidth but inaccurate at measuring low flowrates such as in this application. A first-order polynomial equation with $\Delta P[mmHg]$, and $\omega[RPM]$ as input variables was found to match well with the experiment data presented previously (Fig. 5.6) and is used here to estimate flowrate $Q(t)[LPM]$.

$$Q_{est}(t) = a_1\Delta P + a_2\omega + a_3 \tag{5.21}$$

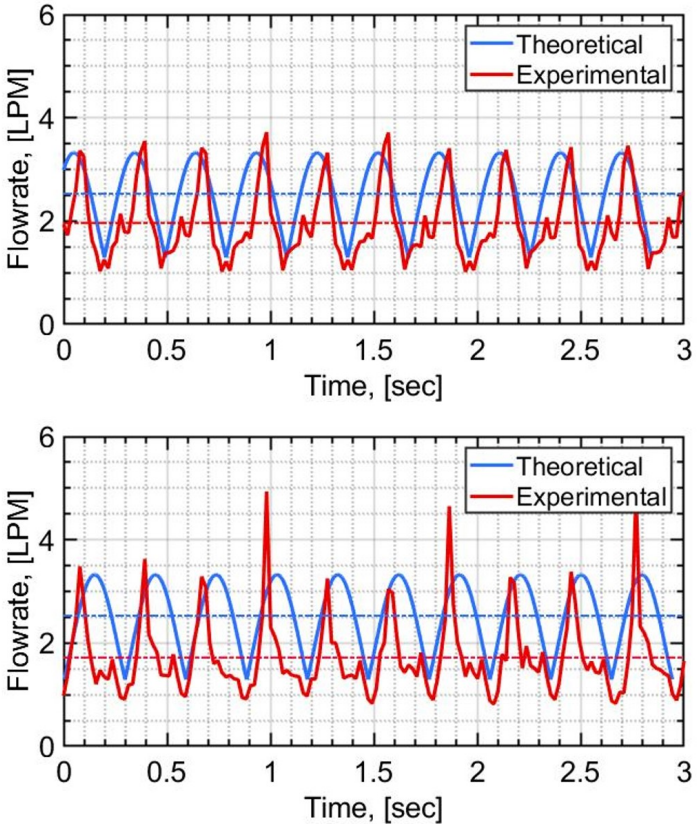

Figure 5.9: Theoretical flowrates v.s. experimental flowrates. Top: $\bar{\omega} = 101.9[RPM]$, $\Delta P = 26.34[mmHg]$; bottom: $\bar{\omega} = 101.5[RPM]$, $\Delta P = 98.45[mmHg]$. Dashed lines are average flowrates.

where parameters $(a_1, a_2, a_3) = (-9.644 \times 10^{-3}, 2.309 \times 10^{-2}, -3.233 \times 10^{-1})$. Real time pressure sensor data and motor speed data were collected and resampled due to the sensors' different sampling frequencies before the data were plugged into Eqn. 5.21. The estimated flowrate, Q_{est}, was then compared with the theoretical flowrate and these flowrate curves under several operating conditions are plotted in Figs. 5.9-5.11.

As Figs. 5.9-5.11 illustrate, the estimated instantaneous flowrate of the prototype MCS pump shows clear pulsatile behavior. Flowrate varies noticeably as the rotary angle increments. Additionally, although the estimated instantaneous flowrate does not match very well with the theoretical model, the instants where the flowrate reaches a minimum or a maximum and the pulsatile frequency are captured by the model nicely. Lastly, since the

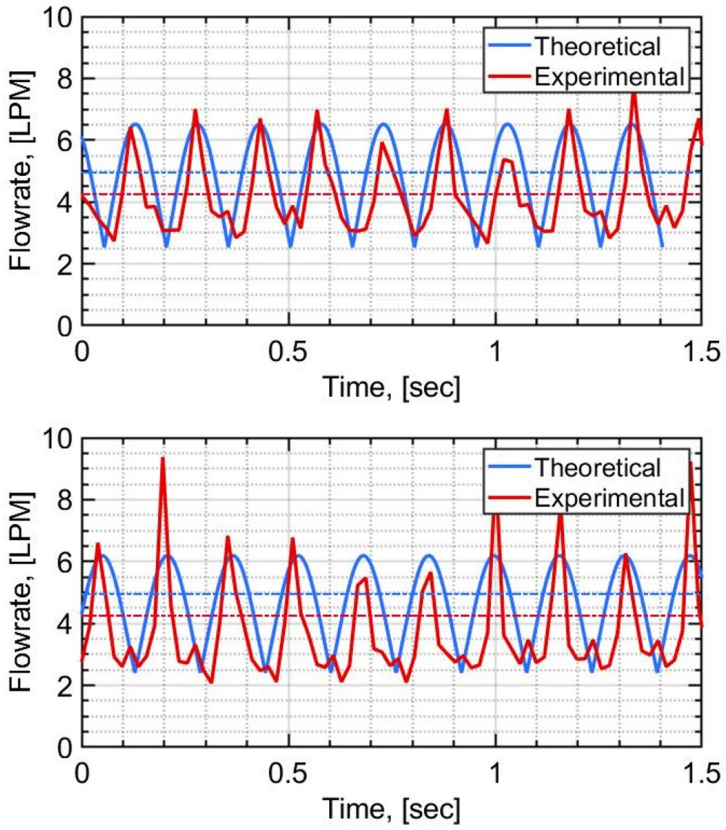

Figure 5.10: Theoretical flowrates v.s. experimental flowrates. Top: $\bar{\omega} = 196.2[RPM]$, $\Delta P = 27.17[mmHg]$; bottom: $\bar{\omega} = 195.6[RPM]$, $\Delta P = 105.5[mmHg]$. Dashed lines are average flowrates.

first-order polynomial fitting function to calculate the instantaneous flowrate is derived using the data in Fig. 5.6, the discrepancy between the average experimental (fitting) flowrate and the average theoretical flowrate is consistent with the data in Fig. 5.7.

5.7 Discussion

The fundamental working principle and geometrical design of a novel valveless pulsatile flow MCS pump are introduced in this work. It presents the geometric governing equations in mathematical forms along with performance objectives and constraints. Conflicting objectives exist such as the displacement volume and pump rotary speed. Both of them are of vital significance because on the one hand the available space inside pa-

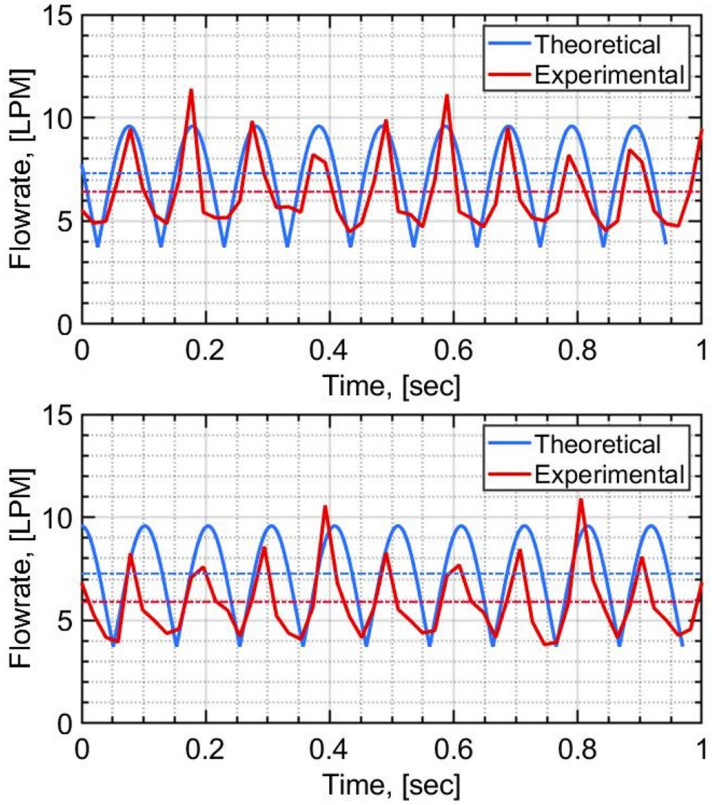

Figure 5.11: Theoretical flowrates v.s. experimental flowrates. Top: $\bar{\omega} = 295.6[RPM]$, $\Delta P = 33.92[mmHg]$; bottom: $\bar{\omega} = 294.1[RPM]$, $\Delta P = 121.7[mmHg]$. Dashed lines are average flowrates.

tient's chest is limited so a compact MCS device is required, on the other hand, elevated shear stress within MCS devices caused by high velocity gradient leads to shear mediated platelet activation, causing many adverse hemocompatibility-related events. This can be used to explore the parameter space and optimize future generation prototypes. Also, the design methods presented in this work serve as a starting point for future CFD and fluid structure interaction (FSI) simulation studies to further optimize the size-speed trade-off and to optimize detailed geometry to improve the device hemocompatibility of the proposed MCS pump [16, 17].

A first generation prototype was fabricated. A more compact size is achievable. Initially, considering the material property of PTFE, the original design has redundant wall thickness and couterbore-like hole depth to prevent possible break down of parts. A stiffer

and harder material will eventually result in a thinner wall (from 5[mm] to 3[mm]) and a shallower hole (from 5[mm] to 3[mm]) to restrain the motion of the rolling cylinder. A custom-made motor with a longer shaft will shorten the couterbore-like hole of the upper case from 10[mm] to 5[mm]. Do note that the overall size depends more on the pump rotary speed.

Experimental tests were conducted to characterize the MCS pump prototype and to validate the model developed. HQ curves of the proposed MCS pump were experimentally measured. As briefly described in Chapter 5.6.1, the leakage could happen between the rolling cylinder and the flow straightener. A mechanism like a wiper blade between them would effectively prevent leakage through this pathway. Another possible leakage source is the gap between the vane and the wall. Although other solutions to Eqn. 5.1 exist to allow constant contact between sliding vane end and the wall, manufacture tolerance still exists, leading to gaps. Smaller gaps will lead to less backflow leakage, thus increasing the pump efficiency. However, this will also contribute to higher shear stresses onto blood, causing blood damage.

The proposed MCS pump, mathematically and experimentally, showed a more physiologic pulsatile flow generation, compared to the attenuated or non-pulsatile flow generated from prevailing rotary VADs. This inherent feature may prevent medical complications associated with prevailing rotary pumps [7,8]. Since accurate, high-bandwidth, flow meters are not available at an acceptable price and expensive and bulky flowmeters are either low-bandwidth or high-bandwidth and inaccurate at low flows such as this application, a flowrate estimator using polynomial fittings was adopted. Note that the coefficient for rotary speed $\omega(t)$ in Eqn. 5.18 is larger than that for pressure difference $\Delta P(t)$, the pulsatility of the resulting estimated flowrate $Q_{est}(t)$ partially comes from the motor rotation oscillation (which in future word could be controlled to promote a particular pulse shape). Nonetheless, the polynomial flowrate estimator still captured the time steps where the flowrate reaches minimum or maximum and pulsatile frequency.

5.7.1 Novelty and Improvements of the Proposed Design

Initial MCS designs largely relied on pulsatile membrane based displacement systems, for both VAD and TAH design. These system required a drive mechanism which was initially pneumatic with cumbersome hoses and air supplies. Analogous to a real human heart to produce pulsatile physiologic flow to the circulatory system, the first generation of VADs (e.g. Berlin Heart EXCOR, Thoratec HeartMate, Abiomed AB5000) and the only FDA approved TAH, SynCardia TAH [20], adopts fixed volume displacement fashion that incorporates sacs, diaphragms or pusher plates actuated pneumatically, electrically or mechanically. Blood is pulled into a flexible chamber from left or right ventricle and pushed out into ascending aorta or pulmonary artery while uni-directional blood flow is guaranteed by prosthetic valves. Although they could generate pulsatile physiologic blood flow, these pumps 1) inherently are bulky which make them difficulty to fit into many patients [21], 2) have large blood contacting surfaces which require frequent coagulation of warfarin, aspirin and dipyridamole to maintain high international standard ratio (INR) [22], and have potential mechanical failures caused by flexible membranes or diaphragms fatigue [23].

To circumvent the disadvantages mentioned above, a hydrodynamic blood pump generating continuous flow instead of pulsatile flow was invented and favored by researchers and manufactures thanks to its distinct advantages of compactness and durability. These second generation VADs (e.g. Thoratec HeartMate2, Reliant Heart HeartAssist5, Berlin Heart INCOR) normally consist a fast spinning impeller (5000-10000 RPM), a flow straightener and a diffuser. Due to its working principle, the flowrate depends on the pressure difference across the VAD, which requires precise sensors and cardiovascular models and control algorithms to generate desired blood flows. The dramatically high velocity at the impeller edge contributes high shear stress to blood, inducing hemolysis and platelet activation [23]. Also, thrombus may format in regions of recirculation or stagnation such as the stationary flow straightener [23]. The third generation of VADs (e.g. Thoratec HeartMate3, HeartWare HVAD) and some TAHs (e.g. BiCACOR TAH, Cleveland SmartHeart

TAH), utilizing centrifugal pumping architecture, has lower pump speed (5000 RPM) due to higher hydraulic efficiency. Generally, blood enters into the rotor and is driven outward centrifugally to the aorta or pulmonary artery without the need for flow straighteners at the inlet or diffusers at the outlet, thus lowering the probability to induce hemolysis and platelet activation. Still, noticeably high shear stresses, thus leading to blood damage, were generated inside the pumps and much research has been done with in-silico design tos optimize the pump geometry [15-17].

To unify the benefits of pulsatility from piston pumps, high hydro-efficiency from hydrostatic pumps (positive displacement) [24], and compactness, durability and valveless features from hydrodynamic pumps (e.g. 2nd and 3rd VADs and some TAHs), an alternative pump type called the rotary piston pump [14] was invented and studied. Compared with normal rotary VADs, rotary piston pumps generate pulsatile flow under a dramatically reduced motor speed, which theoretically results in reduced complications and lowered shear stress. A wankel-like VAD [14], a wobbling disk VAD [25], a spherical gerotor TAH [26], a spherical rolling disk TAH [27], and the commercial available Torvad VAD are all good examples of rotary piston pumps.

5.8 Conclusion

This paper presents the basic operating principles and design methods for a novel non-compressing single sliding vane MCS pump. An experimental prototype was built and experimental tests were conducted to characterize the pump performance and to validate the design model. The inherent ability to generate pulsatile flow was also illustrated. The presented work offers a novel MCS design and paves the way for device hemocompatibility tests. In the future work, design optimization via optimal search and advanced CFD will be utilized to achieve a more compact size and to further lower device generated shear stress imparted onto the blood.

5.9 Acknowledgement

We acknowledge support from Discovery Grant of Vanderbilt University, support from Doris Griswold Heart Award from Sarver Heart Center of University of Arizona, and support from the Arizona Center for Accelerated Biomedical Innovation (ACABI) of University of Arizona.

5.10 References

[1] Emelia J Benjamin, Paul Muntner, and M´arcio Sommer Bittencourt. Heart disease and stroke statistics-2019 update: A report from the american heart association. Circulation, 139(10):e56–e528, 2019.

[2] Jack G Copeland, Richard G Smith, Francisco A Arabia, Paul E Nolan, Gulshan K Sethi, Pei H Tsau, Douglas McClellan, and Marvin J Slepian. Cardiac replacement with a total artificial heart as a bridge to transplantation. New England Journal of Medicine, 351(9):859–867, 2004.

[3] Mark S Slaughter, Joseph G Rogers, Carmelo A Milano, Stuart D Russell, John V Conte, David Feldman, Benjamin Sun, Antone J Tatooles, Reynolds M Delgado III, James W Long, et al. Advanced heart failure treated with continuous-flow left ventricular assist device. New England Journal of Medicine, 361(23):2241–2251, 2009.

[4] Martin Strueber, Gerry O'Driscoll, Paul Jansz, Asghar Khaghani, Wayne C Levy, George M Wieselthaler, HeartWare Investigators, et al. Multicenter evaluation of an intrapericardial left ventricular assist system. Journal of the American College of Cardiology, 57(12):1375–1382, 2011.

[5] Marvin J Slepian, Yared Alemu, Jo˜ao Silva Soares, Richard G Smith, Shmuel Einav, and Danny Bluestein. The syncardia™ total artificial heart: in vivo, in vitro, and computational modeling studies. Journal of biomechanics, 46(2):266–275, 2013.

[6] Van-Khue Ton, Rongbing Xie, Jaime A Hernandez-Montfort, Bart Meyns, Takeshi Nakatani, Masanobu Yanase, Steve Shaw, Stephen Pettit, Ivan Netuka, James Kirklin, et al. Short-and long-term adverse events in patients on temporary circulatory support before durable ventricular assist device: An imacs registry analysis. The Journal of Heart and Lung Transplantation, 39(4):342–352, 2020.

[7] James K Kirklin, Francis D Pagani, Robert L Kormos, Lynne W Stevenson, Elizabeth D Blume, Susan L Myers, Marissa A Miller, J Timothy Baldwin, James B Young, and David C Naftel. Eighth annual intermacs report: special focus on framing the impact of adverse events. The Journal of Heart and Lung Transplantation, 36(10):1080–1086, 2017.

[8] Randall C Starling, Nader Moazami, Scott C Silvestry, Gregory Ewald, Joseph G Rogers, Carmelo A Milano, J Eduardo Rame, Michael A Acker, Eugene H Blackstone, John Ehrlinger, et al. Unexpected abrupt increase in left ventricular assist device thrombosis. New England Journal of Medicine, 370(1):33–40, 2014.

[9] Mi-Suk Jung, Jea-Hurn Bae, and Yang-Ha Kim. Relationships between dietary intake and serum lipid profile of subjects who visited health promotion center. Journal of the Korean Society of Food Science and Nutrition, 37(12):1583–1588, 2008.

[10] Anne-Marie Leuck. Left ventricular assist device driveline infections: recent advances and future goals. Journal of thoracic disease, 7(12):2151, 2015.

[11] Gabriel A Hernandez, Jonatan D Nunez Breton, and Sandra V Chaparro. Driveline infection in ventricular assist devices and its implication in the present era of destination therapy. Open journal of cardiovascular surgery, 9:1179065217714216, 2017.

[12] Bente Kristina Thamsen. A two-stage rotary blood pump design to reduce blood trauma. PhD thesis, Technische Universit¨at Berlin, 2016.

[13] Mengtang Li, RyanWalk, Yana Roka-Moiia, Jawaad Sheriff, Danny Bluestein, Eric J Barth, and Marvin J Slepian. Circulatory loop design and components introduce artifacts impacting in-vitro evaluation of ventricular assist device thrombogenicity: A call for caution. Artificial Organs, 2019.

[14] Johannes Wappenschmidt, Simon J Sonntag, Martin Buesen, Sascha Gross-Hardt, Tim Kaufmann, Thomas Schmitz-Rode, Ruediger Autschbach, and Andreas Goetzenich. Fluid dynamics in rotary piston blood pumps. Annals of biomedical engineering, 45(3):554–566, 2017.

[15] Katharine H Fraser, Tao Zhang, M Ertan Taskin, Bartley P Griffith, and Zhongjun J Wu. A quantitative comparison of mechanical blood damage parameters in rotary ventricular assist devices: shear stress, exposure time and hemolysis index. Journal of biomechanical engineering, 134(8), 2012.

[16] Gaurav Girdhar, Michalis Xenos, Yared Alemu, Wei-Che Chiu, Bryan E Lynch, Jolyon Jesty, Shmuel Einav, Marvin J Slepian, and Danny Bluestein. Device thrombogenicity emulation: a novel method for optimizing mechanical circulatory support device thromboresistance. PloS one, 7(3), 2012.

[17] Danny Bluestein, Shmuel Einav, and Marvin J Slepian. Device thrombogenicity emulation: a novel methodology for optimizing the thromboresistance of cardiovascular devices. Journal of biomechanics, 46(2):338–344, 2013.

[18] Mumin R Noor, Chong H Ho, Kim H Parker, Andre R Simon, Nicholas R Banner, and Christopher T Bowles. Investigation of the characteristics of heart ware hvad and thoratec heart mate ii under steady and pulsatile flow conditions. Artificial organs, 40(6):549–560, 2016.

[19] Zachary BK Berk, Jiafeng Zhang, Zengsheng Chen, Douglas Tran, Bartley P Griffith, and Zhongjun JWu. Evaluation of in vitro hemolysis and platelet activation of a newly developed maglev lvad and two clinically used lvads with human blood. Artificial organs, 43(9):870–879, 2019.

[20] Marvin J Slepian, Richard G Smith, and Jack G Copeland. The syncardia cardiowest™ total artificial heart. FUNDAMENTAL AND CLINICAL CARDIOLOGY, 56:473, 2006.

[21] Eric H Maslen, Gill B Bearnson, Paul E Allaire, Ronald D Flack, Michael Baloh, Edgar Hilton, Myounggyu D Noh, Don B Olson, Pratap S Khanwilkar, and James D Long. Artificial hearts. In Proceedings of the 1997 IEEE international conference on control applications, pages 204–209. IEEE, 1997.

[22] Thorsen Drews, Matthias Loebe, Ewald Hennig, Friedrich Kaufmann, Johannes Muller, and Roland Hetzer. The 'berlin heart'assist device. Perfusion, 15(4):387–396, 2000.

[23] Daniel Timms. A review of clinical ventricular assist devices. Medical engineering & physics, 33(9):1041–1047, 2011.

[24] Mengtang Li, Ryan Foss, Kim Stelson, James Van de Ven, and Eric John Barth. Design, dynamic modelling and experiment validation of a novel alternating flow variable displacement hydraulic pump. IEEE/ASME Transactions on Mechatronics, 2019.

[25] Fengxiang Lin, Ligang Yao, Rongye Zheng, Wenjian Li, and Changsheng Fang. A novel ventricular assist miniscule maglev nutation pump: Structure design, 3d modelling and simulation. In Mechanism and Machine Science, pages 443–453. Springer, 2016.

[26] Mengtang Li and Eric J Barth. Spherical gerotor: Synthesis of a novel valveless pulsatile flow spherical total artificial heart. Journal of Mechanics Engineering and Automation, 8(7):281–292, 2018.

[27] Piergiorgio Tozzi, Audrey Maertens, Jonathan Emery, Samuel Joseph, Matthias Kirsch, and Franc¸ois Avellan. An original valveless artificial heart providing pulsatile flow tested in mock circulatory loops. The International journal of artificial organs, 40(12):683–689, 2017.

Chapter 6

A "Servopump" for Soft Robotics

Mengtang Li, Benjamin Thomas, Joseph Howard, Eric Barth

Vanderbilt University, Nashville, TN

Submit to *Soft Robotics*

Status: Under Review

6.1 Abstract

A hydraulic "servopump" for soft robotics that directly powers soft actuators is proposed and presented here. This is akin to a servomotor for traditional robotics that is suitable for closed-loop feedback control. This miniature hydraulic power unit (mHPU), based on a gerotor architecture and driven by a DC motor, features compactness, convenience, high bandwidth and high power density. It offers a highly controllable actuation package that current soft robotic systems lack. A design methodology is presented for sizing the mHPU for a given flowrate. A prototype is demonstrated for a target application with a flowrate of ±3 L/min and maximum output pressure of 500kPa (77 psig). Our first-generation prototype was designed and fabricated with a positive-displacement gerotor architecture of 0.5 mL/rev directly driven by a 60W brushless DC motor. The mHPU prototype was characterized in terms of flowrate (as a function of speed and pressure load), efficiency (volumetric, mechanical, electrical and total efficiency), and control bandwidth. Energy efficiency of the proposed mHPU offers a peak efficiency near 45%, offering comparable efficiencies of non-soft servomotor actuated systems. Bandwidth characterization demonstrated the mHPU has a bandwidth of approximately 35 Hz, which is well above

the mechanical frequency of many soft robots and results in high control authority. As a demonstration of the control capabilities of the mHPU, the position of a basic fluidic muscle was controlled with a simple PID controller and exhibited a fast and accurate step response (1.6 cm step in 250ms with a steady-state accuracy of 0.2 mm).

6.2 Introduction

robotics utilizes the compliance and adaptability of soft materials to interact with humans and the environment more adeptly and safely than conventional rigid-body robots made with high stiffness materials [1]. Compared to rigid robots, soft robots have shown superiority in performing tasks in unstructured and undefined environments. The elastic and soft material properties, on one hand, grant a soft robot the ability to bend, stretch and contract, but, on the other hand, require special actuation methods other than conventional robotic actuators such as motors with gearheads. It is critical that soft robots, especially in mobile applications, have a power supply and actuation system with high power density, high control bandwidth, and high efficiency. The goal herein is to fill the gap of having no viable compact, convenient, high bandwidth and high power density direct power unit for soft robotics. Anecdotally, many videos of soft robots exist with "4X" or even "10X" is shown in the corner of the video. The intent of the power unit presented in this paper is to put an end to such slow responses and enable soft robotics to be controlled with impressive bandwidths and accuracies.

Some common actuation methods studied in soft robotics include cable (tendon) drive, fluidic actuation (pneumatics and hydraulics) and shape memory alloy (SMA) [1].

Cable drives allow for the transfer of very high tensile strength and forces to a manipulator from a distant power source along its longitudinal axis while also permitting bending in other directions without noticeable strength loss. With these unique features, the system moment of inertia is low and movements of joints and manipulators are not affected. Although cables can be guided through complex routes and mounted to the system easily

and tightly (e.g. a spine [2]), adequate space to include a power source such as a spooler motor can make the whole soft robotic system bulky. Nonetheless, due to is simplicity, the cable driven method is a very common actuation method for soft continuum robots [3-7], soft robotic manipulators (for instance an octopus inspired arm uses embedded cables for reaching [8, 9]) and soft robot locomotions (for example a cable driven fish robot [10]).

Pneumatic actuation dates back to the 1950s when McKibben invented an unbraided chord tube, which replicated the functionality of contracting muscle when pressurized. Inspired by the McKibben actuator, more-recently developed unbraided channeled silicon molds, often called PneuFlex Actuators [11], Pneumatic Networks (Pneu-Nets) [12], or PneuFlex Actuator [13], have been shown not only to have the ability to contract and expand but also to bend. Because pneumatic networks are lightweight and can operate using ambient air, this actuation method has been adopted by many bio-inspired soft robots such as a resilient quadrupedal robot [14]. A fish-like robot [15], a snake-like robot [16], and a manta ray-like robot [17]. However, using pressurized air inevitably limits the mobility of any pneumatic powered soft robots since the source is normally connected to a building or at least a large air tank. Even though some studies showed on-board chemical decomposition of gas generation in a closed container could be used to generate the pressure [18], this method will not be able to replace the traditional pressure source. Another noticeable disadvantage of pneumatics comes from its poor efficiency and poor dynamic behavior due to the compressibility of the working fluid.

Hydraulic actuation shares many similarities with pneumatic actuation as both approaches regulate internal pressure to deform a structure in a controlled manner and some soft robots can be powered by either method [19]. In contrast to most pneumatic systems, hydraulic systems normally contain a closed loop of working fluid, enabling them to function in untethered environment such as an under-water robotic fish [20] or in a mobile application such as a rehabilitation device [21] or an exoskeleton [22-24]. Although hydraulics provide larger forces and faster system dynamics than pneumatics, classic system circuits

contain pressure regulators, directional valves, and accumulators, making traditional hydraulics unsuitable for small-package designs. Electro-hydraulic actuators (EHAs) offer an alternative approach to directly supply power to actuators by varying the speed of an electric drive motor connected to a fixed displacement hydraulic pump, eliminating the need for conventional control valves [25-27] which are bulky and exhibit low efficiency.

Shape memory alloy is a novel, light, simple, and deformable material of interest to soft robot developers thanks to its ability to revert to its original position and orientation when heated. This unique effect has been utilized by researchers to actuate various soft robots, such as a meshworm robot inspired by the peristaltic of Oligochaetes [28], the GoQBot, a soft body rolling robot inspired by a caterpillar [29], and octopus like robots [30, 31]. The most significant drawback to adopting SMAs more broadly in soft robotic systems is material hysteresis, as cooling the material takes more time than heating [32], which makes SMAs not suitable for many bi-directional applications. SMAs also exhibit low bandwidth compared to other forms of soft actuation.

Inspired by EHAs, this paper proposes a novel actuation method for soft robotics, as a parallel counterpart to that for rigid robots. In rigid robots, servo motors with gear heads offer high bandwidth, fast dynamics, controllability, and compactness. The proposed ''servopump" for soft robotics contains a high power density motor plus a pump head, which can easily be matched to different applications. We envision a day when such a pumphead that can be ordered from a motor manufacturer for soft robotics, where a gearhead would have been ordered for traditional rigid robotics. In Chapter 6.3, the basic principles of the miniature hydraulic power unit are presented first followed by detailed geometry design methods and optimization targets. To illustrate the compactness and power density of the mHPU, an energy efficiency evaluation model is also established. Next, methods described previously were implemented to design an experimental prototype for a follow-up soft bending actuator in Chapter 6.4. The results of experimental tests for the mHPU prototype are provided in Chapter 6.5, including bandwidth characterization and various energy

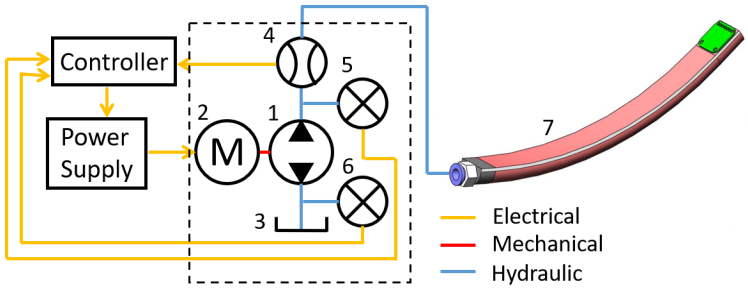

Figure 6.1: Schematics of a hydraulic powered soft actuator. (1) pump head, (2) electric motor, (3) reservoir (can be excluded depending on applications), (4) flow meter, (5) outlet pressure sensor, (6) inlet pressure sensor, (7) soft actuator.

efficiency evaluations. In Chapter 6.6, the proposed mHPU was used to control the position of a fast-prototyped fluidic muscle to illustrate its suitability to power up soft robotics. A discussion follows in Chapter 6.7 and Chapter 6.8 draws the concluding remarks.

6.3 Miniature Hydraulic Power Unit

The proposed miniature hydraulic power unit for soft robotic actuators is a compact portable bi-directional micropump driven by a DC motor and can be visualized in Fig. 6.1. It primarily consists of a micropump head and a DC motor, together with optional pressure sensors and flowmeters. By eliminating solenoid and/or proportional valves used frequently in pneumatic approaches for flow direction control, the mHPU is controlled by converting electric energy into hydraulic energy, actuating the soft robot directly. This not only makes the overall system compact, but also improves the system's energy efficiency, compared to pneumatic actuation method [33,34]. The absence of valves and mechanical transmission lines also permits back-drivability of the power unit, enhancing the fidelity and types of feedback control architectures that can be applied (such as impedance control or force/pressure control).

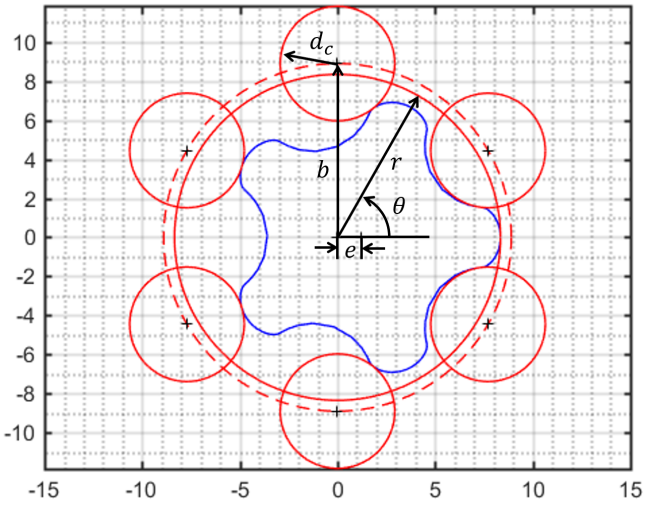

Figure 6.2: Circular-toothed gerotor gearset. Design parameters include: the distance from the center of outer rotor to the center of outer gear tooth b, the eccentricity between the inner rotor and outer rotor e, the outer gear tooth radius d_c, the outer gear "root radius" r, and the number of outer rotor gear teeth m.

6.3.1 Pump Head Core Geometry

With the aim of designing a compact power unit, the pump head is desired to have adequate displacement (amount of working fluid pumped out per shaft revolution) while occupying little space. Since the main goal is to deliver power instead of flow, only positive displacement (hydrostatic) pump architectures are considered instead of hydrodynamic ones. Among candidate micro pump architectures, annular gear (gerotor) stands it out due to its high displacement to size ratio, simple and compact with inherently low sound and vibration (though higher cost to custom manufacture), and bi-directionality [35].

The geometric profile of a circular-toothed gerotor is well studied and a detailed method for profile design can be found in the literature [36, 37]. The inner and outer gerotor gear profiles are determined by an epitrochoid and its conjugate, parameterized by the design variables shown in Fig. 6.2. Consequently, as the inner rotor rotates at a speed n, the outer rotor rotates at $n(m-1)/m$.

6.3.2 Design and Optimization

In addition to designing for a maximum volumetric flowrate, the following and their tradeoffs must also be considered when designing and optimizing the mHPU: 1) flow ripple (variation in flow output over a single pump cycle), 2) net displacement per revolution (the amount of working fluid pumped per shaft revolution), and 3) cavitation (bubbles or cavities formed within a pump that impart stress to the pump and working fluid upon imploding). Minimizing ripple allows for more accurate flowrate control at the cost of greater pump size. For example, the authors in [37] demonstrated that a gerotor design with m=6 outer rotor gear teeth outputs less ripple than a gerotor with m=5 outer rotor gear teeth, though the latter design is more compact. Ripple also becomes less noticeable when pump displacement is small (within an order of magnitude of 0.1 mL/rev) and the pump rotary speed is fast.

Furthermore, ideal pump displacement D, operating speed n, pump head height h, and the facial displacement area $A(b,e,d_c,r,m)$, must also match to the characteristics of the electric motor driving the pump. Compared with brushed DC motors, brushless DC motors (BLDC) show higher power density and less friction and are therefore well suited to drive the pump head. Because BLDC motors work more efficiently at high speeds and medium load torques [38], a small displacement D is preferred. The displacement cannot be too small, however, since the volumetric efficiency would also drop significantly, leading to a high leakage flowrate as a portion of the total theoretical flowrate $Q_{th}(n)$.

$$D = A(b,e,d_c,r,m) \tag{6.1}$$

$$Q_{th}(n) = A(b,e,d_c,r,m)hn \tag{6.2}$$

Maximum flowrate (and maximum pump speed) are also limited by the pump's potential for cavitation, which could occur in response to low pressure generated behind the rotor

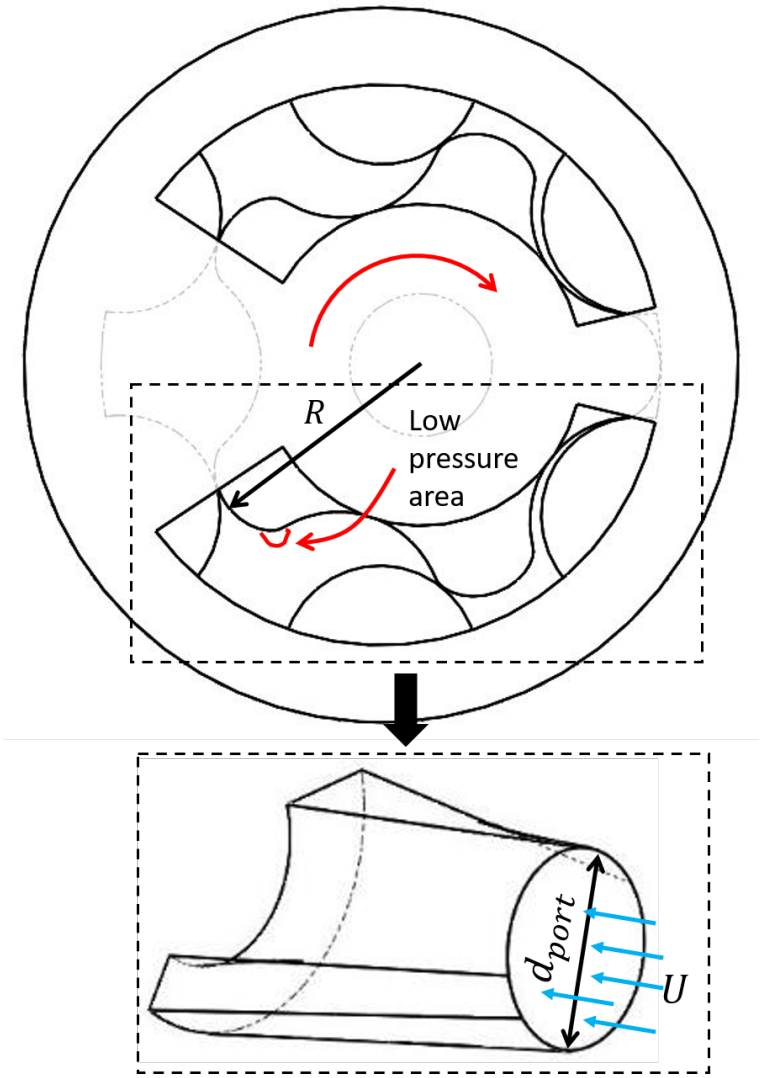

Figure 6.3: Gerotor port and equivalent port gallery.

or coinciding with turbulent flow conditions. In the first case, as the pump core rotates, the region behind the inner rotor lobe tip (as indicated in Fig. 6.3) establishes a pressure drop:

$$\Delta P = 0.5\rho V^2 \tag{6.3}$$

where ρ is the density of working fluid and V is the speed of inner rotor lobe tip.

Cavitation begins when the pressure drops below the vapor pressure of the working

fluid:

$$\Delta P = P_{atmo} - P_{vapor} \tag{6.4}$$

So the maximum permissible inner rotor speed is approximately:

$$\omega_{max,1} = V/R \tag{6.5}$$

where R is the distance between inner rotor center and lobe tip, as shown in Fig. 6.3.

Secondly, cavitation could also begin at onset of turbulent flow within the inlet gallery, which has the same plane area of the inlet port (the crescent shape in Fig. 6.3). To avoid turbulent conditions, the maximum Reynolds number allowed for in our design is set as:

$$Re = 2000 = U d_{port}/\nu \tag{6.6}$$

where U is fluid velocity, d_{port} is the gallery diameter, and ν is working fluid kinematic viscosity.

The volumetric flow rate into the inlet gallery is then:

$$Q = AU = \pi d_{port}^2 U/4 = D\omega_{max,2} \tag{6.7}$$

The maximum permissible speed is therefore:

$$\omega_{max} = min(\omega_{max,1}, \omega_{max,2}) \tag{6.8}$$

In this study, a mixture of purified water (density $998 kg/m^3$, kinematic viscosity $\sim 1 cst$) and propylene glycol (density $1040 kg/m^3$, kinematic viscosity $\sim 45 cst$) in a 9:1 volume ratio was used as the working fluid to increase the maximum permissible speed to avoid the onset of cavitation. This fluid also has the advantage of being less toxic and less caustic than either based hydraulic fluid.

6.3.3 Energy Efficiency Evaluation

The total energy efficiency of the mHPU is described and evaluate by the volumetric efficiency, the mechanical to hydraulic efficiency and the electric motor efficiency.

The volumetric efficiency of the pump head η_v is defined as the ratio of the measured pump flow rate Q_{exp} to the theoretical flow rate Q_{th}:

$$\eta_v = \frac{Q_{exp}}{Q_{th}} = \frac{Q_{exp}}{Dn} \tag{6.9}$$

The mechanical to hydraulic efficiency of the mHPU η_{mh} is defined similarly as:

$$\eta_{mh} = \frac{T_{th}}{T_{eff}} = \frac{D\Delta P}{2\pi T_e} \tag{6.10}$$

where T_{th} is the theoretical torque output, and T_{eff} is the effective torque required to rotate the motor shaft and pump head across the pressure difference ΔP. T_e, the torque provided by the electric motor, can be approximated by measuring the motor phase current i_{EM} and multiplying with torque constant k_T.

$$T_e = i_{EM} k_T \tag{6.11}$$

The overall pump efficiency (not including the motor) η_{pump} is then the ratio between delivered hydraulic power $\mathbb{P}_{hyd}$ and required mechanical power $\mathbb{P}_{mech}$:

$$\eta_{pump} = \frac{\mathbb{P}_{hyd}}{\mathbb{P}_{mech}} = \frac{Q_{exp}\Delta P}{2\pi n T_e} = \eta_v \eta_{mh} \tag{6.12}$$

The efficiency of the electric motor η_{em} converting electric power $\mathbb{P}_{ele}$ into mechanical power $\mathbb{P}_{mech}$ is:

$$\eta_{em} = \frac{\mathbb{P}_{mech}}{\mathbb{P}_{ele}} = \frac{2\pi n T_e}{V_s i_s} \tag{6.13}$$

where V_s is the voltage provided by the power supply and i_s is the drawn current.

Therefore, the total efficiency of the mHPU η_{tot} converting electric power $\mathbb{P}_{ele}$ into mechanical power $\mathbb{P}_{mech}$ and then into hydraulic power $\mathbb{P}_{hyd}$ can be obtained by multiplying η_v, η_{mh} and η_{em}:

$$\eta_{tot} = \frac{\mathbb{P}_{hyd}}{\mathbb{P}_{ele}} = \eta_v \eta_{mh} \eta_{em} \tag{6.14}$$

6.4 mHPU Prototype Design and Manufacture

An experimental prototype of the proposed mHPU was designed to be capable of delivering a flowrate of $0-3000mL/min$ at pressures ranging from $0-400kPa$. The pump head, with a displacement of $0.5mL/rev$, was customed designed and CNC manufactured (Proto Labs, MN) with PTFE material to reduce friction and maintain a low moment of inertia (due to its light weight). A specially-designed port part (part 2 in Fig. 6.4A) was 3D printed using a resin printer (Formlabs, MA). It has two grooves for o-ring placements to prevent leakage through possible gaps. It also has two built-in NPT threads, allowing easy and tight installation of two push-in NPT fittings (part 1 in Fig. 6.4A). Note that additional structures to integrate pressure sensors can be easily designed and incorporated into this part. A Maxon BLDC motor (EC-max 30, part number 272763) was selected to drive the pump head, and its shaft was filed to a flat surface to complete the mount. An o-ring and a dynamic seal were used to minimize leakages through the motor-pump case interface. Additional sealing using silicone sealant caulk (GE, MA) was applied externally to further seal the pump head.

The overall mHPU prototype results in a nice compact package with a total weight of 347 gram, a length of 120 mm, and a diameter of 30 mm. The detailed design is illustrated in Fig. 6.4, along with part descriptions listed in Tab. 6.1.

6.5 mHPU Prototype Experimental Test

Once the experimental prototype was manufactured and assembled, both dynamic and steady state performance were characterized and evaluated.

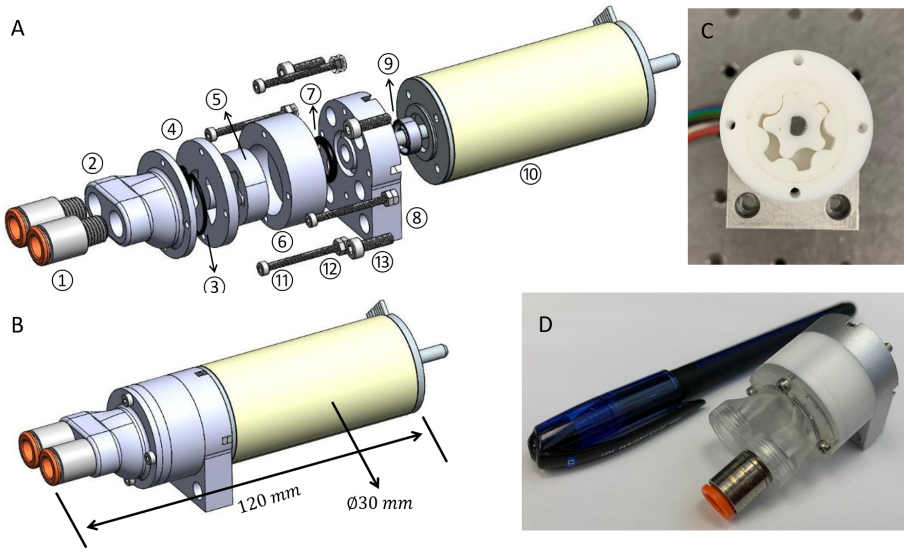

Figure 6.4: (A) Exploded view of CAD design. (B) Isometric view of CAD design. (C) Photo of the pump core. (D) Photo of the pump head with a pen.

Table 6.1: Prototype Part Descriptions

Part Number	Part Name	Part Specification
1	Push-in fitting	1/4in PI x 1/8in PI
2	Port	3D printed by Formlab printer
3	O-ring	I.D. 12mm, O.D. 14mm, width 1mm
4	Port plate	CNC with PTFE
5	Gerotor core	CNC with PTFE, diameter 22mm
6	Pump case	CNC with PTFE, depth 6.5mm
7	O-ring	I.D. 9mm, O.D. 13mm, width 2mm
8	Base	CNC with Aluminum
9	Rotary seal	I.D. 4mm
10	Motor	Maxon EC-max 30
11	Screw	M2, length 25mm
12	Nut	M2
13	Screw	M3, length 6mm

6.5.1 Experimental Setup

The schematic of the experimental setup is illustrated in Fig. 6.5A and the corresponding bench top setup is shown in Fig. 6.5B. The mHPU delivers flow to a variable orifice

valve which can by manually adjusted to set the load pressure. A magnetic-inductive flow meter (SM4000, IFM Efector, Germany) was placed in line to measure the flow rate out from mHPU. Two pressure sensors (SSCSANT100PGAB3, Honeywell, MN) were placed to measure the pressure levels at the inlet and outlet ports of the mHPU. An analog servo drive (AZBH12A8, A.M.C., CA) along with a compatible mounting shield (MC1XAZ01, A.M.C., CA) were selected to implement BLDC motor speed control. The servo drive also provided an analog voltage proportional to the motor phase current i_{EM}. A current probe (A1146, Agilent Technologies, CA) measured the drawn current i_s from the power supply unit ($24V$). Finally, the pressure levels, flow rate, motor speed, motor phase current and power supply drawn current were all read with a PCIe-6343 NI DAQ board (National Instruments, TX) on a xPC Target Machine (Mathworks, MA) with a sampling rate of $10kHz$.

6.5.2 Dynamic Characterization

A series of sinusoidal speed command signals with a variety of amplitudes (1500, 3000, 4500 and 6000rpm) and frequencies (0.5, 1, 2, 5, 10, 20, 30, 40Hz) were sent to the mHPU controller. Since the mHPU is bi-directional, these speed commands resulted in rapid pumping in and out of the mHPU as would be seen during feedback control of a soft actuator. The prototype's response was measured to assess the mHPU's closed-loop bandwidth for flow control. Bode plots in Fig. 6.6A depict the bandwidth test results. Fig. 6.6B shows the response of the most extreme test case (speed command signal: 6000rpm amplitude and 40Hz frequency) and corresponding motor winding current i_{EM}, respectively.

These results show that the mHPU's -3 dB bandwidth is nearly 35 Hz, well above the mechanical frequency of many soft robotic actuators such as fiber-reinforced bending actuators 1-2 Hz [21], and air-filled soft actuators 1-5 Hz [39].

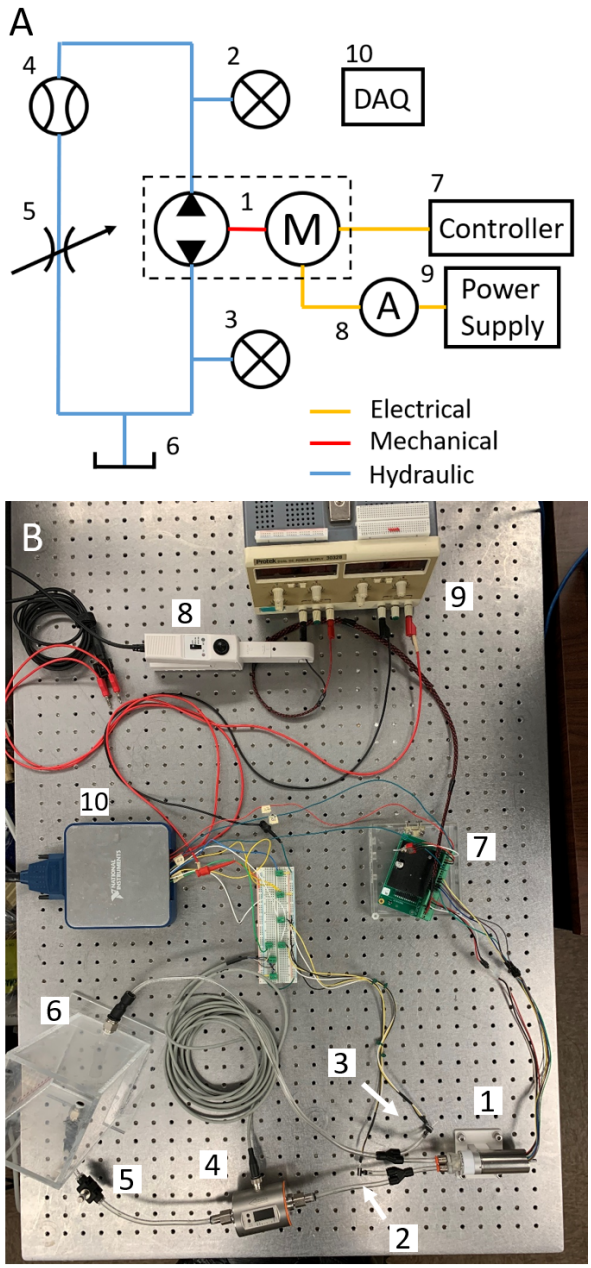

Figure 6.5: (A) Schematics of experimental setup. (B) Photo of experimental setup. (1) mHPU prototype, (2) outlet pressure sensor, (3) inlet pressure sensor, (4) flow meter, (5) variable orifice valve, (6) reservoir, (7) A.M.C. controller, (8) current probe, (9) power supply, (10) DAQ

6.5.3 Energy Efficiency Evaluation

The steady state performance of the proposed mHPU was measured (pump characterization curves) and energy efficiency was then evaluated. The mHPU was operated under

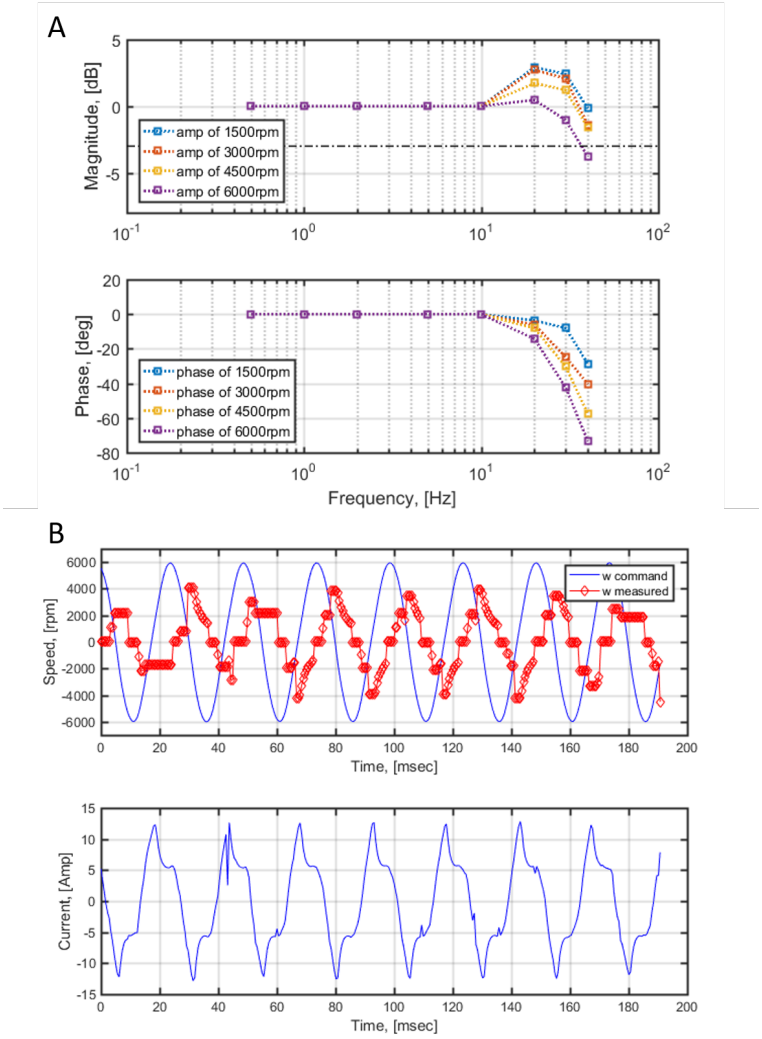

Figure 6.6: (A) Bode plot from bandwidth experiments of the mHPU prototype. (B) Upper: Measured and command mHPU speed at 6000rpm and 40Hz. Lower: Motor winding current at 6000rpm and 40Hz.

various motor speeds and against pressure differences. The pressure difference across the pump was established by setting the variable orifice valve shown in Fig. 6.5. Measured data points were recorded (red circles in Figs. 6.7-6.12) and interpolated with 3-order polynomial fitting functions to plot out the device energy efficiency topography surfaces. The boundary of all the topography surfaces are determined by achievable motor speed and pressure difference.

The output flow rate Q and volumetric efficiency η_v are plotted against various oper-

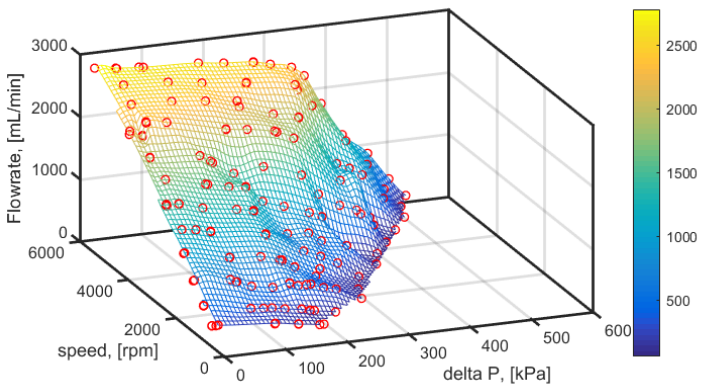

Figure 6.7: Flowrate v.s. speed v.s. pressure difference of mHPU prototype.

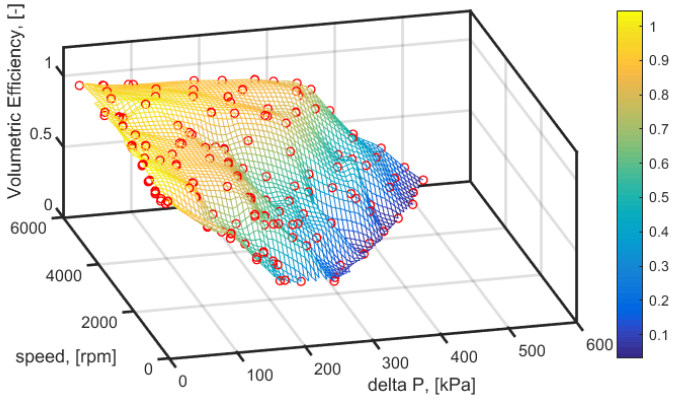

Figure 6.8: Volumetric efficiency of mHPU prototype vs. speed vs. pressure difference.

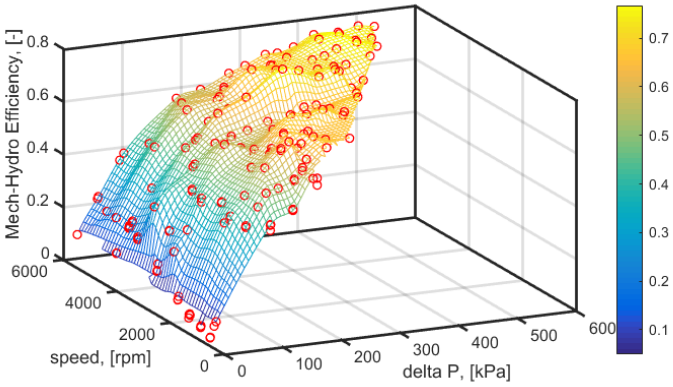

Figure 6.9: Mechanical-to-Hydraulic efficiency of mHPU prototype vs. speed vs. pressure difference.

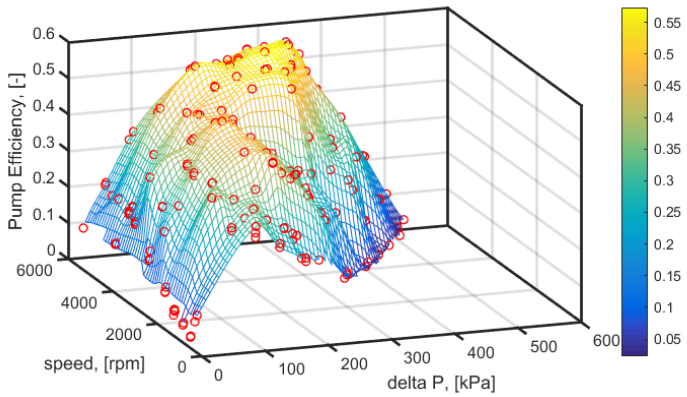

Figure 6.10: Pump efficiency of mHPU prototype vs. speed vs. pressure difference.

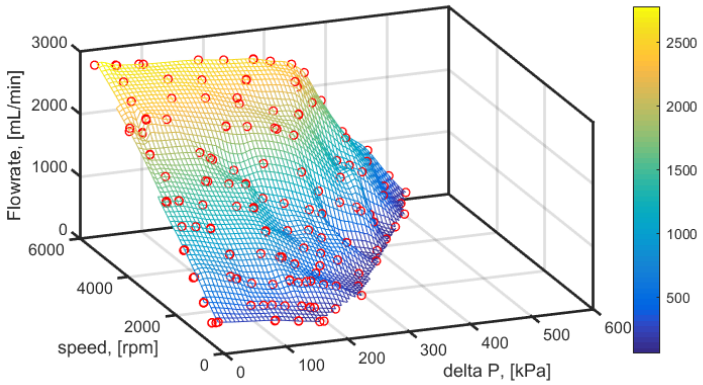

Figure 6.11: Electric motor efficiency of mHPU prototype vs. speed s. pressure difference.

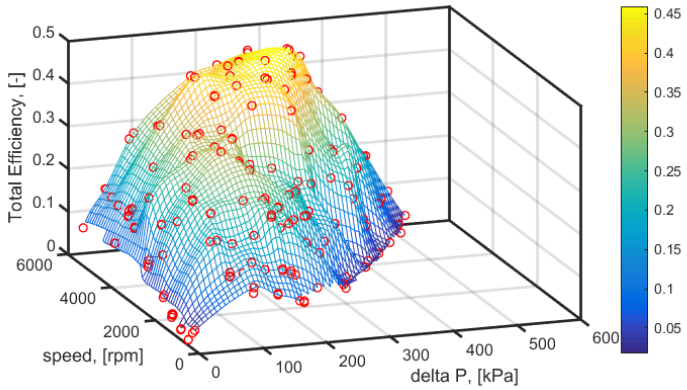

Figure 6.12: Total efficiency of mHPU prototype vs. speed vs. pressure difference.

ating speed and pressure difference in Fig. 6.7 and Fig. 6.8 respectively. As it can be seen that when operating at the same speed, as the pressure difference increases, the actual

delivered output flow rate drops due to the increased leakage. Note from Fig. 6.8 that the volumetric efficiency drops quicker at low operating speed than high operating speed. This phenomenon also coincides our previous suggestion that a mHPU should be designed to operating at medium to high speed range.

The mechanical to hydraulic efficiency η_{mh} is shown in Fig. 6.9. The topography indicates that more energy is used to overcome friction losses such as friction of the motor, dynamic seal friction, and sliding motion friction at low working pressure conditions. However, the relative sliding motion exists in all kinds of pumping mechanisms and necessary dynamic seals are critical to avoid leakage. Hence, targeting operations at medium/high speed during design is one way to improve the efficiency. Fortunately, this is normally the case because an unactuated fluidic elastomer soft actuator (e.g. [14, 21]) would not require power or flow from the mHPU.

The overall pump efficiency η_{pump} can be obtained by combining the two topographies ($\eta_{pump} = \eta_v \eta_{mh}$) and is plotted in Fig. 6.10. This curve plays an analogous role to an efficiency curve of a gearhead for a rigid robot servomotor, where pressure difference is replaced with load torque.

Figure 6.11 depicts the topography of the electric motor efficiency η_{em} versus various operating speed and pressure. The general trend, though not very smooth, indicates that energy losses associated with the motor itself, such as iron loss and winding loss, are more significant at low operating speeds and load pressures. Note that this curve would be the same (where pressure difference were replaced by load torque) if this motor were used as a servomotor for a rigid robot.

Finally, the total efficiency of the mHPU η_{tot} converting electric power $\mathbb{P}_{ele}$ into mechanical power $\mathbb{P}_{mech}$ and then into hydraulic power $\mathbb{P}_{hyd}$ is presented in Fig. 6.12. As expected, the mHPU prototype reaches its highest efficiency at medium/high speed and medium pressure since BLDC motors work most efficiently at medium/high speed under medium load torque and the pump's volumetric efficiency drops less at high speed and

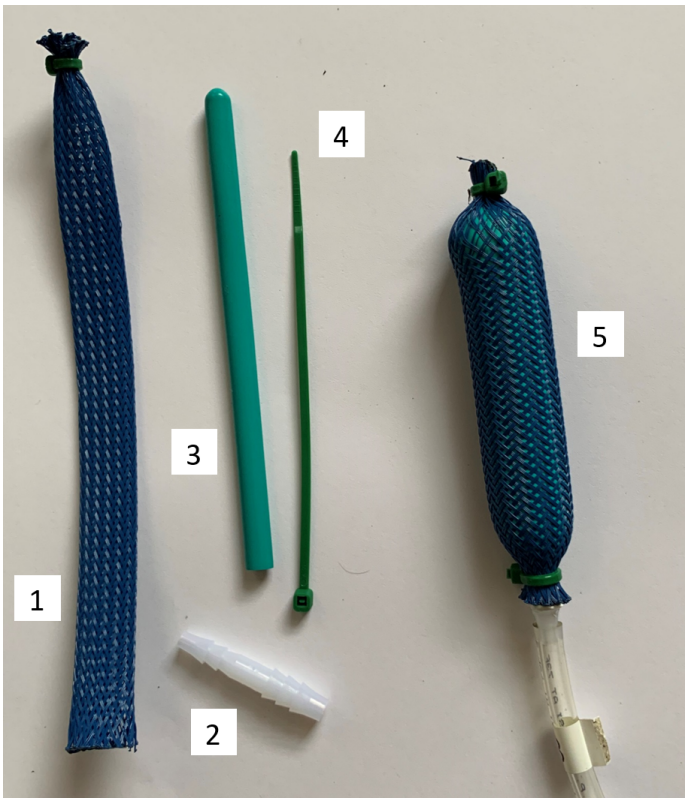

Figure 6.13: Fast-prototyped fluidic muscle: 1) expandable sleeving, 2) barbed tube fitting, 3) party balloon, 4) zip tie, 5) pressurized stage.

medium/high pressure. Therefore, correct sizing of pump head and selection of the motor according to the operation range of soft robot are the key to maintaining high efficiency and power density.

6.6 Position Control using mHPU

To demonstrate the suitability and feasibility of the proposed mHPU to rapidly and accurately control soft robotics, a common soft actuator, a fluidic muscle (Fig. 6.13), was fast prototyped and controlled to achieve desired position.

The experiment setup is shown in Fig. 6.14A. The fluidic muscle was connected to a 3D printed mass block, which sits on a linear slider (Igus, Germany). When the fluidic muscle is pressurized, it retracts; and vice versa. A sequence of stair waves of desired positions (magnitude 16 mm) was sent to be tracked by the fluidic muscle. Since the

control strategy study is not the main focus of this paper, simple PID control ($K_p = 2, K_i = 0.02, K_d = 0.045$) was utilized and the control diagram is shown in Fig. 6.14B. A command voltage is generated by the PID controller with the position error as the input. The motor servoamp proportionally outputs a current according to the controller's output voltage (4 volts to 6 output amps) and drives the mHPU's motor to run the integrated gerotor pump to pressurize/depressurize the fluidic muscle. The position of the mass block is measured by a linear encoder (US digital, WA).

Position tracking results are presented in Fig. 6.15A with a close-up of the steady-stae position in Fig. 6.15B. The corresponding mHPU motor speed is depicted in Fig. 6.15C. Firstly, note from Fig. 6.15C that the overall system has roughly a 0.2 sec rise time. Second, the system illustrates good system performance with around 0.2 mm position error. Note that when the fluidic muscle is pressurized and contracted to maintain at the desired position (Fig. 6.15B), the mHPU is still slightly rotating to compensate back flows and leakages through gerotor gear gaps under high pressure. While during the depressurization and expansion phase, the mHPU does not rotate as the back flow under low pressure is negligible.

6.7 Discussion

A compact, convenient, and high-bandwidth miniature hydraulic power unit is proposed to offer an alternative approach for the community to actuate soft robots for various applications with high power, speed and accuracy. A first-generation prototype with a brushless DC motor and an integrated gerotor bi-directional pump was designed and manufactured. Its basic specifications are listed in Tab. 6.2.

Compact. As can be seen from Tab. II and Fig. 6.4, the overall unit is a compact package with an integrated pumphead, similar to a motor and gearhead combination. In an analogous manner, the BLDC motor occupies most of the volume (axial length 60mm) and weight (305gram). This design is scalable to a large range of motor sizes and power

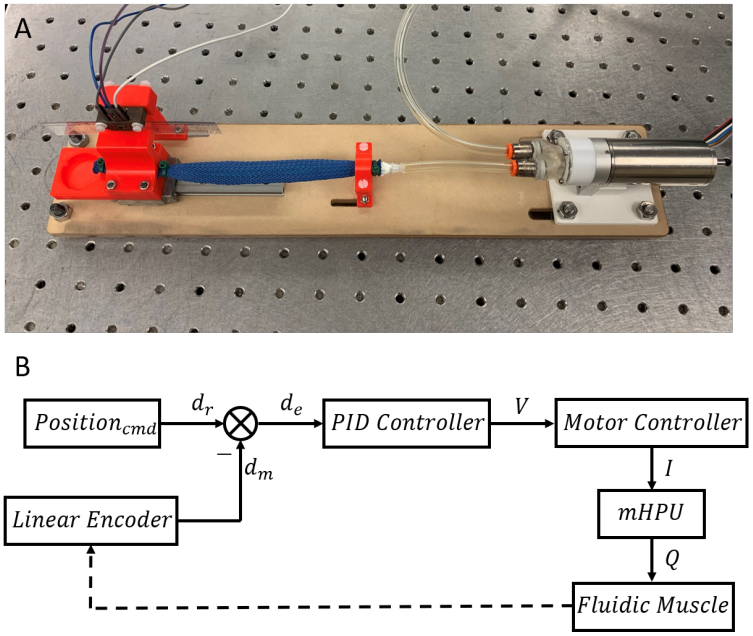

Figure 6.14: (A) photo of experiment setup, (B) control diagram.

Table 6.2: mHPU Prototype Spec

Property	Value
Length	$120mm$
Diameter	$30mm$
Weight	$347gram$
Displacement	$0.5mL/rev$
Speed Range	$0-6000rev/min$
Flow Range	$0-2950mL/min$
Pressure Range	$0-500kPa$
Bandwidth	$35Hz$
Power Density (peak)	$0.058W/g$

output capability (larger and smaller). This scalabilty is due to the high power density of hydraulic pump systems, including the gerotor pump architecture. Additonally, although this prototype was designed for similar working pressures as seen in current soft actuators, the ability of this miniature hydraulic system to be designed to achieve pressures higher than those seen in pneumatic systems affords the possibility of miniaturizing the inflatable

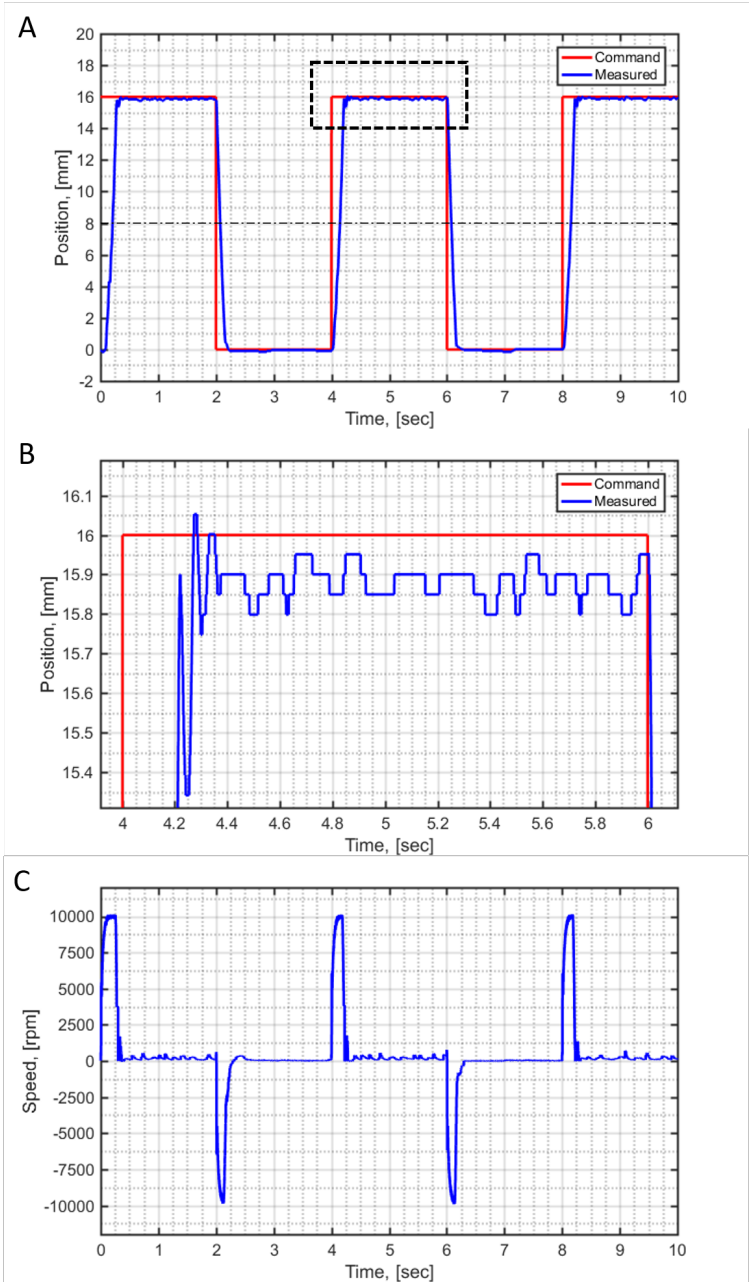

Figure 6.15: Position control results: (A) desired and measured positions, (B) zoom-in look, (C) measured mHPU motor speed.

space in the core of soft actuators. This could result in dramatically smaller and/or more capable soft actuators.

High Bandwidth. Compared to the relatively poor dynamic behavior from controlled pneumatic soft robots, the nearly incompressible property of the servopump's working fluid

allows energy to be delivered nearly instantaneously from the mHPU to the actuator [40], and enables fast dynamic response. The mHPU's speed is controlled to proportionally convert electric power into hydraulic power to actuate soft robots in a simpler manner and with fewer energy domain transitions than a pneumatic approach. This not only makes the the overall system more compact, but also improves the system energy efficiency [33]. The absence of valves (pneumatic) and mechanical transmission lines (cable-driven) also permits the back-drivability of the power unit, allowing fast and symmetric functionality in both directions with little hysteresis. The high bandwidth of approximately 35 Hz is well above the mechanical frequency of typical soft actuators, making the mHPU suitable for fast soft robot actuation.

High Power Density. Bear in mind that the BLDC motors are ideally suited for various applications due to their high power density and the one used for the mHPU prototype has a power density of 0.2 W/g (MAXON EC-max30: 60W, 305gram). Also note that the peak total efficiency is near 45%, illustrating high energy efficiency and high power density of the proposed mHPU prototype (similar to that seen with motor/gearhead combinations in rigid robotics). As previously mentioned, the ability of this servopump concept to achieve much higher pressures than current soft actuation systems allows the design space of soft actuators to expand to include very small inflation volumes that have the potential for even greater mechanical power delivery per unit size of the actuator than current technology.

6.8 Conclusion

This paper presents the basic working principles of a miniature hydraulic power unit (mHPU or servopump) for soft robot actuation, along with its design methods and optimization metrics. A detailed energy evaluation is presented and can serve as a guide for other designs. A first-generation prototype was designed and manufactured, and experiments were conducted. Bandwidth of the prototype was tested to illustrate its feasibility for powering typical soft actuators. Energy efficiency was evaluated to give insights and

suggestions for system-level optimization. Position control of a typical soft actuator utilizing the proposed mHPU was demonstrated to illustrate the feasibility and suitability of powering soft actuators. The mHPU servopump delivers high power that is rapidly controlled, in a compact convenient package, with high efficiency. It is our hope that this servopump will become the standard "servomotor" for the soft robotics community.

6.9 Acknowledgement

This work was supported by the National Science Foundation grant EFMA-1935278.

6.10 References

[1] Daniela Rus and Michael T Tolley. Design, fabrication and control of soft robots. Nature, 521(7553):467, 2015.

[2] Ian D Walker. Continuous backbone "continuum" robot manipulators. Isrn robotics, 2013, 2013.

[3] Radosław Cie´slak and Adam Morecki. Elephant trunk type elastic manipulator-a tool for bulk and liquid materials transportation. Robotica, 17(1):11–16, 1999.

[4] Ian A Gravagne and Ian D Walker. Uniform regulation of a multi-section continuum manipulator. In Proceedings 2002 IEEE International Conference on Robotics and Automation (Cat. No. 02CH37292), volume 2, pages 1519–1524. IEEE, 2002.

[5] Michael W Hannan and Ian D Walker. Kinematics and the implementation of an elephant's trunk manipulator and other continuum style robots. Journal of robotic systems, 20(2):45–63, 2003.

[6] William McMahan, Bryan A Jones, and Ian DWalker. Design and implementation of a multi-section continuum robot: Air-octor. In 2005 IEEE/RSJ International Conference on Intelligent Robots and Systems, pages 2578–2585. IEEE, 2005.

[7] David B Camarillo, Christopher R Carlson, and J Kenneth Salisbury. Configuration tracking for continuum manipulators with coupled tendon drive. IEEE Transactions on Robotics, 25(4):798–808, 2009.

[8] Marcello Calisti, Andrea Arienti, Maria Elena Giannaccini, Maurizio Follador, Michele Giorelli, Matteo Cianchetti, Barbara Mazzolai, Cecilia Laschi, and Paolo Dario. Study and fabrication of bioinspired octopus arm mockups tested on a multipurpose platform. In 2010 3rd IEEE RAS & EMBS International Conference on Biomedical Robotics and Biomechatronics, pages 461–466. IEEE, 2010.

[9] Hesheng Wang, Weidong Chen, Xiaojin Yu, Tao Deng, Xiaozhou Wang, and Rolf Pfeifer. Visual servo control of cable-driven soft robotic manipulator. In 2013 IEEE/RSJ International Conference on Intelligent Robots and Systems, pages 57–62.IEEE, 2013.

[10] Kamal Youcef-Toumi et al. Design of machines with compliant bodies for biomimetic locomotion in liquid environments. ASME J. Dyn. Syst., Meas., Control, 128(1):3–13, 2006.

[11] Andrew D Marchese and Daniela Rus. Design, kinematics, and control of a soft spatial fluidic elastomer manipulator. The International Journal of Robotics Research, 35(7):840–869, 2016.

[12] Panagiotis Polygerinos, Stacey Lyne, Zheng Wang, Luis Fernando Nicolini, Bobak Mosadegh, George M Whitesides, and Conor J Walsh. Towards a soft pneumatic glove for hand rehabilitation. In 2013 IEEE/RSJ International Conference on Intelligent Robots and Systems, pages 1512–1517. IEEE, 2013.

[13] Raphael Deimel and Oliver Brock. A novel type of compliant and underactuated robotic hand for dexterous grasping. The International Journal of Robotics Research, 35(1-3):161–185, 2016.

[14] Michael T Tolley, Robert F Shepherd, Bobak Mosadegh, Kevin C Galloway, Michael Wehner, Michael Karpelson, Robert J Wood, and George M Whitesides. A resilient, untethered soft robot. Soft robotics, 1(3):213–223, 2014.

[15] Andrew D Marchese, Cagdas D Onal, and Daniela Rus. Autonomous soft robotic fish capable of escape maneuvers using fluidic elastomer actuators. Soft Robotics, 1(1):75–87, 2014.

[16] Cagdas D Onal and Daniela Rus. Autonomous undulatory serpentine locomotion utilizing body dynamics of a fluidic soft robot. Bioinspiration & biomimetics, 8(2):026003, 2013.

[17] Koichi Suzumori, Satoshi Endo, Takefumi Kanda, Naomi Kato, and Hiroyoshi Suzuki. A bending pneumatic rubber actuator realizing soft-bodied manta swimming robot. In Proceedings 2007 IEEE International Conference on Robotics and Automation, pages 4975–4980. IEEE, 2007.

[18] Cagdas D Onal, Xin Chen, George M Whitesides, and Daniela Rus. Soft mobile robots with on-board chemical pressure generation. In Robotics Research, pages 525–540. Springer, 2017.

[19] Gregory McCarthy, Daniil Effraimidis, Brian Jennings, Nicholas Corso, Cagdas D Onal, and MB Popovic. Hydraulically actuated muscle (ham) exo-musculature. In Robot Makers: The Future of Digital Rapid Design and Fabrication of Robots (RoMa) Workshop, 2014.

[20] Robert K Katzschmann, Andrew D Marchese, and Daniela Rus. Hydraulic autonomous soft robotic fish for 3d swimming. In Experimental Robotics, pages 405–420. Springer, 2016.

[21] Panagiotis Polygerinos, Zheng Wang, Kevin C Galloway, Robert J Wood, and Conor J Walsh. Soft robotic glove for combined assistance and at-home rehabilitation. Robotics and Autonomous Systems, 73:135–143, 2015.

[22] Justin W Raade, Kurt R Amundson, and H Kazerooni. Development of hydraulic-electric power unit for mobile robots. In ASME 2005 International Mechanical Engineering Congress and Exposition, pages 27–34. American Society of Mechanical Engineers Digital Collection, 2005.

[23] Kurt Amundson, Justin Raade, Nathan Harding, and Hami Kazerooni. Hybrid hydraulic-electric power unit for field and service robots. In 2005 IEEE/RSJ International Conference on Intelligent Robots and Systems, pages 3453–3458. IEEE, 2005.

[24] Adam Zoss and H Kazerooni. Architecture and hydraulics of a lower extremity exoskeleton. In ASME 2005 International Mechanical Engineering Congress and Exposition, pages 1447–1455. American Society of Mechanical Engineers Digital Collection, 2005.

[25] Saeid Habibi and Andrew Goldenberg. Design of a new high performance electrohydraulic actuator. In 1999 IEEE/ASME International Conference on Advanced Intelligent Mechatronics (Cat. No. 99TH8399), pages 227–232. IEEE, 1999.

[26] Kyoung Kwan Ahn, Doan Ngoc Chi Nam, and Maolin Jin. Adaptive backstepping control of an electrohydraulic actuator. IEEE/ASME transactions on mechatronics, 19(3):987–995, 2013.

[27] Joerg Grabbel and Monika Ivantysynova. An investigation of swash plate control concepts for displacement controlled actuators. International journal of fluid power, 6(2):19–36, 2005.

[28] Sangok Seok, Cagdas Denizel Onal, Kyu-Jin Cho, Robert J Wood, Daniela Rus, and Sangbae Kim. Meshworm: a peristaltic soft robot with antagonistic nickel titanium coil actuators. IEEE/ASME Transactions on mechatronics, 18(5):1485–1497, 2012.

[29] Huai-Ti Lin, Gary G Leisk, and Barry Trimmer. Goqbot: a caterpillar-inspired soft-bodied rolling robot. Bioinspiration & biomimetics, 6(2):026007, 2011.

[30] Cecilia Laschi, Matteo Cianchetti, Barbara Mazzolai, Laura Margheri, Maurizio Follador, and Paolo Dario. Soft robot arm inspired by the octopus. Advanced Robotics, 26(7):709–727, 2012.

[31] Matteo Cianchetti, Tommaso Ranzani, Giada Gerboni, Thrishantha Nanayakkara, Kaspar Althoefer, Prokar Dasgupta, and Arianna Menciassi. Soft robotics technologies to address shortcomings in today's minimally invasive surgery: the stiff-flop approach. Soft robotics, 1(2):122–131, 2014.

[32] Marko B Popovic. Biomechatronics. Academic Press, 2019.

[33] Mengtang Li, Ryan Foss, Kim Stelson, James Van de Ven, and Eric John Barth. Design, dynamic modelling and experiment validation of a novel alternating flow variable displacement hydraulic pump. IEEE/ASME Transactions on Mechatronics, 2019.

[34] Michael Wehner, Michael T Tolley, Yi˘git Meng¨uc¸, Yong-Lae Park, Annan Mozeika, Ye Ding, Cagdas Onal, Robert F Shepherd, George M Whitesides, and Robert JWood. Pneumatic energy sources for autonomous and wearable soft robotics. Soft robotics, 1(4):263–274, 2014.

[35] Raymond P Lambeck. Hydraulic pumps and motors: selection and application for hydraulic power control systems. Technical report, 1983.

[36] JR Colbourne. Gear shape and theoretical flow rate in internal gear pumps. Transactions of the Canadian Society for Mechanical Engineering, 3(4):215–223, 1975.

[37] Andrew J Robison and Andrea Vacca. Kinematic multi-objective optimization of circular-toothed gerotor pumps by genetic algorithm. In ASME/BATH 2017 Symposium on Fluid Power and Motion Control. American Society of Mechanical Engineers Digital Collection, 2017.

[38] Jasper De Viaene, Florian Verbelen, Stijn Derammelaere, and Kurt Stockman. Energyefficient sensorless load angle control of a bldc motor using sinusoidal currents. IET Electric Power Applications, 12(9):1378–1389, 2018.

[39] Steven I Rich, Robert J Wood, and Carmel Majidi. Untethered soft robotics. Nature Electronics, 1(2):102–112, 2018.

[40] Andrew D Marchese, Robert K Katzschmann, and Daniela Rus. A recipe for soft fluidic elastomer robots. Soft robotics, 2(1):7–25, 2015.

Chapter 7

Conclusion

7.1 Summary

This dissertation has presented a model informed design methodology to evaluate and refine innovative hydraulic pump concepts. This methodology is demonstrated on three distinctly different applications, namely 1) industrial and mobile hydraulics, 2) mechanical circulatory support device, and 3) soft robot actuation method.

For the industrial and mobile hydraulic application, a novel rotary variable displacement pump inspired by alternating flow concept was modeled, designed, fabricated and evaluated. This AF pump 1) offers a more energy efficient way to directly power every actuator, eliminating metering losses; 2) achieves high efficiency across a wide range of operating conditions and displacements; and 3) allows multiple units to be easily common-shaft mounted for a compact multi-actuator displacement control system from a single prime mover.

For mechanical circulatory support application, two novel pumping architectures were proposed. The spherical gerotor MCS pump 1) presents a novel rotary positive displacement pumping fashion; 2) is capable for both circulation sides (systemic and pulmonary) with only 1 DoF; and 3) theoretically reduces shear stress mediated blood damage by its low operating speed. The vane MCS pump 1) shows itself as a novel alternative architecture capable of generating blood flow within clinic range; 2) reduces shear stresses imparted to blood by dramatic reduced rotary speed, particularly in comparison to present VADs (5000 rpm+); and 3) demonstrates the ability of generating pulsatile flow to address related issue of current MCS devices.

For soft robot actuation, a miniature hydraulic power unit came as a fruition from the methodology. This hydraulic ”servo” motor for soft robotics features 1) extremely high

bandwidht ($\sim 35Hz$), well above the mechanical frequency of typical soft robots; 2) high energy efficiency (with peak efficiency near 45%); 3) nice compact size to be integrated into many soft robot structure within a closed loop; and 4) suitability and feasibility for soft robotic actuation.

7.2 Contribution

Key contributions for the five manuscripts resulting directly from this work are:

1. A novel alternating flow variable displacement hydraulic pump to improve efficiency of industrial actuators across various operating conditions and displacements
2. A dynamic model capturing interactions between cardiovascular systems and MCS devices based on bond graph technology
3. A novel spherical gerotor pump as a compact, valveless, pulsatile flow MCS device
4. A novel sliding vane pump as a compact, valveless, pulsatile flow MCS device
5. A novel miniature hydraulic pump unit as a compact, energy dense, high efficient, and high bandwidth power source for soft robotics

These contributions represents a model informed design methodology to design, evaluate, and refine innovative hydraulic rotary pump concepts, and collectively help to shed lights on the usage of fluid power with novel hydraulic rotary pumps.